Search for Electroweakinos Using Two Soft Opposite-Sign Displaced Muons at the CMS Experiment

Dissertation
zur Erlangung des Doktorgrades
an der Fakultät für Mathematik, Informatik und
Naturwissenschaften
Fachbereich Physik der Universität Hamburg

vorgelegt von

Alexandra Tews

Hamburg

2024

Abstract

A search for the decay of heavy neutral particles into a dark matter candidate and a pair of displaced, low-energy muons is presented. The search targets supersymmetric extensions of the Standard Model of particle physics predicting light electroweakinos with compressed mass spectra with electroweakino mass differences ranging from 0.3 to 3.0 GeV. A bino or higgsino-like lightest supersymmetric particle (LSP) is considered, both of which as possible dark matter candidates. The heavier neutralino ($\tilde{\chi}_2^0$) has a decay length of up to a few centimeters and the decay can lead to a pair of opposite-charge muons. The analysis concentrates on identifying displaced tracks of muon pairs, employing a specialized reconstruction and identification method for the displaced secondary decay vertex of the $\tilde{\chi}_2^0$. The background is estimated from a control region in the data.

Data corresponding to an integrated luminosity of 36.4 fb^{-1} collected by the CMS experiment in proton-proton collisions at $\sqrt{s} = 13$ TeV are analyzed. The observed event yields are consistent with the Standard Model and exclusion limits are set in the plane of the $\tilde{\chi}_2^0$ mass and its mass difference to the LSP. For models with a mass difference of greater or equal to 1.25 GeV, $\tilde{\chi}_2^0$ with a mass of 115 GeV are excluded.

Zusammenfassung

Eine Suche nach dem Zerfall neutraler schwerer Teilchen in einen Dunkle Materie Kandidaten und ein verschobenes niederenergetisches Myonspurpaar. Die Suche zielt auf supersymmetrische Erweiterungen des Standardmodells ab, die leichte Elektroweakinos mit komprimierten Massenspektren vorhersagen. Die Massendifferenzen der Elektroweakinos reichen von 0,3 bis 3,0 GeV. Bino- oder Higgsino-artige leichteste supersymmetrisches Teilchen (LSP) werden angenommen, die jeweils Kandidaten für Dunkle Materie darstellen. Das schwerere Neutralino ($\tilde{\chi}_2^0$) hat eine Zerfallslänge von bis zu einigen Zentimetern und der Zerfall kann zu einem Myonenpaar mit entgegengesetzter elektrischer Ladung führen. Die Analyse konzentriert sich darauf, verschobene Spuren von Myonpaaren zu identifizieren, und verwendet eine spezielle Methode zur Rekonstruktion und Identifikation des verschobenen sekundären Zerfallspunktes des $\tilde{\chi}_2^0$. Die Untergründe werden aus einer Kontrollregion in den Daten bestimmt.

Daten, die einer integrierten Luminosität von 36,4 fb^{-1} entsprechen, und vom CMS-Experiment in Proton-Proton Kollisionen bei $\sqrt{s} = 13$ TeV gesammelt wurden, werden analysiert. Die Anzahl beobachteter Ereignisse stimmt mit dem Standardmodell überein und Ausschlussgrenzen werden in der Ebene der Masse des $\tilde{\chi}_2^0$ und des Massenunterschiedes zum LSP festgelegt. Für Modelle mit einer Massendifferenz größer oder gleich 1,25 GeV werden $\tilde{\chi}_2^0$ mit einer Masse von 115 GeV ausgeschlossen.

Contents

Preface

It is a special *privilege* to work in the field of natural sciences and in particular in experimental particle physics. To explain this rather personal statement, I will connect two distinct areas, which are also the two topics I am most passionate about. One is the way all the constituents of Nature are assembled to fit together from quarks to protons, molecules and, ultimately, our entire universe. As a mother of two wonderful daughters, the other is the way children develop according to a level of refinement reached after years of Darwinian evolution, a repeating pattern which is highly adaptable to the experiences accumulated by humans over the past 100,000 years [1]. In a way, in both cases, my admiration is for the evolution of the universe, just at very different domains and times of its history. The building blocks of matter we know today were probably produced around 13.7 billion years ago after a particularly fast expansion [2, 3]. The Earth is about 4.54 billion years old [4, 5]. The evolution of the human species that shapes the behavior of humans until today dates back around 7 million years [6, 7].

I can establish parallel between the two subjects. The development of young children progresses in steps. The achievement of a next developmental step comes mainly from within the children themselves. For instance, no adult needs to teach a child how to stand up. The child will try to do it all by itself. Developmental researchers have observed that the children's motivation is to transport toys, which is not possible when crawling on all fours [8]. Some children become very creative and briefly put the toy in their mouth, like a dog with a ball, or push it in front of them. But eventually, all children try to stand upright to have their hands free. Their motivation is a limitation, an apparent boundary that motivates them to overcome it. Here, I see the first parallel to fundamental research in particle physics. Let me take the example of the Standard Model (SM) of particle physics. It is consistent with most observable phenomena, from the reactions that fuel the Sun to the forces that hold a snowflake together. Over the past decades, its predictions have demonstrated remarkable precision, aligning closely with experimental data. Physicists regard the SM with a blend of admiration and frustration, acknowledging its successes while recognizing its inherent incompleteness. From its inception, it has been clear that the model has significant limitations [9]. It lacks for example the incorporation of gravity, a fundamental force in the universe [10]. Moreover, the SM incorporates particles that account for visible matter (or more precisely baryonic matter, as will be explained further along this thesis), overlooking the fact that

the majority of the universe is composed of dark matter and dark energy [2, 11, 12]. Limitations like these motivate particle physicists to push boundaries and to build experiments that surpass existing ones. Such as the world's largest particle accelerator, the Large Hadron Collider (LHC) at the European Organisation for Nuclear Research (CERN), whose data were used for the analysis in this doctoral thesis. Thus, the first parallel here is the drive that motivates physicists just like children to overcome given limitations.

Experiments like those at the LHC lead us to the second parallel. Scientists use experiments to test their assumptions and theories about Nature. The Compact Muon Solenoid Experiment (CMS) at the LHC, for example, is a large detector used, among other things, for the search for the components of dark matter. Evolution has taught children the same approach. Their exploratory learning is nothing more than experimental testing of assumptions about the world. For example, the slightly annoying phase in which children at a certain young age enjoy throwing objects to the ground, as long as there is an adult who picks them up again. The child is testing its assumption that everything falls to the ground. It has just discovered gravity. Like any good physicist, it would never believe in its discovery based on a single event. Thus, with this somewhat annoying behavior, it is collecting statistically significant event yields that support its theory of gravity [8].

At this point, I can get to the privilege mentioned above. In most cases, children's intrinsic motivation and evolutionary shaped development program are at least strongly hindered if not stopped completely. This happens quasi during the coming of age, and the cause for it lies in the overlay of intrinsic motivation (acting out of pure joy) by extrinsic motivation (doing something for a purpose). Children are often confronted with such extrinsic motivations from various sides while growing up, for example, in the form of praise and punishment from parents, grading or pressure for success in school, or societal obedience [13]. Keeping in mind that as adults, we are primarily conditioned to achieve a predefined result, to work purposefully and purpose-bound, one can come to understand what I consider a privilege in basic research.

When I explain my research on a search for dark matter and a plausible extension of the SM to people beyond physics, I am almost always asked, "And can it be used for something practical?" and I always answer with satisfaction, "No!" Of course, basic research has also produced many useful by-products in history, such as the World Wide Web, which can be traced back to an invention by physicist Tim Berners-Lee at CERN in 1989 [14]. But what is special about fundamental research is that the original motivation is not purpose-bound. Neither economic interests nor any other external motives drive it. It is solely about intrinsic motivations of the researchers, such as curiosity and the wish to increase humanity's collective knowledge, leading to a better understanding of the universe around us [15]. Being allowed to pursue my work in this way is what I have considered a great privilege. No less than Albert Einstein expressed this somewhat more poetically when he said: "The pursuit of truth and beauty is a sphere of activity in which we are permitted to remain children all our lives." [16]

Against this background, I present the results of my research work with great gratitude in this thesis, in which I had the opportunity to test the limits of our knowledge using a variety of experimental methods. The search for electroweakinos using data from the LHC accelerator collected by the CMS experiment, is a search for the potential components of dark matter, which is one of the greatest unresolved phenomena in modern natural sciences.

Introduction

Supersymmetric (SUSY) models attempt to extend the SM while maintaining consistency with existing observations and physical laws. SUSY models can introduce novel phenomena, such as dark matter, into the theoretical framework by predicting the existence of new elementary particles that are linked to the already known particles. A particularly interesting class of postulated particles are electroweakinos, particles whose mass eigenstates result from the mixing of the partner particles of the Higgs bosons, (higgsinos), and partners of the gauge bosons, (gauginos). The neutral mass eigenstates are called neutralinos, while the charged mass eigenstates are called charginos. Weakly Interacting Massive Particles (WIMPs) [17] are a prime candidate for dark matter, a concept supported by astrophysical evidence. In the so-called minimal supersymmetric model (MSSM) [18], a neutralino ($\tilde{\chi}^0$) serves as the lightest supersymmetric particle (LSP), presenting a viable WIMP candidate.

Scenarios where the mass difference between a bino or higgsino-like LSP and a heavier chargino or neutralino is minimal, so-called compressed SUSY models, provide a natural realization of SUSY. These final states are of particular relevance to searches for new physics at the LHC through relatively high production cross section on the order of 10^4 fb. Moreover, the predicted lightest electroweaknios are relatively light, i.e., on the order of $O(100)$ GeV and thus also kinematically accessible to experiments at the LHC.

The goal of the LHC is among others to test the predictions of different theories of particle physics, including measuring the properties of the SM particles, and searching for new particles predicted by supersymmetric theories. Numerous LHC searches have investigated charged or neutral electroweakino decays, establishing exclusion limits on SUSY model parameters. However, a region within the parameter space with electroweakino mass differences ranging from 0.3 to 3.0 GeV remains only mildly constrained by results from the LHC or the Large Electron-Positron Collider (LEP). The sensitivity of previous searches in that regime is limited by the low momentum of visible decay products. This thesis presents an analysis that is sensitive in this specific region.

In the examined signal models, the LSP and next-to-LSP are neutralinos. The heavier neutralino ($\tilde{\chi}^0_2$) has a decay length in the detector of up to a few centimeters. Its decay into the lighter neutralino ($\tilde{\chi}^0_1$) through an off-shell Z^*/γ^* boson can result in a pair of opposite-sign electrons or muons. This analysis concentrates on muonic decays,

given the advantageous experimental reconstruction efficiency for low-momentum muons. Due to the highly compressed mass spectra, these muons can have momenta below 5 GeV and thus often escape conventional reconstruction methods. The unique aspect of this analysis is a specialized reconstruction and identification method for the displaced secondary decay vertex of the $\tilde{\chi}_2^0$ supplemented by the application of machine learning techniques. Events are selected with one secondary vertex in final states featuring at least one high-momentum jet opposing a large missing transverse momentum. The SM background arises mostly from processes with neutrinos accompanied by inaccurately reconstructed leptons, spurious, or fake tracks. The backgrounds are estimated from the data in a control region. Thereby, the analysis presented in this thesis is able to probe the unexplored regime of compressed scenarios, which was not covered by previous analyses.

In Chapter 1 of the thesis, the theoretical motivation is introduced, including key elements such as the SM, evidence for dark matter, and identified limitations of the SM. Additionally, relevant supersymmetric models are discussed. In Chapter 2, the experimental setup is laid out giving a brief description of the relevant parts of the CMS detector along with the techniques employed for particle reconstruction and identification. Chapter 3 provides detailed information on the search itself, e.g., on signal characteristics, criteria for object and event selection, and methodologies for background estimation. In Chapter 4, the results for the analyzed data from 2016 and the expected limits derived with the luminosity from all data taken in the years 2016 to 2018 at the CMS experiment are given. The thesis concludes in the summary and outlook in Chapter 5.

1 Theory

The motivation for this thesis is driven by the need to explain experimental phenomena which the current best model of particle physics, the Standard Model, cannot explain, in particular the observed abundance of dark matter (DM) in the universe. To explain these phenomena an extension to the SM is required, in terms of particle content or interactions. Several such beyond-the-SM (BSM) theories would manifest through the existence of new particle classes, such as long-lived particles (LLPs), that may be detected at particle colliders such as the CERN LHC.

In the first section of this chapter, an overview on the SM of particle physics is given, followed by theoretical and experimental hints for physics beyond the SM. In the second section, off all those hints for new physics, DM is in the focus. The section starts with the motivation for DM from cosmological observations and arguments, followed by a discussion of the properties potential yet-undiscovered DM particles would have to possess to explain the observed abundance of DM. Possible BSM theories are then discussed, which predict the existence of new long-lived particles, including a valid DM candidate, in particular SUSY.

1.1 Standard Model of Particle Physics

This section introduces the Standard Model of particle physics. For a more comprehensive description of the SM and its theoretical derivation references [19, 20, 21] can be considered.

The SM stands as the most successful theory to date in explaining the phenomena observed in particle physics experiments and astronomical observations. The most significant recent validation of the theory is related to the concept of spontaneous symmetry breaking (SSB) namely the discovery of a Higgs boson by the ATLAS (A Toroidal LHC ApparatuS) and CMS collaborations at the LHC in 2012 [22, 23], and the subsequent measurement of the properties of the Higgs boson.

The SM provides a comprehensive framework for the understanding of the fundamental building blocks of matter and their interactions. It describes the elementary particles, distinguishing them by their respective charge, spin, and mass and explains their interaction mediated by fundamental forces. The SM encompasses three of the four fundamental

forces: electromagnetic, weak, and strong nuclear interactions. The fourth fundamental force, gravity, is not included in the SM at its given stage and does not seem to be compatible with fundamental quantum field theories (cf. Section 1.1.5).

In its mathematical formulation, the SM is a non-abelian gauge quantum field theory, with the underlying local gauge symmetries $SU(3)_C$ for quantum chromodynamics (QCD) and $SU(2)_L \times U(1)_Y$ for the unified electroweak theory. A unique charge is associated with each gauge symmetry denoted by the subscripts C, L and Y which will be explained in more detail below. A particle corresponds to an excitation of quantum fields.

1.1.1 Standard Model Particles

All elementary particles discovered so far can be classified into two categories: fermions with half-integer spin and boson with integer spin. Each charged particle has an associated antiparticle with the same mass but opposite charges, for example the electron e^- and the positron e^+.

The three fundamental interactions in the SM can be represented by the symmetry tensor product $SU(3)_C \times SU(2)_L \times U(1)_Y$, where subscripts indicate which types of SM particles participate in the respective interaction. Each fundamental interaction has an associated charge, and only fermions carrying that particular charge participate in the interaction. The subscript C refers to color-charged particles (related to the strong force), L refers to left-handed particles (related to the weak force), and Y refers to hypercharge particles (related to the electroweak force).

SM fermions are mathematically represented by Dirac spinors ψ. Dirac spinors in quantum field theory are four-component mathematical objects that encode the quantum states and dynamics of fermionic particles, describing their spin and determining their behavior under Lorentz transformations. Ferminons can be further categorized into leptons and quarks based on the charge they carry. Quarks carry electric, weak, and color charge and thus participate in all three fundamental forces of the SM, whereas leptons do not interact strongly but only participate in the electroweak interactions. Both leptons and quarks exist in three generations that differ in mass but have the same quantum numbers across the generations.

The spin of a particle determines its handedness or chirality, which, for massless particles, is equivalent to helicity. The helicity is defined by the sign of the spin vector's projection onto the momentum vector, where negative is left-handed and positive is right-handed. The chirality for a Dirac fermion ψ is defined using the operators

$$P_L = \frac{1}{2}(1 - \gamma^5), \quad P_R = \frac{1}{2}(1 + \gamma^5),$$

where $\gamma^5 = i \, \gamma^0 \, \gamma^1 \, \gamma^2 \, \gamma^3$ represent the Dirac matrices. The Dirac matrices include the identity matrix and the gamma matrices with the Pauli matrices σ_i as coefficients. The gamma matrices γ_μ incorporate spin and space-time properties of fermions. By

7

applying these projection operators to ψ, a Dirac field, which are the QFT representation of fermions, can be separated into its left- and right-handed components. Chirality is important because the fundamental interactions (gauge interactions) treat the left and right-chirality components of Dirac spinors differently. Left-handed fermions of one generation form an $SU(2)_L$ doublet that couples to the weak force. Right-handed fermions build an $SU(2)_R$ singlet that does not couple via the weak force. Unlike leptons, quarks are additionally grouped into $SU(3)_C$ triplets due to their color.

1.1.2 Fundamental Forces

In the $SU(3)_C \times SU(2)_L \times U(1)_Y$ symmetry, each subgroup requires the existence of corresponding gauge fields that act as the generators of the gauge group. These gauge fields are associated with vector bosons have spin 1 and are known as gauge bosons. They are force mediating particles in the SM. The Higgs boson has spin 0 and is responsible for providing all particle masses in the SM (cf. Section 1.1.3).

Any particle can be described in terms of its mass eigenstate, the state propagating in free space, or the gauge eigenstate (also: flavor), which denotes its participation in interactions. The eigenstates of the gauge bosons are: the B boson for $U(1)_Y$, the three W bosons $W_{1,2,3}$ for $SU(2)_L$, and the eight gluons $G_{1\ldots8}$ for $SU(3)_C$. Due to electroweak symmetry breaking (cf. Section 1.1.3), the B field and the neutral W_3 mix, forming new mass eigenstates that are physically observable as the A^0 field or γ (photon), and the Z field (Z boson). Additionally, the mixture of W_1 and W_2 gives rise to the $W^\pm$ fields. An overview of all fundamental SM particles and their main properties is given in Table 1.1.

	Names		Spin	Charge [e]	Mass [MeV]	Gauge Eigenstates	Mass Eigenstates
Fermions	Leptons	I	1/2	-1	0.511	e	$e, \mu, \tau,$ $\nu_{1,2,3}$
				0	$< 0.8 \times 10^6$	ν_e	
		II		-1	105.66	μ	
				0	$< 0.8 \times 10^6$	ν_μ	
		III		-1	1.78×10^3	τ	
				0	$< 0.8 \times 10^6$	ν_τ	
	Quarks	I		$+2/3$	2.2	u	$u, c, t,$ d, s, b
				$-1/3$	4.7	d'	
		II		$+2/3$	1.3×10^3	c	
				$-1/3$	93.0	s'	
		III		$+2/3$	172.7×10^3	t	
				$-1/3$	4.2×10^3	b'	
Bosons	Higgs Boson	Scalar	0	0	125.3×10^3	H	H
	W Bosons	Vector	1	± 1	80.38×10^3	$W_{1,2,3}$ B^0	$W^\pm$
	Photon			0	0		γ
	Z Boson			0	91.188×10^3		Z^0
	Gluons			0	0	$G_{1\dots8}$	$G_{1\dots8}$

Table 1.1: Particle content of the SM. The names of all SM particles are given along with the generation for fermions and the spin-type for bosons in the third column, as well as the electric charges, masses and eigenstates [24]. Each SM fermion has a respective anti-particle, which is not contained in this table.

As formula in special relativity and quantummechanics are littered with the speed of light in vacuum $c = 299792 \times 10^3$ m/s and the Planck's Constant h, $\hbar = \frac{h}{2\pi} = 1.055 \times 10^{-34}$ Js, it is convenient to set:

$$\hbar = c = 1 \tag{1.1}$$

in natural units. With this convention, the unit of mass, momentum and energy is GeV, as the energy–momentum relation, or relativistic dispersion relation

$$E^2 = (pc)^2 + (m_o c^2)^2 \tag{1.2}$$

becomes

$$E^2 = p^2 + m_o^2. \tag{1.3}$$

Moreover, a particle's charge is typically given in units of e, which represents the elementary charge, i.e., the magnitude of the electric charge carried by a single proton or a single electron: $1e = 1.602 \times 10^{-19}$C. In Table 1.1, as well as throughout this thesis, **natural units** are used for particles energies, momenta and masses.

1.1.3 Higgs Mechanism

In the early universe, shortly after the big bang, all particles and forces are believed to have been unified in a single force. As the universe cooled down and underwent a phase transition, the electroweak symmetry was spontaneously broken. After that, this symmetry was no longer apparent in the low-energy state of the universe but the distinct electromagnetic and weak nuclear forces we observe today. This process is described by the electroweak symmetry breaking, represented by the electroweak symmetry group $SU(3)_C \times SU(2)_L \times U(1)_Y$. More detail on the physics of the early universe can be found in Section 1.2.1.

As the symmetry was broken, a less general symmetry emerged, and the vacuum state became invariant under a new symmetry product $SU(3)_C \times U(1)_{EM}$ at low energies O(100 GeV) through the process known as Higgs mechanism. A consequence of this is the emergence of a new spin-0 boson, the Higgs boson. The Higgs boson is associated with a field called the Higgs field. This field interacts with other particles and gives them mass. Similar to how objects moving through a medium like water encounter resistance, particles moving through the Higgs field acquire mass. The interaction with the Higgs field is responsible for the masses of particles [25].

The existence of the Higgs field was postulated in the Brout-Englert-Higgs mechanism (BEH) by Peter Higgs, Robert Brout and François Englert in the 1960s [26, 27, 28, 29,

30] long before the discovery of the Higgs boson. Without the spontaneous symmetry breaking, the masses of the W and Z boson could not be described in the SM. Also, due to the chiral structure of the $SU(2)_L$, fermion masses would break the $SU(2)_L$ invariance of the Lagrangian (cf. Section 1.1.4) and thus be not allowed [31]. In essence, without the Higgs mechanism, the symmetries of the SM would not allow for the generation of particle masses, contradicting experimental observations.

In the Brout-Englert-Higgs mechanism, a further scalar field (Higgs field/boson) is required, which has a non zero vacuum expectation value (see also next section). Such a scalar field was found at the LHC in 2012, leading to François Englert and Peter Higgs being awarded with the Nobel Prize in Physics in 2013 [32]. The discovery of a new particle and the confirmation of a new type of interaction was the beginning of a new era of particle physics and cosmology.

1.1.4 Standard Model Lagrangian

Since the SM is a quantum field theory, it can be formulated as a Lagrangian that captures the dynamics of the known particles, similar to the classical mechanics. The construction of such Lagrangian follows a general procedure. First, the principles of Lorentz invariance and gauge invariance are postulated to ensure that the laws of physics remain unchanged in different observer frames and possess specific symmetries.

Starting from these fundamental symmetries, the most comprehensive renormalizable Lagrangian is formulated. This Lagrangian incorporates all the observed field excitations (particles) and interactions observed in Nature so far. The complete Lagrangian of the SM can be represented as follows:

$$
\begin{aligned}
\mathcal{L}_{\text{SM}} = &-\frac{1}{4} B^{\mu\nu} B_{\mu\nu} - \frac{1}{4} W_a^{\mu\nu} W_{\mu\nu a} - \frac{1}{4} G_a^{\mu\nu} G_{\mu\nu a} \\
&+ \sum_\psi \bar{\psi} i \gamma_\mu \partial^\mu \psi \\
&+ \sum_{\psi_L} \bar{\psi}_L i \gamma_\mu (ig \frac{\sigma_a}{2} W_a^\mu + ig' \frac{Y}{2} B^\mu) \psi_L \\
&+ \sum_{\psi_R} \bar{\psi}_R i \gamma_\mu (ig' \frac{Y}{2} B^\mu) \psi_R \\
&+ \sum_{\psi = q} \bar{q} i \gamma_\mu (ig_s \frac{\lambda_a}{2} G_a^\mu) q \\
&+ \mid (\partial^\mu - ig \frac{\sigma_a}{2} W_a^\mu - ig' \frac{Y}{2} B^\mu) \phi \mid^2 \\
&- \left(\mu^2 \mid \phi \mid^2 + \lambda \mid \phi \mid^4 \right) \\
&- \sum_\psi Y_{ij}^\psi \bar{\psi}_{L,i} \phi \psi_{R,j} \quad + \text{ h.c.}
\end{aligned}
\tag{1.4}
$$

11

In the SM Lagrangian, the gauge couplings, denoted by g, g' and g_s represent the strength of the interactions and the index a refers to the different field-strength tensors and generators of the three gauge groups, respectively. The gamma matrices γ^μ and the covariant form of the gamma matrix γ_μ are related through the metric tensor by $\gamma_\mu = g_{\mu\nu}\gamma^\mu$. The Einstein convention is applied to all indices occurring in the equation. The last line of Equation 1.4 is completed by the hermitian conjugate (h.c.) of the previous term.

Let's break down the different components of the Lagrangian:

- The first line in Equation 1.4 describes the kinetic energy and self-interaction of the gauge bosons. The field-strength tensors $B^{\mu\nu}, W_a^{\mu\nu}, G_a^{\mu\nu}$ encode the information about the interactions between particles.

- The second line describes the kinetic energies of all Dirac fermions ψ.

- The third line comprises interaction terms for all left-handed fermion doublets, e.g., $\psi_L = (\nu_e, \ e)_L$ resulting from the $U(1)_Y \times SU(2)_L$ gauge group. The gauge fields W_a^μ with $a = 1, 2, 3$ and B^μ represent the $U(1)_Y$ and $SU(2)_L$ gauge fields, respectively.

- The fourth line and the second summand in the third line represent the behaviour of the fermions ψ, $\bar\psi$ under the $U(1)_Y$ gauge interaction.

- The fifth line describes the strong interaction governed by QCD and involves transformations for quarks $\psi_q = q$ and gluons G_a^μ under the $SU(3)_C$ gauge group.

- The sixth and seventh lines represent the scalar part of the $SU(2)_L \times U(1)_Y$ Lagrangian, including interactions between the gauge fields and the scalar field (Higgs field).

- The last line describes the interaction of fermions with the Higgs boson, known as Yukawa interactions.

The Lagrangian can be split into a free-field and an interaction component. Free particles are described by a mass term and a kinematic term, describing the propagation of the fields. Therefore, the Lagrangian can be decomposed into a mass term, a coupling term and a kinetic term for each field in the theory.

To calculate the interactions, field-strength tensors are used, which contain the gauge coupling constant g and the structure constant f^{abc} of the specific gauge group. For a given gauge field A, the field strength tensor is:

$$F_{\mu\nu}^a = \partial_\mu A_\nu^a - \partial_\nu A_\mu^a + g f^{abc} A_\mu^b A_\nu^c. \tag{1.5}$$

The structure constant is defined by the commutator of the generators t_i of the gauge group: $[t_a, t_b] = i \ f^{abc} \ t_c$ [33]. In an abelian group the structure constant vanishes since all generators commute. The SM includes the abelian group $U(1)_Y$, and the non-abelian

groups $SU(3)_C$ and $SU(2)_L$.

The covariant derivative
$$\gamma^\mu D_\mu = \gamma^\mu (\partial_\mu - iqA_\mu), \tag{1.6}$$

comprises the kinetic energy term for fermions, the gauge field A_μ, and the respective charge q of an interaction.

Finally, with the use of field-strength tensors and the covariant derivative the individual contributions of the fundamental interactions can be separated.

In quantum electrodynamics (QED), for leptons with masses m, the partial Lagrangian is
$$\mathcal{L}_{\text{QED}} = \bar{\psi}(i\gamma_\mu D^\mu - m)\psi - \frac{1}{4}F_{\mu\nu}F^{\mu\nu}. \tag{1.7}$$

The relevant charge q is the electric charge eQ here and the vector field A^μ corresponds to the photon field.

In QCD, for quarks with masses $m = m_q$, the respective part of the Lagrangian is
$$\mathcal{L}_{\text{QCD}} = \sum_{\psi=q} \bar{q}(i\gamma_\mu D^\mu - m_q)q - \frac{1}{4}F^a_{\mu\nu}F^{\mu\nu}_a. \tag{1.8}$$

Here, the relevant charge q is the color charge and A_μ is a color-charged gluon G^μ_a of $SU(3)_C$. In this case, the generator is given by $t_a = \frac{\lambda_a}{2}$ with the eight Gell-Mann matrices λ_a [34].

In the electroweak interaction for fermions ψ the partial Lagrangian is
$$\mathcal{L}_{\text{EW}} = \sum_{\psi=l,q} \bar{\psi}(i\gamma_\mu D^\mu)\psi - \frac{1}{4}W^a_{\mu\nu}W^{\mu\nu}_a - \frac{1}{4}B_{\mu\nu}B^{\mu\nu}. \tag{1.9}$$

A superposition of the fields W^a_μ, with $a = 1, 2, 3$ and B_μ leads to the eigenstates $W^\pm$, Z, and γ. The respective generator are $I_a = \frac{\sigma_a}{2}$, with the three Pauli matrices σ_a, whose eigenvalues give the weak isospin, which is the relevant charge for $SU(2)_L$.

In the unification of $U(1)_Y \times SU(2)_L$, the individual charges of the QED and the weak interaction are combined to a so-called hypercharge Y. The hypercharge is given by the electric charge Q and the third component of the weak isospin I_3 as $\frac{Y}{2} = Q - I_3$. Thus, $U(1)_Y$ is similar to electromagnetism, but unlike QED, it acts on weakhypercharged particles of both chiralities via the Z boson and on charged particles via the photon. Consequently, both, left and right-handed fermions interact with the the $U(1)_Y$ gauge field B^μ. In contrast, right-handed fermions which form singlets under $SU(2)_L$, (e.g. $\psi_R = e_R$ or $\psi_R = u_R$), do not interact with the $SU(2)_L$ gauge field W^μ. In result, D_μ differs for left-handed and right-handed fermion fields.

The introduced scalar Higgs field ϕ to the Lagrangian adds a spontaneous symmetry breaking term and a Yukawa coupling term to all fermions:

$$\mathcal{L}_{\mathrm{H}} = \mathcal{L}_{\mathrm{SSB}} + \mathcal{L}_{\mathrm{Yukawa}}. \tag{1.10}$$

The spontaneous symmetry breaking term is given by:

$$\mathcal{L}_{\mathrm{SSB}} = (D_\mu \phi)^\dagger (D^\mu \phi) - V(\phi), \tag{1.11}$$

which expands to:

$$\mathcal{L}_{\mathrm{SSB}} = \mid (\partial^\mu + ig\frac{\sigma_a}{2}W_a^\mu + ig'\frac{Y}{2}B^\mu)\phi \mid^2 - V(\phi), \tag{1.12}$$

with the Higgs potential

$$V(\phi) = \mu^2 \mid \phi \mid^2 + \lambda \mid \phi \mid^4 . \tag{1.13}$$

The square of the covariant derivative D^μ in Equation 1.11 leads to three and four-point interactions between the gauge fields and the Higgs field. Subsequently, Equation 1.12 contains a kinetic term and a mass term for the Higgs field as well as interactions between the gauge fields and the Higgs field, with quadratic terms in W^μ and B^μ, that give rise to masses for the W and Z boson.

To see the direct relation between the Higgs potential and the masses of the gauge bosons, the interaction eigenstates $(W_{1,2,3}^\mu, B^\mu)$ of the gauge bosons have to be related to the mass eigenstates via the Weinberg angle $\theta_W = \frac{g'}{\sqrt{g^2 + g'^2}}$, which yields:

$$\begin{aligned} M_H &= \sqrt{2}\mu \\ M_W &= \frac{g}{\sqrt{2}}\nu \\ M_Z &= \frac{1}{\sqrt{2}}\nu\sqrt{g^2 + g'^2} \\ M_\gamma &= 0. \end{aligned} \tag{1.14}$$

As can be seen, the massless photon does not obtain a mass term through the Higgs mechanism, while the Higgs boson itself obtains a mass through the potential. The λ term of the Higgs potential describes a quartic self-interaction of the scalar Higgs fields. The potential of the Higgs field is also known as the Mexican Hat potential. In Figure 1.1, the spontaneous symmetry breaking in the Mexican Hat potential is illustrated.
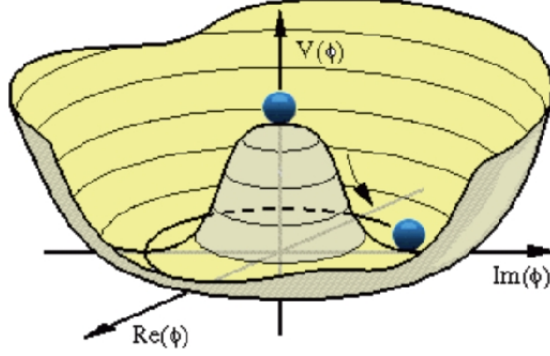
Figure 1.1: The phenomenon of spontaneous symmetry breaking illustrated for the case of the Higgs potential: going from regions of higher field strength towards the ground (vacuum) state, the form of the Higgs potential resembles that of a symmetric Mexican Hat. A ball placed in the middle of that potential at some point has to choose spontaneously one point on the brim of the hat as ground state to rest in. This leads to an asymmetric outcome despite being in a symmetric potential [35].

Minimizing Equation 1.13 leads to

$$|\phi|^2 = -\frac{\mu^2}{2\lambda}. \tag{1.15}$$

The spontaneous symmetry breaking is introduced if the Higgs filed has a non-vanishing vacuum expectation value $\langle\phi\rangle = \nu$. For the complex scalar Higgs field $SU(2)_L$ doublet

$$\phi = \frac{1}{\sqrt{2}} \begin{pmatrix} \phi^+ \\ \phi^0 \end{pmatrix}, \tag{1.16}$$

this holds if ϕ^+ is set to zero, which is possible in a unitary gauge, and if the mass parameter μ^2 in the Higgs potential is smaller than zero while the parameter λ is greater than zero. In that case, choosing a point in the minimum (vacuum state) spontaneously breaks the rotational symmetry of $\mathcal{L}_{\mathrm{SSB}}$ under $SU(2)_L \times U(1)_Y$ such that only the $U(1)_Q$ of electromagnetism remains.

The interaction of the Higgs field with fermions is given by the Yukawa interaction term of Equation 1.10. Similar to gauge boson masses, fermion mass terms can be obtained after spontaneous symmetry breaking, with

$$\mathcal{L} \propto - \left(\sum_{\psi} M_{ij}^{\psi} \bar{\psi}_L \psi_R \right) + h.c. \tag{1.17}$$

15

Here, $M_{ij}^\psi = Y_{ij}^\psi \, \nu$ are mass matrices containing the Yukawa coupling parameters Y_{ij} of the fermions to the Higgs field. These parameters are free parameters that are not predicted by the theory but only determined experimentally.

Among the fermions, neutrinos are unique in that they were initially treated as massless in the SM (Yukawa couplings for neutrinos were not included), and only the left-handed component couples to the weak force in the SM. Thus, neutrinos are not be described as Dirac particles in the SM because the left-handed component of a Dirac particle's spinor corresponds to one helicity state (handedness), and the right-handed component corresponds to the other helicity state. Therefore, massless neutrinos are described as left-handed Weyl spinors. The discovery of non-zero neutrino masses, was made through observations of neutrino oscillations, where a deficit of electron neutrinos in the flux of solar neutrinos indicated a superposition of different neutrino mass eigenstates [36]. In this and following experiments the neutrino masses have been experimentally bounded (cf. Table 1.1). To give neutrinos mass the concept of right-handed neutrinos, or sterile neutrinos can be introduced. These right-handed neutrinos are singlets under the weak force, and their presence allows for the generation of neutrino masses through the seesaw mechanism. In the see-saw mechanism, right-handed neutrinos are heavy, while left-handed neutrinos are light. Through the interaction of the two sets of neutrinos, the mechanism can explain why the neutrinos we observe are so much lighter than other elementary particles [37]. An alternative way to introduce massive neutrinos is through majorana neutrinos. Majorana neutrinos are described by Majorana spinors, which are special types of spinors that are their own antiparticles. The Majorana nature of neutrinos allows for a different type of neutrino mass generation mechanism. The mass term for Majorana neutrinos involves a right-handed neutrino singlet component, and this mass term does violate lepton number conservation [38]. The nature of neutrinos, whether they are Dirac or Majorana fermions is subject to experimental efforts, such as neutrinoless double-beta decay searches [39], that aim to determine whether neutrinos are Majorana particles by observing a process that would be forbidden for Majorana neutrinos but allowed for Dirac neutrinos.

Taking into account all the partial Lagrangian above, the final SM Lagrangian can also be rewritten as:

$$\mathcal{L}_\text{SM} = \mathcal{L}_\text{QED} + \mathcal{L}_\text{QCD} + \mathcal{L}_\text{EW} + \mathcal{L}_\text{H}. \tag{1.18}$$

1.1.5 Beyond the Standard Model Physics

While the SM is able to describe a large range of phenomena and measurements in particle physics and cosmology, it also leaves some big questions wide open, and a number of measurements can not be described within it.

One particularly noteworthy example is the fundamental force of gravity, which is not accounted for in the model. The mathematical formalism and underlying principles of gravity are described by Einstein's theory of general relativity. The SM is inherently a quantum field theory, which means that it describes particles and their interactions at small energy scales. General relativity, on the other hand, does not easily fit into the quantum framework. Efforts to quantize gravity have led to theoretical difficulties and inconsistencies, such as infinities in certain calculations (a problem known as non-renormalizability). The quest for a theory that unifies gravity with the other forces is an ongoing endeavor in theoretical physics and has led to BSM theories such as string theory and loop quantum gravity [10].

One further problem is the hierarchy or naturalness [18]. The principle of naturalness, pioneered by G. 't Hooft [40], is a basic concept in theoretical physics, addressing the subtle balance between fundamental constants and the scales of physical processes. It is prominent in the context of a hierarchy problem, which results from the large discrepancy between the weak and Planck scales of $\sim 1.22 \times 10^{19}$ GeV, which is the scale up to which the predictions of the SM should be reconcilable. This discrepancy leads to concerns about the stability of the non-zero average value of the Higgs field and the sensitivity of its mass to quantum corrections. In quantum field theory, virtual particle-antiparticle pairs continuously pop in and out of existence, creating a sea of quantum fluctuations. These fluctuations can affect the Higgs field, causing its average value to become unnaturally small or large. However, the observed Higgs mass (about 125 GeV) [22, 23] remains significantly lower. Naturalness considers a theory more appealing if no excessive fine-tuning is required to maintain observed values. In that context, fine-tuning refers to the precise adjustment of parameters to counteract large corrections, a scenario considered less elegant.

Problems of a similar nature, involving suspicion about free parameters or physical constants that seem unlikely to be coincidental, encompass challenges such as the absence of unification of the electroweak and strong interactions for large energies [41, 42], as well as the origin of the number of the fermion generations.

In rare cases, the SM provides an incomplete description of the behavior of the known particles. There are, for example, indications that the SM may not fully describe the g-2 anomaly, which refers to a discrepancy between the predicted and observed values of the magnetic moment of certain particles. The experiment that revealed the g-2 anomaly took place at the Brookhaven National Laboratory in the 1990s and early 2000s, known as the E821 experiment [43]. In this experiment, muons were subjected to a magnetic field while they circulated in a storage ring. By precisely measuring the magnetic moment of the muons, scientists aimed to compare the results with the predictions of the SM. The

g-2 anomaly has since then led to ongoing experiments, such as the muon g-2 experiment at Fermilab [44, 45].

Finally, astrophysical observations suggest that less than 5 % of matter-energy content in the universe be made of visible matter, while by far the largest amount (about 27 %) is dark matter and dark energy (about 68 %) [11, 46, 12]. *Dark* here means invisible, in the sense that it neither emits nor absorbs light, and is only confirmed to interact through the gravitational force. DM cannot be explained within the SM since the SM contains no candidate particle with suitable properties to explain the total amount of DM observed in the universe. DM is further discussed in the following section.

The points raised above, in addition to other considerations, suggest that the SM be only valid within a limited scope, for energies up to perhaps 100 GeV or 1 TeV. There is ample evidence to motivate the development of theories beyond the SM. Numerous extensions to the SM have been proposed where some of the most well-motivated and extensively researched are supersymmetric extensions. These supersymmetric extensions of the SM predict new fields, which may be discovered by particle experiments at the energy frontier, such as the CMS and ATLAS experiments at the Large Hadron Collider.

1.2 Dark Matter

The previous section explored how the nature of DM challenges the SM, standing as one of the most striking open questions in modern physics and supersymmetry has been suggested as a way to confront this challenge. Nonetheless, characteristics of potential DM particles remain uncertain. This section connects the dots to the mysterious realm of DM, exploring the progression from the early universe to particle physics and BSM searches at collider experiments.

Many arguments concerning the nature of DM, especially from astrological observations, rely on assumptions about the state of the universe and its matter shortly after its beginning. The most accepted model to describe the early universe and its development until today is the model of cosmology, which is briefly introduced in the first part of this section. Based on that, motivation for DM from cosmological observations and arguments is given. While alternative theories attempt to explain DM without postulating new particles, such as modified Newtonian dynamics (MOND), the leading and most substantiated explanation is that one or more particles exist, which are neutral, stable and posses other properties needed to explain the relic abundance of DM observed in the universe today. This section concludes by discussing potential DM candidate particles and the underlying theoretical frameworks.

1.2.1 Early Universe

The most widely held theory for the evolution of the universe is the SM of cosmology or big-bang model. It describes how the universe expanded from an initial state of high density and temperature to the observable universe today consisting of dark energy, DM,

and visible (or baryonic) matter. It offers a comprehensive explanation for a broad range of observed phenomena, including the abundance of light chemical elements, the cosmic microwave background (CMB) radiation, and large-scale structures [47, 48, 49].

The big-bang model is based on two key assumptions. Firstly, it assumes that Albert Einstein's general theory of relativity accurately describes the gravitational interaction of all matter. Secondly, the cosmological principle is introduced as the second assumption, asserting that an observer's perception of the universe remains independent of the direction he looks or his specific location. While this principle is applicable only to the large-scale properties of the universe, it implies a universe without an edge. Consequently, the big-bang origin is not localized to a specific point in space but is distributed uniformly throughout space at the same time. These two assumptions enable the calculation of the cosmos's history post a defined epoch known as the Planck time. Nevertheless, scientists are yet to discern the prevailing conditions before the Planck time.

The big bang model has its name from the initial state of the universe of extreme temperature and density, known as the big bang, which expanded outward initially at superluminous rates, a phenomenon referred to as inflation. Extrapolating the expansion of the universe as observed today backwards in time using general relativity yields an infinite density and temperature at a finite time in the past. That initial event is thus referred to as a singularity. Based on measurements of the expansion of the universe using supernovae [50] and measurements of temperature fluctuations in the cosmic microwave background [51], the time that has since transpired is approximately 13.8 billion years.

To the current knowledge, the most remarkable stages in the history of the universe are the following [52].

- Singularity: infinitely dense and hot point in space and time;

- Inflation and baryogenesis

  - planck epoch up to 10^{-43}s: universe was filled homogeneously and isotropically with a very high energy density, huge temperatures of 10^{32} degrees Celsius and pressures; the four fundamental forces were unified as one;

  - grand unification epoch: gravity separated from other forces; rapid expansion and cooling;

  - phase transition at approx. 10^{-37}s: caused a cosmic inflation; universe grew exponentially;

  - electroweak epoch at approx. 10^{-36}s: strong nuclear force separated; only electromagnetic force and weak nuclear force remained unified

  - inflation stop and reheating after 10^{-33} to 10^{-32}s: production of quark–gluon plasma and other elementary particles; particle–antiparticle pairs of all kinds were continuously created and destroyed in collisions;

19

– baryogenesis: violation of the conservation of baryon number, leading to a small excess of quarks and leptons over antiquarks and antileptons; resulting in the predominance of matter over antimatter in the present universe;

- cooling at approx. 10^{-11}s: density decreased; fall in temperature; symmetry-breaking phase transitions; particle energies dropped to values attainable at particle accelerators; quarks and gluons combined to form baryons, (e.g., protons and neutrons); temperatures no longer high enough to create proton–antiproton or neutron–antineutron pairs; mass annihilation of nearly all matter and all anti-matter;

- nucleosyhthesis after few minutes: neutrons and protons formed helium and deuterium;

- recombination: electrons and protons combined to atoms, mostly neutral hydrogen; atoms were able to emit radiation (CMB) (after $\approx$ 379,000 years);

- structure formation: denser regions gravitationally attracted nearby matter, forming gas clouds, stars, galaxies, and the other astronomical structures observable today;

- cosmic acceleration: expansion of the universe is accelerating [53]; can be explained assuming dark energy (i.e., a positive cosmological constant Λ).

The timeline can also be illustrated in terms of the radiated waves and the expansion of the universe in the big bang model, as shown in Figure 1.2.

A widely accepted parameterization of the big bang model is given by the Lambda Cold DM (ΛCDM) model. The cosmic evolution after the inflationary epoch can be described and modeled using quantum mechanics and general relativity. It is a specific version of the big bang model that incorporates additional details about the composition of the universe. In the model, the universe is composed of three main components: dark energy, which is represented by the cosmological constant Λ; cold DM (CDM), a hypothetical type of matter; and ordinary matter. While cold DM consist of particles that move relatively slowly and are cold in terms of their velocities. Cold DM is the prevailing assumption in the ΛCDM model. In contrast, warm DM refers to a hypothetical type of DM with particles that have higher velocities compared to cold DM. Warm DM particles are still non-relativistic but have higher kinetic energy. The hypotheses of cold DM and warm DM address different challenges and discrepancies in cosmological observations and simulations.

The ΛCDM model effectively explains the presence and structure of the CMB, the large-scale arrangement of galaxies, the observed abundance of hydrogen (including deuterium), helium, and lithium and the observed phenomenon of the universe's accelerating expansion [55].
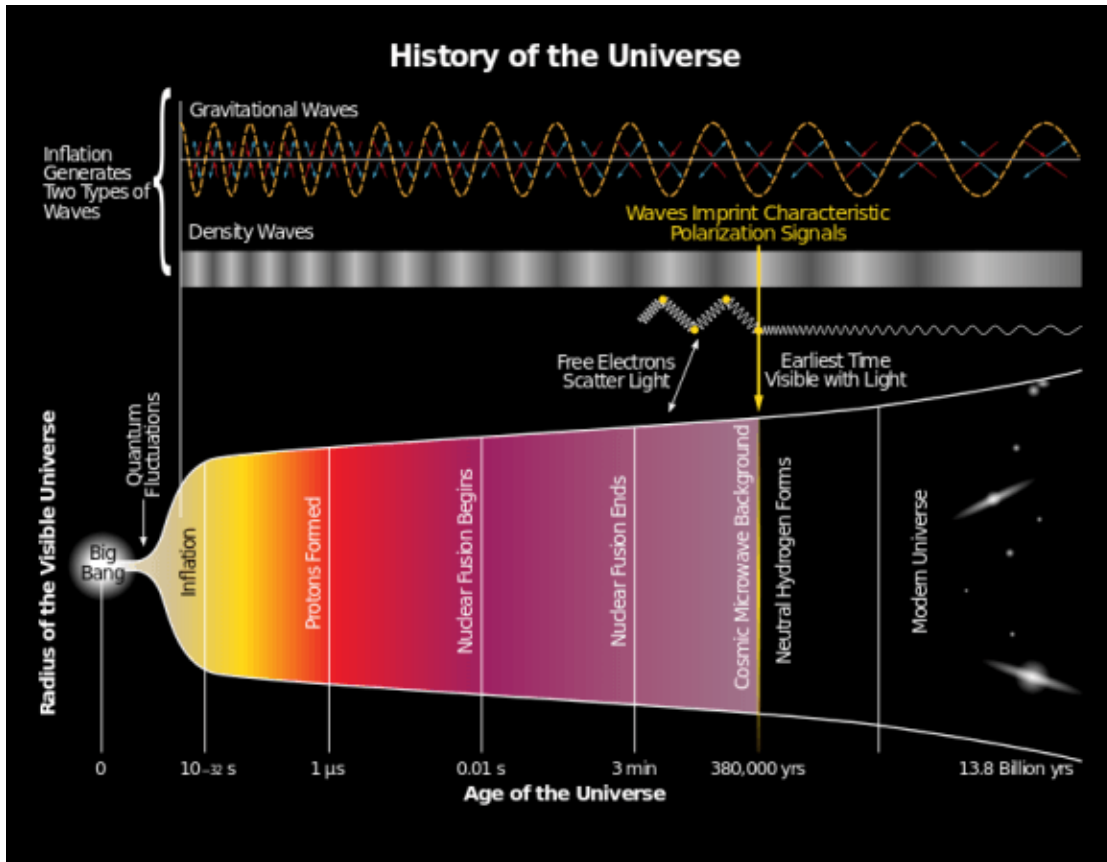
Figure 1.2: Timeline of the evolution of radiated waves (top) and the metric expansion of the Universe (bottom) from the inflation to the current epoch; from the left: first the dramatic expansion occurs in the inflationary epoch, followed by the cooling epoch, where the formation of first baryons such as protons and neutrons, and later nucleosynthesis, began; after that, to the right, the forming of gas clouds, stars, galaxies, and the other astronomical structures occurred in the structure epoch [54].

1.2.2 Evidence for Dark Matter

Astronomers have long proposed yet undetectable forms of matter, either because they are too far away, too dim, or intrinsically invisible.

In 1933, Fritz Zwicky, examined the redshifts of various galaxy clusters and observed a significant dispersion in the apparent velocities of eight galaxies within the Coma Cluster. Applying the virial theorem [56] establishes a relationship between the kinetic and potential energies of a system of particles and provides an estimate for the mass of the cluster. An analysis carried out by his graduate student Vera Rubin predicted the velocity of stars within the galaxy around 80 km/s, while the observed average velocity along the line of sight was an order of magnitude larger, approximately 1000km/s. From

21

this comparison, Zwicky concluded: "If this would be confirmed, we would get the surprising result that dark matter is present in much greater amount than luminous matter" which is the first identified mention of DM in literature [57].

In the 1970s, based on comparisons between predicted and measured rotation curves of spiral galaxies, the consensus grew that DM was indeed abundant in the universe. If all of the matter in galaxies were luminous, a given galaxy's distribution could be estimated as a point mass in the center with test masses orbiting around it, similar to the solar system. The rotational velocity for a stable Keplerian orbit is then given from Kepler's Second Law [58] by

$$v(r) = \sqrt{\frac{G * m(r)}{r}}, \tag{1.19}$$

where G is the gravitational constant, $m(r)$ is the total mass contained within r, and r is the radius from the galactic central point. Measurements yield approximately constant velocities for the most distant galactic objects, while at large distances r from the galactic center, the velocity of luminous objects is expected to decrease with $v(r) \propto \sqrt{1/r}$. However, the observed rotation curves are seen to increase with r, as can be seen in Figure 1.3. This indicates that the total mass distribution in spiral galaxies is not similar to that of the solar system, but of a more uniform, spread out distribution. These are strong indications for non-luminous matter (DM). As DM apparently does not interact with the electromagnetic field, which means it does not absorb, reflect, or emit electromagnetic radiation, it is invisible to astronomical detection techniques [11, 46].

Different kinds of studies of clusters of galaxies gives further insight to the characteristics of DM in the universe, including its overall abundance. The effect known as gravitational lensing is used, which is the bending of light through the distribution of matter. It can become a large effect in the presence of vast quantities of mass, such as in galaxy clusters. Gravitational lensing studies of the Bullet Cluster (1E 0657-56), which consists of two colliding clusters of galaxies, show that the center of mass of each cluster is far displaced from the baryonic center of mass [61, 62]. The major components of the Bullet Cluster are stars, gas and the putative DM. While the stars of the galaxies, were not greatly affected by the collision, and mostly passed right through, the hot gas that represents most of the baryonic (visible) matter, interacted during the collision electromagnically and thereby increased in temperature and slowed down. The majority of the clusters' total mass however continued to move along its original trajectory as gravitational lensing showed, which is an other indication of a potentially particle like DM [12]. The Bullet Cluster observations have also been argued to support the hypothsis of cold DM over competing theories that can explain observed galaxy rotation curves, in particular MOND. In MOND, the lensing would be expected to follow the baryonic matter;

A further milestone in the investigation of DM, was the observation of anisotropies in the CMB radiation, measured first in 1992 by the NASA satellite Cosmic Background Explorer (COBE). The cosmic microwave background is microwave radiation that fills
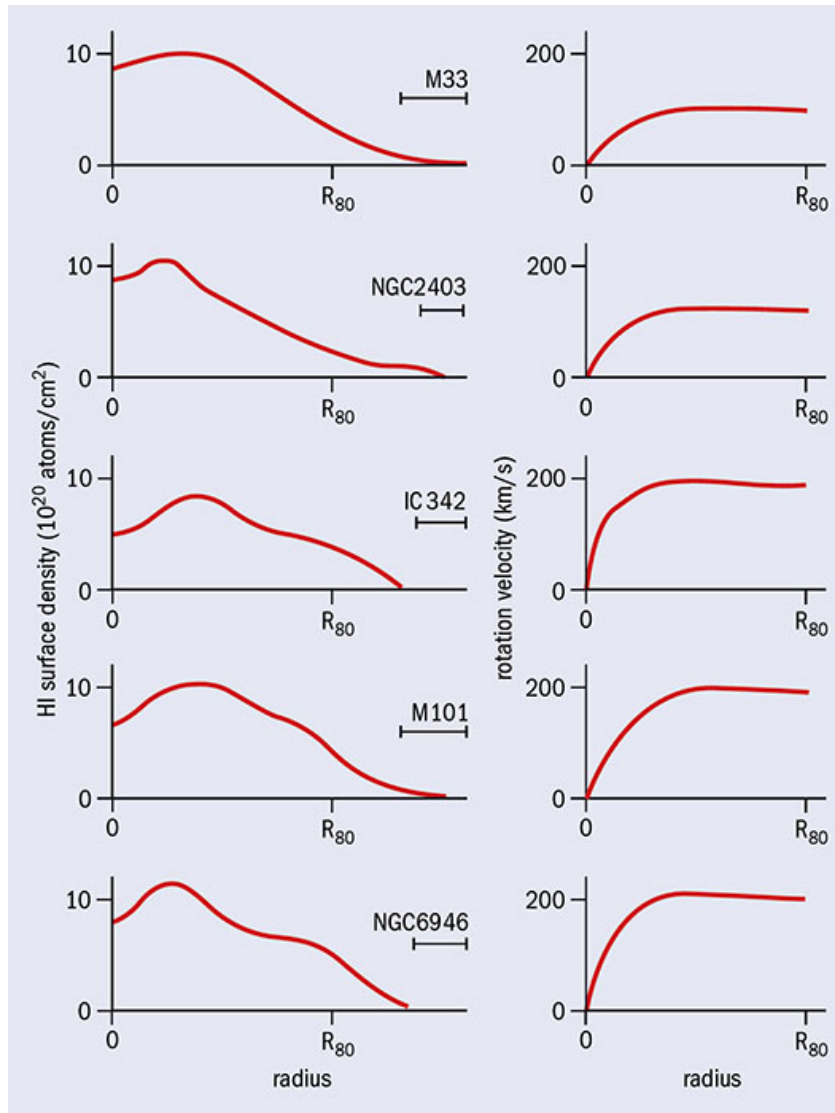
Figure 1.3: Flat rotation curves for galaxies, which indicate they are spinning faster than expected if they were made purely from baryonic matter, from observations in the early 1970s. Shown are the hydrogen surface density profile (left) and rotation curves (right) of five galaxies as obtained by D.H. Rogstad and G.S. Shostak in 1972, where the bars under the galaxy names indicate their average radial diameter and R80 corresponds to the radius containing 80% of the observed hydrogen [59] [60].

all space in the observable universe and can be detected with a sufficiently sensitive radio telescope. All radiation from the sky we measure today comes from a spherical surface called the surface of last scattering. This represents the set of locations in space at which the decoupling of bound matter and free photons occurred. The CMB is

23

estimated to originate from a point in time such that the photons from that distance have just reached observers. During the earliest periods, the universe was filled with an opaque fog of dense, hot plasma of sub-atomic particles. Thus all ordinary matter was ionized and interacted strongly with radiation via Thomson scattering. As the universe expanded, this plasma cooled to the point where protons and electrons combined to form neutral atoms of mostly hydrogen (cf. Section 1.2.1). Unlike the plasma, these atoms could not scatter thermal radiation by Thomson scattering, and so the universe became transparent. In this recombination epoch, photons were released to travel freely through space. Over time, the photons have grown less energetic, since the expansion of space causes their wavelength to increase.

In contrast to baryonic matter, DM does not interact directly with radiation, but it does affect the CMB by its gravitational potential and by its effects on the density and velocity of ordinary matter. Ordinary and DM perturbations, therefore, evolve differently with time and leave different imprints on the CMB. The angular scale and height of the acoustic peaks in the power spectrum of the CMB photon oscillations give a precise estimate of the total energy density in the universe as well as the baryonic fraction, and the DM component. Currently, this yields a fraction of 4.9% baryonic matter, 26.8% DM and 68.3% dark energy [63]. The latter is a form of energy that permeates all of space. It is often referred to as a cosmological constant or a form of energy associated with empty space. It is modeled as having negative pressure and causes an accelerated expansion of the universe (cf. Section 1.2.1), counteracting the gravitational pull of matter [50]. However, the fundamental constituents and properties of dark energy remain a topic of active research and exploration [2].

In Figure 1.4, a linear combination of temperature maps is given that the ESA Planck observatory surveyed in nine broad frequency bands. It shows one of the most recent pictures of the anisotropies of the CMB.

Global fits of cosmological parameters to multiple observations for the thermal relic density of cold, non-baryonic matter yield [24]

$$\Omega_{\mathrm{nbm}} h^2 = 0.1186 \pm 0.0020. \tag{1.20}$$

Here, h denotes the reduced Hubble constant $h = H_0/100 \times \frac{\mathrm{Mpc}}{\mathrm{km/s}}$ The resulting density is significantly larger than the baryonic matter density

$$\Omega_{\mathrm{b}} h^2 = 0.02226 \pm 0.00023. \tag{1.21}$$

1.2.3 Dark Matter Particle Candidates and Detection Methods

Searches for new particles that make up DM are supported by the previously discussed cosmological findings. In principle, a massive astrophysical compact halo object (MACHO), a type of massive celestial body of baryonic matter, could explain the apparent
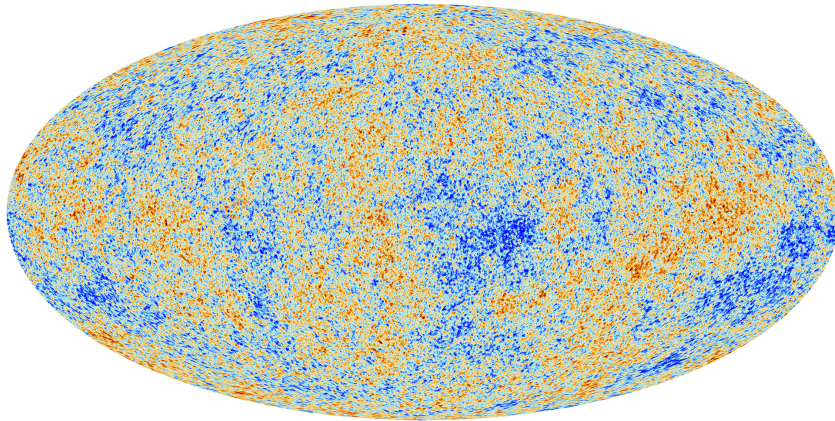
Figure 1.4: The anisotropies of the cosmic microwave background as observed by the ESA Planck satellite shown in galactic coordinates filtered from any unwanted background. Tiny temperature fluctuations correspond to regions of slightly different densities, representing the seeds of all structure (e.g., stars, galaxies) observed today [64].

presence of DM in galaxy halos. However, the observations from CMB elaborated above disfavor purely baryonic DM. In addition, the production of light elements such as hydrogen and helium occurred through the process of big bang nucleosynthesis, and the resulting relative abundance of elements in the universe is relatively well understood. If there were more baryons, there should also be more helium, lithium and heavier elements synthesized during the big bang. The observed abundances suggest that baryonic matter makes up between 4–5% of the universe's critical density, which is consistent with $\Omega_{\rm b} h^2$ given above (cf. Equation 1.21).

A viable particle candidate for non-baryonic DM is required to be stable, electrically neutral, and non-interacting via the strong force. Additionally, it should account for the correct relic density, $\Omega_{nbm} h^2$ (cf. Equation 1.20). These requirements can be satisfied by macroscopic objects like primordial black holes, bosons and fermions, as well as axion-like particles [65], sterile neutrinos [66], or weakly interacting massive particles (WIMPs) [17]. Among these possibilities, the WIMP paradigm is particularly interesting as WIMPs are electrically neutral stable particles that can potentially be directly produced in collider experiments involving TeV-scale collisions. Consequently, dedicated searches focus on detecting WIMPs as a potential solution for DM [67] including this thesis.

1.2.3.1 Weakly Interacting Massive Particles

WIMP are DM candidates that interact via the electroweak force and have a mass between 10 GeV and 1 TeV. The SM does not provide a viable WIMP candidate. Even though, in principle, neutrinos interact weakly and are electrically neutral, neutrino masses are constrained to $m_\nu < 0.13$ eV [68], and thus can not account for the correct cosmological density alone. In the ΛCDM model, WIMPs can yield the correct relic

25

density via thermal production with a self-annihilation cross section on the order of the electroweak scale ($O(\mathrm{pb})$) [24].

Many WIMP candidates are expected to have been produced thermally in the early universe, similarly to the particles of the SM, assuming a thermal and chemical equilibrium of WIMPs and SM particles after the inflation in the early universe. At that state of the universe, particles and antiparticles were forming and annihilated into lighter particles. The rate of annihilation between WIMPs and SM particles is given by the cross section multiplied by the WIMP velocity. As the universe expanded and cooled, the average thermal energy of lighter particles became insufficient to form a DM particle-antiparticle pair. However, the annihilation of the DM particle-antiparticle pairs continued, and the number density of DM particles decreased exponentially (cf. cooling epoch in Section 1.2.1). When the universe was about one second old and had cooled to temperatures around a few billion degrees Kelvin, the WIMPs no longer annihilated due to the decreased particle density, which is referred to as freezeout. The number of DM particles remained (roughly) constant as the universe continued to expand. This chain of arguments thus supports the theory of WIMPs with cross sections on the order of the electroweak scale.

1.2.3.2 Indirect Detection

DM candidate particles may annihilate with each other, and thereby produce indirect signals. Indirect detection of DM is a method of searching for SM final state particles emanating from the annihilation of DM particles. Searches use observations of photons, protons, electrons, and neutrinos.

Gamma-ray telescopes such as the H.E.S.S. Cherenkov telescopes [69] and FERMI-LAT [70] are one type of indirect search. Especially the mass scale of WIMP DM implies that a sizable fraction of the emission generated by annihilation and decays happens at gamma-ray energies. Gamma rays travel to the observer without deflection, allowing mapping of the sources of the signal. Through their prompt emission, gamma rays carry important spectral information that can be used to characterize the DM particles in the case of a detection. The H.E.S.S. Cherenkov telescopes point to the center of the galaxy, which is expected to contain a high DM density.

Similar to gamma rays, neutrinos also preserve spectral information and point back to the source. Detection of astrophysical neutrinos generally involves instrumenting a massive and large volume of material, for example water or ice, detecting the Cherenkov light produced in the detector medium from neutrino interactions as neutrinos pass through it. Such an experiment is realized in the IceCube observatory, for example [71]. Consisting of a cubic kilometer of ice at the south pole, instrumented with photomultiplier tubes to detect Cherenkov light, IceCube has a large enough volume to potentially detect WIMP annihilation products.

Finally, space-based instruments to detect charged cosmic rays, such as the PAMELA [72] or AMS [73] detectors, are sensitive to the charge of incoming particles, and therefore

capable of determining the relative flux of particles and anti-particles, which may originate from WIMP annihilations. Differences in the high-energy positron and electron fluxes are measured and used to constrain the annihilation rate of certain classes of DM.

Strong limits on the DM annihilation cross section have been obtained from gamma-ray telescopes and gamma-ray detectors [74]. A combination of data from observations of 20 dwarf galaxies by FERMI-LAT, HAWC, H.E.S.S., MAGIC and VERITAS, assuming 100% annihilation of DM to $\tau^+\tau^-$ is given in Figure 1.5. Cross section bounds are determined depending on the WIMP mass m_{DM} and reach down below a DM mass of 200 GeV for the respective cross section.
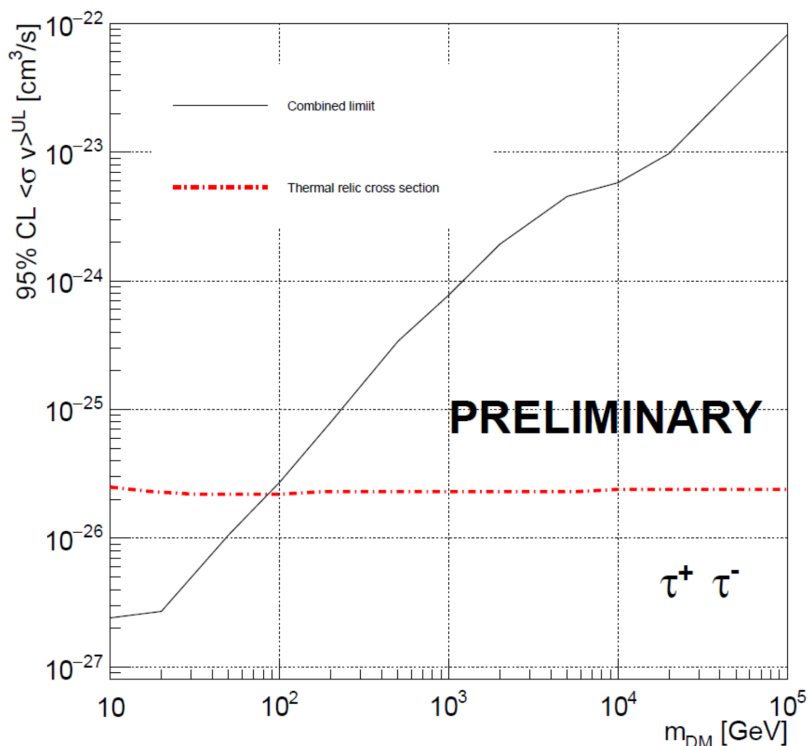

Figure 1.5: Upper limits on the DM annihilation cross section from the combination of data from observations of 20 dwarf galaxies by FERMI-LAT, HAWC, H.E.S.S., MAGIC and VERITAS, assuming 100% annihilation to $\tau^+\tau^-$ [75].

1.2.3.3 Direct Detection

In contrast to indirect detection, direct detection experiments are strictly earth-based detectors that aim to observe low-energy recoils of nuclei induced through elastic scattering directly with WIMPs, as they pass through the Earth. These measurements provide information about the interaction cross-section of DM with regular matter and set constraints on the parameter space of DM candidates. The typical kinetic energy of a

recoiling nucleus is a few keV. After an interaction between a DM particle and a nucleus in the sensitvity detector volume, the nucleus will emit energy in the form of scintillation light. The expected interaction rate is at most one event per day and per kilogram of detector material. It is crucial to maintain an extremely low background rate, and experiments typically operate deep underground where interference from cosmic rays is minimized. In WIMP nucleon scattering processes, the interaction requires the existence not only of the DM particle itself, but also another field or particle which mediates the interaction. It is useful to distinguish between the component of the interaction cross section that depends on the spin of the mediator particle, and the component which is independent of this spin. That is because different detection strategies can be more or less sensitive to the mediator spin, depending on whether the interaction proceeds through the scalar term or the axial term of the Lagrangian, i.e., whether the interaction is mediated through a scalar boson or a vector boson. The most prominent underground laboratories hosting direct detection experiments are the SNOLAB underground laboratory [76] at Sudbury and the Gran Sasso National Laboratory [77].

In Figure 1.6, the best current constraints on the DM-nucleon cross section from direct and indirect DM detection experiments are shown as a function of the DM mass for the DM-neutron cross section for spin-independent, and on the DM-proton cross section for spin-dependent interactions. The two most stringent limits are currently from the LUX-ZEPLIN (LZ), which uses a detector made of 10 tons of liquid xenon for direct detection of WIMPs (similar to the XENONNT experiment and the PANDAX-4T) and the PICO collaboration at SNOLAB [78].
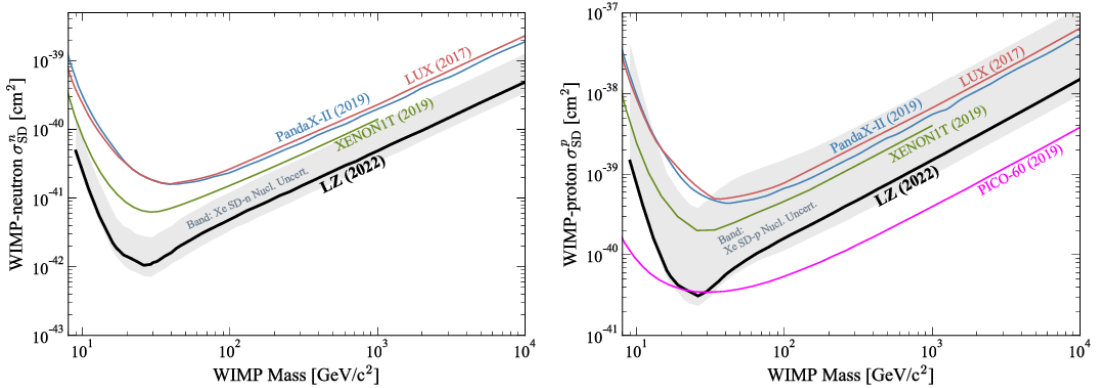

Figure 1.6: The best current limits for WIMP-neutron (left) and WIMP-proton (right) cross section as a function of WIMP mass from direct detection experiments in combination with indirect detection limits [78].

In summary, the information gained from direct and indirect detection has narrowed down the range of possible masses and interaction strengths for DM particles. This helps guide the design of particle collider experiments for detection of DM particles to focus on energy regimes where potential DM interactions might occur. In particle

collider experiments, DM particles are produced in the collisions of high energy particles and travel through the detector. Since potential DM particles should have negligible interactions with SM particles that make up baryonic-matter and detector material, additional dedicated reconstruction techniques are employed to yet identify the DM signals. The detection of DM in a collider search is the goal of the analysis presented in this thesis. The anlaysis and all methods used in this search are described in Chapter 3.

1.3   Supersymmetry and Long-lived Particles

Efforts to identify the fundamental particles comprising DM have led to a wide range of theories and hypotheses. Supersymmetry [11, 18, 79, 80] is a set of theories that address different limitations of the SM mentioned in Section 1.1.5. In simple terms, SUSY postulates a symmetry that establishes a connection between fermions and bosons, introducing a super partner for each SM particle called a sparticle. Sparticles have identical quantum numbers as their corresponding SM particles, except for the spin. This means that a supersymmetric transformation converts a bosonic state into a fermionic state, and vice versa. To distinguish the notation of sparticles from from SM particles, a tilde is typically written above the particle symbol, such as $\tilde{t}$ denoting the top squark, which is the super partner of the SM top quark t. No supersymmetric particles haven been observed so far. SUSY particles with the same mass as the SM particles are thus not consistent with experimental observations. The absence of observations within certain mass ranges defines the necessary mass gap between SM particles and sparticles. This implies that SUSY, if it is a symmetry that describes Nature at high energy scales, must be broken below the TeV scale.

In many SUSY models, the Lagrangian contains terms that explicitly violate baryon (B) and lepton (L) number conservation. These terms include bilinear terms that mix the higgs fields and trilinear terms involving the interactions of quarks, leptons, and their supersymmetric partners. These terms, if not controlled, can lead to rapid proton decay and other unwanted phenomena. Especially a rapid proton decay contradicts physical observations, including the stability of protons over experimental time scales, as supported by numerous experiments such as those conducted at the Super-Kamiokande detector [81]. Subsequently, in most well-motivated SUSY scenarios a discrete symmetry is introduced to address these problems. The introduction of a new symmetry gives rise to a new preserved quantity, which is the R-parity

$$P_R = (-1)^{3B+L+2s}. \tag{1.22}$$

While baryon number and lepton number are no longer conserved, R-parity, with s being the spin, is conserved. There are also R-parity violating SUSY models [82], however, they can be neglected for the context of the analysis presented in this thesis. All SM particles have an R-parity of +1 and all superpartners have R-parity of -1. With R-parity conservation, the Lagrangian allows only for the production or annihilation of an

even number of supersymmetric particles, thereby preventing a sparticle from decaying solely into SM particles. Since the proton is not a supersymmetric particle, it cannot decay directly into an odd number of SUSY particles while conserving R-parity. Thus, R-parity conservation helps prevent rapid proton decays in SUSY models. In addition, the conservation leads to the stability of the lightest SUSY particle, which serves as a DM candidate in those models. In the remainder of this section, the most well-motivated SUSY models that predict a viable DM candidate are discussed.

1.3.1 R-Parity Conserving MSSM

The MSSM [18] stands out as the SM extension with the least additional field content, featuring precisely one SUSY partner for each SM particle and four additional Higgs bosons, alongside with their supersymmetric partners. Table 1.2 shows the additional particles considered in the MSSM.

The MSSM offers a compelling DM candidate, making it attractive for theoretical interpretations. To explore how the lightest electroweakino serves as a suitable DM candidate within the MSSM, it is essential to delve into the role of the electroweakinos in this framework. Elektroweakinos are particles with masses on the order of the electroweak scale postulated in many SUSY models, particularly the MSSM. The mass eigenstates of electroweakinos result from the mixing of the partner particles of the Higgs bosons, higgsinos, and partners of the gauge bosons, gauginos. In the MSSM, two Higgs doublets are required, leading to a total of five higgs bosons. This is necessary to resolve a gauge anomaly caused by a single higgs doublet, and to accommodate the distinct Yukawa couplings of quarks to the higgs bosons in supersymmetry. In contrast to the SM, where both up-type and down-type quarks couple to the Higgs field, the MSSM separates their couplings, leading to the inclusion of an additional supersymmetric Higgs doublet.

In analogy to the mixing of the B field and the neutral W_3, as well as the W_1 and W_2, due to the SSB in the SM (cf. Section 1.1.2), the higgsino and electroweak gauginos mix. The superpositions of the neutral superpartners of the Higgs and electroweak gauge bosons are called neutralino. The neutralino mass matrix relates the gauge eigenstates (bino, wino, and two higgsinos) to the mass eigenstates ($\tilde{\chi}^0_{1,2,3,4}$) as follows:

$$M = \begin{bmatrix} M_1 & 0 & -m_Z \cdot c_W \cdot s_\beta & m_Z \cdot s_W \cdot s_\beta \\ 0 & M_2 & m_Z \cdot c_W \cdot c_\beta & -m_Z \cdot s_W \cdot c_\beta \\ -m_Z \cdot c_W \cdot s_\beta & m_Z \cdot c_W \cdot c_\beta & 0 & -\mu \\ m_Z \cdot s_W \cdot s_\beta & -m_Z \cdot s_W \cdot c_\beta & -\mu & 0 \end{bmatrix} \tag{1.23}$$

In the mass matrix, M_1, and M_2 are the soft SUSY-breaking bare masses of the bino and wino; parameter m_Z and s_W represent the mass of the Z boson and sine of the weak mixing angle; the parameter s_β and c_β represent the sine and cosine of the ratio of the vacuum expectation values from the neutral components of the two scalar Higgs

	Names	Spin	Charge [e]	P_R	Gauge Eigenstates	Mass Eigenstates
Sfermions	Sleptons I		-1 0		$\tilde{e}$ $\tilde{\nu}_e$	$\tilde{e}, \tilde{\mu}$ $\tilde{\nu}_e, \tilde{\nu}_\mu$
	Sleptons II		-1 0		$\tilde{\mu}$ $\tilde{\nu}_\mu$	
	Sleptons III		-1 0		$\tilde{\tau}$ $\tilde{\nu}_\tau$	$\tilde{\tau}_{1,2}$ $\tilde{\nu}_\tau$
	Squarks I	1	+ 2/3 -1/3	-1	$\tilde{u}$ $\tilde{d}$	$\tilde{u}, \tilde{d},$ $\tilde{c}, \tilde{s}$
	Squarks II		+2/3 - 1/3		$\tilde{c}$ $\tilde{s}$	
	Squarks III		+ 2/3 - 1/3		$\tilde{t},$ $\tilde{b}$	$\tilde{t}_{1,2}$ $\tilde{b}_{1,2}$
Gauginos	Higgsinos	1/2	$0, \pm 1$	-1	$\tilde{H}_u^0, \tilde{H}_d^0 \tilde{H}_u^+, \tilde{H}_d^-$	Charginos: $\tilde{\chi}_{1,2}^\pm,$ Neutralinos: $\tilde{\chi}_{1,2,3,4}^0$
	Winos		$0, \pm 1$		$\tilde{W}^0, \tilde{W}^\pm$	
	Binos		0		$\tilde{B}^0$	
	Gluinos		0		$\tilde{g}_{1,\dots 8}$	$\tilde{g}_{1,\dots 8}$
Bosons	Higgs bosons	0	0 / ± 1	+1	$H_u^0, H_d^0, H_u^+, H_d^-$	$h^0, H^0, A^0, H^\pm$

Table 1.2: Additional particle content of the Minimal Suspersymmetric Standard Model. In addition to one supersymmertric partner for each SM particle (cf. Table 1.1), four additional Higgs bosons are added, alongside with their supersymmetric partners, the higgsinos. In the general MSSM, also first and second generation sfermions have mass eigenstates that differ from the gauge eigenstates, but this distinction is neglected here. For reasons of presentation, the observed Higgs boson (h^0) is included in the list, even though it is inherently part of the SM (H in Table 1.1).

doublets. The ratio of two vacuum expectation values of the Higgs fields

$$\tan \beta = \frac{\langle H_u \rangle}{\langle H_d \rangle} \tag{1.24}$$

governs the behavior of the Higgs sector and its interactions with fermions in SUSY models. The parameter μ is the higgsino mass parameter. Thereof, all four neutralino states are Majorana fermions emerging from the diagonalization of the neutralino mass matrix. Each state is a superposition of the neutral electroweak gauginos and higgsinos.

The lightest neutralino, $\tilde{\chi}_1^0$, is assumed to be the lightest sparticle in the MSSM. The eigenvalues of the mixing matrix determine the masses of the neutralino eigenstates, and the degree of mixing determines various properties of the interactions, such as the branching fractions of the possible decay modes. Consequently, the $\tilde{\chi}_1^0$ is a linear combination of the gauge eigenstates

$$\tilde{\chi}_1^0 = N_{11}\tilde{B} + N_{22}\tilde{W} + N_{13}\tilde{H}_d^0 + N_{14}\tilde{H}_u^0, \tag{1.25}$$

where N is the unitary 4×4 matrix that diagonalizes the neutralino mass matrix in Equation 1.23. Similarly, charginos $\tilde{\chi}^\pm$ are Dirac mass eigenstates resulting from the mixing between charged higgsinos and winos. The relations between the coefficients N_{ij} yield the predominant nature of the neutralino, e.g., when

$$N_{11}^2 > \max\{N_{12}^2, N_{13}^2 + N_{14}^2\},$$

$\tilde{\chi}_1^0$ is called bino-like. The neutralino mass matrix and its elements depend on the specific framework or model of supersymmetry that is being considered. Different choices of model parameters lead to variations in the values of the mass parameters and mixing angles, leading to different neutralino phenomenology (cf. Section 1.3.1.2). In result, the LSP can be either mostly bino-, wino-, higgsino-like, or a mixture. These distinct natures lead to different signatures for neutralinos in collider searches, demanding unique search strategies for each type of DM candidate. These strategies will be explored on in the upcoming sections.

1.3.1.1   Naturalness in the MSSM

Among all, natural SUSY is especially well motivated, as natural refers to a mild level of fine-tuning in these scenarios and ensures that the new physics satisfactorily addresses the hierarchy problem (cf. Section 1.1.5). Natural SUSY provides an elegant solution to the hierarchy problem by introducing superpartners for each known particle. These sparticles, through their interactions with the Higgs boson, contribute to quantum loop corrections that partially cancel out the large quadratic divergences arising from Standard Model particles. These cancellation help stabilize the Higgs mass against quantum fluctuations, reducing the need for extreme fine-tuning.

Naturalness in SUSY models and the MSSM explicitly has various implications on the model parameters such as the dominant mixing parameters, which determine the mass differences among the gauginos. If SUSY were not broken, the quadratic divergences would cancel out exactly. However since SUSY must be broken, a soft breaking can be assumed, which implies that quadratic divergences are canceled out, leaving only logarithmic divergences to remain. This solves the hierarchy problem but simultaneously requires the breaking to occur at the weak scale, constraining the mass gap between the SM particle and sparticles to about 1 TeV [18]. As a consequence of electroweak symmetry breaking, the Higgsino mass parameter μ is directly connected to the mass of the Z boson m_Z at tree level via

$$\mu^2 = m_Z^2 \left(\frac{-1}{2} + \frac{m_{H_d}^2 - m_{H_u}^2 \tan^2\beta}{\tan^2\beta} \right).$$ (1.26)

Resulting from Equation 1.3.1.1, to fulfill naturalness, higgsinos should be rather light as the higgsino mass can not be much larger than m_Z. Equation 1.3.1.1 can be expressed using the electroweak fine-tuning parameter ΔEW. It holds the maximum value of any term in an expanded version of that equation with higher orders. This yields

$$|\mu^2| < \Delta EW \frac{m_Z^2}{2}.$$ (1.27)

In order to minimize the level of fine-tuning to less than 1 % ($\Delta EW < 100$), it is therefore necessary to limit the mass of higgsinos to approximately 700 GeV. Meanwhile, the bino and wino mass parameters can be very large.

Conclusively, the MSSM addresses several of the shortcomings of the SM, making it an especially well-motivated BSM theory. It can provide a DM (WIMP) candidate since the LSP cannot decay any further if R-parity conservation is required. If moreover the LSP is only weakly interacting, it can serve as a good candidate for (some of) the invisible matter in the universe. In addition, natural SUSY models provide a solution to the hierarchy problem. The search for electroweakinos as manifestations of the MSSM is thus theoretically compelling and well-grounded.

1.3.1.2 Electroweakino Mass Spectrum

Following the aspiration to obtain low fine-tuning in physical models, SUSY models with minimal field content that fulfill the previously discussed fine-tuning criterion are most well motivated. The two models to meet these expectations, which are chosen for the interpretation of the analysis presented in this thesis, are the compressed higgsino model and the bino-wino-coannihilation model.

Particle lifetimes

Both of these models give rise to long-lived particles, LLPs. In this thesis, long-lived refers to particles with lifetimes that allow their flight distance to be macroscopic, in other words that the particles live long enough to be measurable in the detector. Which BSM model parameters lead to longer lifetimes for predicted particles can be understood, by understanding what determines the mean lifetime of a particle in a decay. The probability of a particle decaying after time t is described by Poisson statistics, and is given by:

$$P(t; \tau) = 1 - e^{-\frac{t}{\gamma \tau}}, \tag{1.28}$$

where the Lorentz boost of the particle is given by γ and its proper lifetime by τ. The lifetime of a particle τ is the inverse of the decay width

$$\tau = \frac{1}{\Gamma}. \tag{1.29}$$

Following Fermi's golden rule [83], the differential decay width for a particle of a mass M and four-momentum P decaying into n particles with momenta p_i is given as:

$$d\Gamma_n = \frac{1}{2M} \int |\mathcal{M}|^2 S d\phi(P, p_1, ... p_n). \tag{1.30}$$

In Equation 1.30, $|\mathcal{M}|^2$ is the squared matrix element, which represents the amplitude for the decay process and depends on the specific interaction involved; S is the phase space factor, and $d\phi$ represents the differential phase space. The mean lifetime of a particle in a decay is thus determined by the amplitude of the process and the phase space. The amplitude or matrix element of the decay depends on the coupling of the particles involved. The phase space is a kinematic factor or combinatorial factor to account for indistinguishable final states. The available phase space is directly related to the mass differences of the particles.

In general, approximate symmetries, i.e., conservation laws, can stabilize LLPs, as well as small couplings between a LLP and lighter states, and suppression of the available phase space for decay. For particles moving close to the speed of light, this can lead to macroscopic, detectable displacements between the production and decay points of a LLP of $c\tau \gtrsim O(10)\mu$m.

In the case of small mass differences between the mother particle and one daughter, i.e., mass degeneracy, the decay may be highly off-shell, meaning that the mediating particle of the decay is virtual. The virtual gauge boson of such a process does not have the exact mass of an on-shell boson, but its energy and momentum are determined by the conservation laws of the interaction. Such a decay is phase-space suppressed, which, as indicated by Equation 1.30, results in an extended lifetime of the mother particle.

Compressed Higgsino Model

The arguments of naturalness (cf. Section 1.3.1.1) support a configuration where the lightest three electroweakinos are higgsino-like with similar masses, as they are barely influenced by M_1 and M_2. Pure higgsino-like LSPs tend to have a relatively large mass, and if they were the dominant form of DM, their predicted relic abundance would exceed the observed amount of DM in the universe [84]. By introducing a small amount of mixing with other neutralinos (e.g., binos or winos), the overall mass of the resulting mixed neutralino can decrease, aligning better with the observed DM density. Therefore, a nearly-pure higgsino-like LSP is choosen in the compressed higgsino model which allows for more diverse and realistic scenarios that align with both observed DM levels and experimental constraints.

The mixture of the LSP also affects the interaction cross sections between the neutralino and other particles, influencing their detectability in experiments. In Figure 1.7 on the left, the neutralino mass difference $\Delta m_0 = m_{\tilde{\chi}_0^2} - m_{\tilde{\chi}_0^1} = m_{\tilde{\chi}_0^2} - m_{\mathrm{LSP}}$ for the nearly-pure higgsino-like LSP in the compresses higgsino model is given, as a function of the wino mass $|M_2|$. For readability, the mass difference of the neutralinos is denoted by Δm_0 in this thesis, while it is given by Δm in the original reference [84]. Both, Δm_0 and $|M_2|$ are essential parameter for the search presented in this thesis. The further model parameter are chosen as: $\tan\beta = 2$, $\mu = 500$ GeV; bino mass $M_1 = M_2$; SUSY breaking scale $\tilde{m} = |M_2|$, as well as $\phi_2 = \arg(M_2) = 0$ and $\phi_2 = \pi/2$, respectively. Hereby, ϕ_2 or $arg(M_2)$ represent the complex phase component of the M_2 parameter, which determines the pattern of electroweak symmetry breaking, the mixing of neutralinos and charginos, as well as the flavor physics within the MSSM. As can be seen in Figure 1.7, for $|M_2| \approx O(1)$ TeV, the neutralino mass difference can be as large as $O(10)$ GeV, decreasing for heavier gaugino masses. The proper lifetime increases with decreasing mass differences, as can be seen in Figure 1.7, left. For mass differences in the range of 200 MeV $\leq \Delta m_0 \leq 1.2$ GeV, the proper lifetime results in mean displacements of the decaying particles of about 100 μm to 1 cm. Such displacements are in principle detectable at the CMS experiments. In conclusion, the smallness of the mass difference, which makes it especially hard to discover a higgsino-like LSP at a hadron collider, can simultaneously yield an additional powerful handle through the finite lifetime of the decaying electroweakino, which can become visible at the scale of detectors and in searches for long-lived particles.

Bino-Wino-Coannihilation model

The second scenario for elektroweakino masses that is especially interesting for collider experiments, well motivated in theory, and targeted by the search presented in this thesis, is the bino-wino-coannihilation model. Provided that $\tilde{\chi}_1^0$ is bino or wino-like, it can coannihilate with other light sparticles. For this thesis, a bino-like LSP and a wino like NLSP are considered. Due to the small couplings of Higgs/Z boson with the bino-
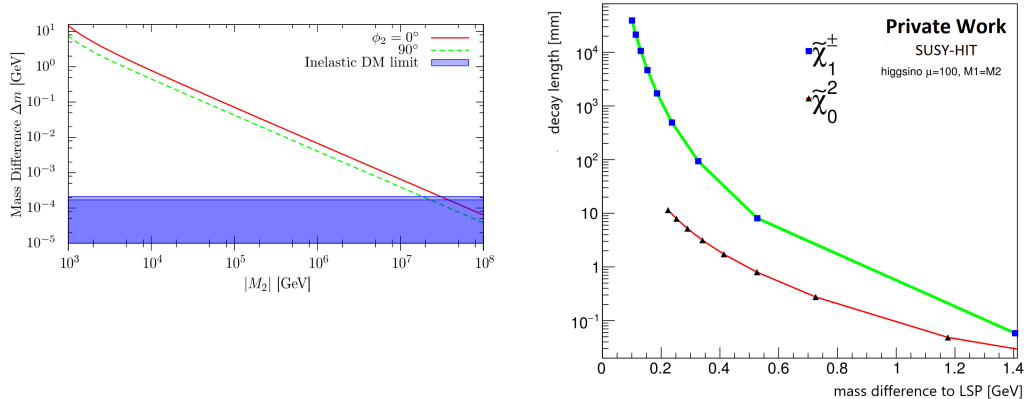
Figure 1.7: Left: Neutralino mass difference as a functions of the wino mass parameter M_2 in the nearly-pure higgsino model in combination with the weakest (strongest) bounds given from three different DM direct detection experiments in the dark (light) shaded region [84]. Right: Relation between the proper lifetime of the chargino or neutralino, respectively, and the mass difference to the LSP ($\tilde{\chi}_1^0$) in the pure-higgsino model.

like $\tilde{\chi}_1^0$, the annihilation rate of $\tilde{\chi}_1^0$ into the SM particles is highly suppressed. However, the presence of the wino-like NLSP with a mass not high above the bino-like LSP boosts the annihilation. This process is called coannihilation.

1.3.1.3 Scan of the pMSSM Parameter Space

A detailed study of pMSSM model points [85] provides further motivation for the search for electroweakinos. The phenomenological Minimal Supersymmetric Standard Model (pMSSM) is a slightly constrained version of the MSSM that remains consistent with current observations while significantly reducing the number of unconstrained free parameters from 120 to just 19. It imposes several key assumptions, which are

- the absence of new sources of CP violation,

- the absence of flavor-changing neutral currents,

- the universality of the first and second fermion generations,

- the limitation of trilinear couplings to the third fermion generation,

- the lightest neutralino being the LSP.

The term CP violation refers to the violation of charge conjugation parity (CP) symmetry that was discovered in the quark sector in 1964 in the decays of neutral kaons [86]. Flavor-

changing neutral currents are interactions that change the flavor of a fermion without altering its electric charge, which are forbidden at the tree level in the SM but can occur at higher orders through loop diagrams [87].

Figure 1.8 shows the distribution of model points in the pMSSM as a function of the proper decay length of the second lightest neutralino, before taking into account constraints derived from LHC results (left). In the Figure, three possible flavors of a neu-
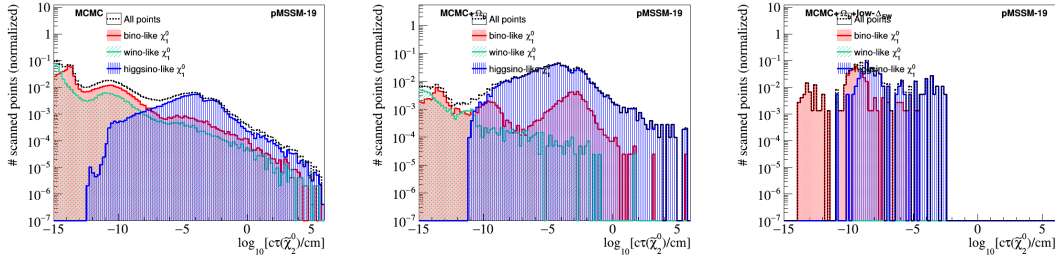

Figure 1.8: Fraction of pMSSM model points with neutralino LSP ($\tilde{\chi}_1^0$) as a function of the logarithm of the proper decay length ($c\tau$) of the neutralino NLSP ($\tilde{\chi}_2^0$) from a scan of pMSSM model points. The distributions are given before any LHC constraints (left), when the LSP accounts for $100\pm10\%$ of the observed relic density (middle), and requiring additionally less than 2% finetuning ($\Delta EW < 200$) (right). Three types of LSP are considered: a bino-like LSP (red filled area), a wino-like LSP (green filled area) and a higgsino-like LSP (blue filled area). The sum of all three is given as the black dashed line [85].

tralino LSP are allowed, and their individual contributions are denoted by the color-filled histograms. The masses M_1 and M_2, as well as μ are randomly scanned between 0 and 4 TeV. Notably, a significant fraction of model points with bino-like, wino-like, and higgsino-like DM exhibit long-lived $\tilde{\chi}_2^0$ with decay lengths surpassing the minimal vertex resolution of the CMS experiment (cf. Figure 1.8, left), which potentially can be detected using vertex reconstruction in the CMS tracking detector. In a significant subset of points, the LSP can account for $100\pm10\%$ of the observed relic density from LHC result (cf. Figure 1.8, middle). However, requiring the LSP to account for nearly all DM observed in the universe is in tension with requirements of naturalness (cf. Figure 1.8, right), as an LSP mass of about 1 TeV is favored to explain the observed DM density, while the naturalness favors lighter higgsinos with masses of $O(100)$ GeV (cf. Section 1.3.1.1).

Requiring a bino-like LSP as in the bino-wino-coannihilation model features especially long-lived neutralinos while being, natural and able to produce the correct DM relict density. This becomes visible from Figure 1.9, where the left figure shows the number of pMSSM model points with a bino-like LSP and a wino-like NLSP for neutralino mass differences between 1 and 10 GeV as a function of the mean proper lifetime of the $\tilde{\chi}_2^0$. As can be seen, in the region of small Δm_0, the corresponding proper lifetime in many
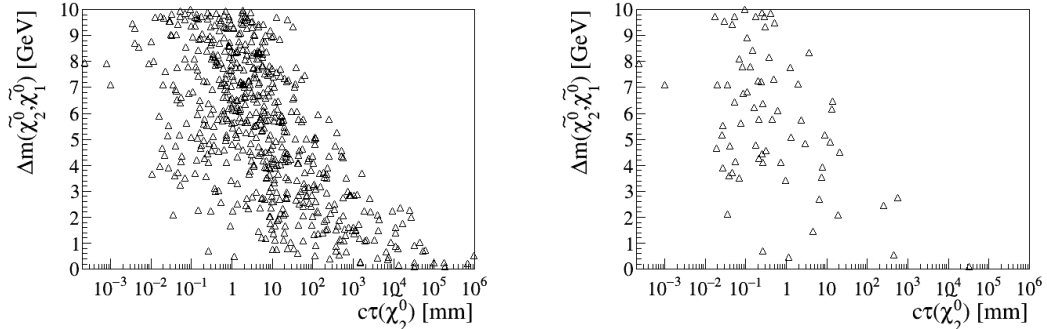
Figure 1.9: Left: pMSSM model points in the plane of the mass difference of the lightest neutralinos and the proper lifetime ($c\tau$) of the $\tilde{\chi}_2^0$ in the bino-wino-coannihilation model from a scan of pMSSM model points. Right: Subset of pMSSM model points consistent within 10% with the observed DM abundance in the universe from [2] in a scan of pMSSM model points [85].

model points can range up to a few centimeters or even meters.

In this model, the coannihilation with the wino-like electroweakinos is essential in yielding the correct DM relic density. The subset of pMSSM model points with a bino-wino like LSP that are consistent within 10% with the observed DM abundance in the universe from [2] is given in the right plot of Figure 1.9.

In summary, two LSP scenarios are targeted in this thesis. Both lead to the production of electroweakinos, as well as an electroweakino mass spectrum that could give rise to soft particles in the final state and a long-lived $\tilde{\chi}_2^0$. The decay of the $\tilde{\chi}_2^0$ to the LSP could be identified by the presence of a displaced secondary decay vertex at the LHC. Generally, different analysis strategies are needed, for different expected mean displacements in the SUSY models, as will be further layed-out in the following sections (cf. Section 1.3.2).

1.3.2 Long-lived Particles

The study of long-lived particles has a long history in collider physics, where long-lived SM particles such as pions and kaons serve as essential probes to investigate the subatomic field. Neutral kaons play a special role among the low-mass SM neutral hadrons. Although the K^0 and its antiparticle $\bar{K}^0$ are usually produced via the strong force, they decay weakly. The K^0 and the $\bar{K}^0$ carry different strangeness and oscillate (turn from one into another through the weak interactions). Thus, they can be thought of as superpositions of two weak eigenstates which have different lifetimes. The longer-lived neutral kaon is called the K_L^0 and has a lifetime of a 5.12×10^{-8} s. It decays

primarily into three pions. The shorter lived neutral kaon is called K_s^0, has a lifetime of 8.95×10^{-11} s, and decays primarily into two pions. The lifetime of the K_s^0 is similar to the lifetime of the $\tilde{\chi}_2^0$ in the targets signal models. In addition, with a mass of 497.61 GeV, the K^0 mass is of similar order of magnitude as the typical mass difference in these models. Therefore K_s^0 are of great use for the development of reconstruction methods for long-lived $\tilde{\chi}_2^0$. The study of K_s^0 is described in Section 2.3.2.1.

Moreover, exotic long-lived particles have long been a subject of fascination and investigation in particle physics, manifesting in various extensions of the SM, with particular relevance in the MSSM. In the further course of this section, we will contextualize this thesis within the field of LLP searches, where diverse analysis strategies are employed due to the unique characteristics of various types of LLPs.

1.3.2.1 Experimental Signatures in Collider Experiments

Experimental signatures of exotic LLPs in collider experiments are diverse and often different from signals of SM processes. LLP signatures can include tracks with unusual ionization and propagation properties; small, localized deposits of energy inside of detector calorimeters without associated tracks; stopped particles that decay out of time with collisions; displaced secondary vertices (SV) in the inner detector or muon spectrometer; and disappearing, appearing, and kinked tracks, to name a few. Figure 1.10 provides a schematic representation of a subset of the various LLP signatures of BSM searches conducted at the LHC.

Standard reconstruction algorithms may reject events or objects that involve LLPs due to their unconventional characteristics. Their unique signatures can sometimes resemble detector noise, pile-up events (simultaneous collisions), or incorrectly reconstructed objects. As a result, specialized search strategies are necessary to identify and study LLP signals. In the following, a brief description of the distinct signal characteristics for the different types of LLPs as shown in Figure 1.10 is given.

Disappearing or kinked tracks arise in scenarios involving LLPs that have a significant decay length, i.e., models with a small mass differences between a charged massive mother particle and one of its invisible neutral daughter particles, or a feeble coupling associated with the decay. These LLPs can travel a certain distance within the detector before decaying, resulting in tracks that terminate prematurely. This behavior is different from the typical tracks produced by promptly produced particles, which extend throughout the entire detector. While disappearing tracks come with a non-reconstructed SM daughter particle, kinked tracks are a slightly modified signature, for which the SM particle is reconstructed, usually as a low-momentum curled track.

Photons coming from LLP decays do not resemble standard photons as they cannot be traced back to the PV, but are displaced, **(non-pointing) photons**. In addition, photons radiated by off a long-lived neutral particle can arrive at the ECAL at a time slightly later than expected because the LLP moves slower than the speed of light;
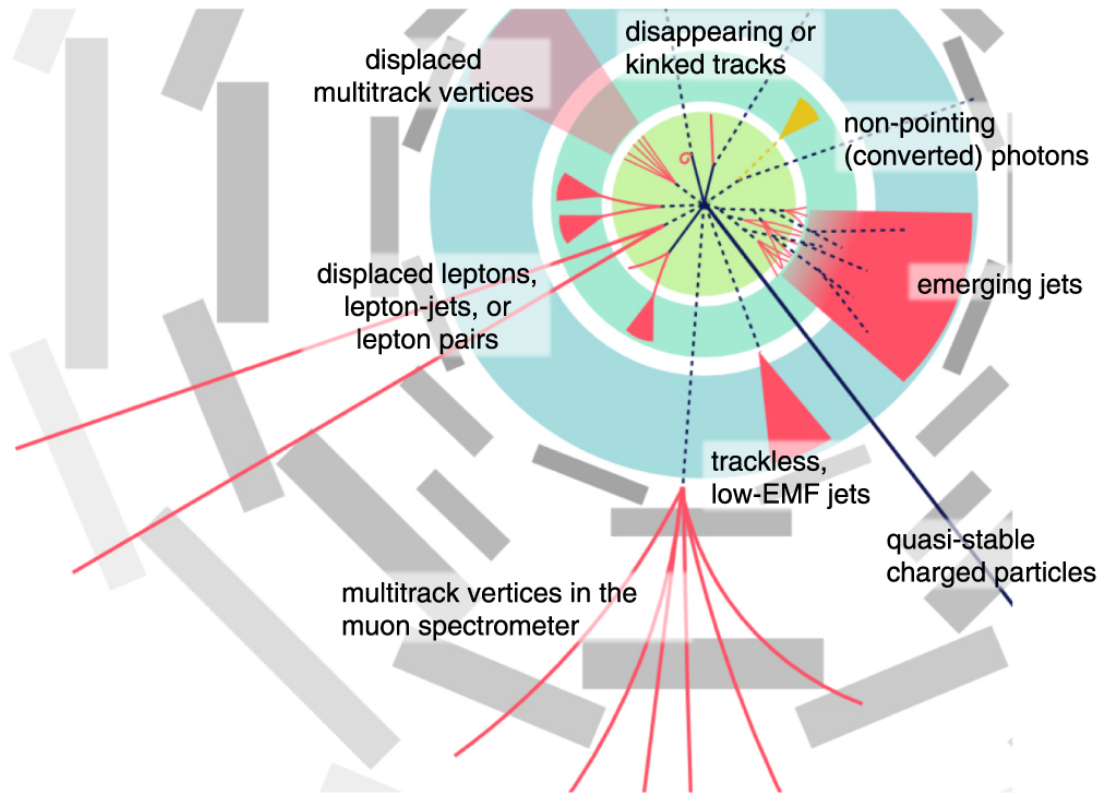
Figure 1.10: Schematic view of the possible experimental signatures that can result from BSM LLPs in collider searches, including the signature of displaced leptons [88].

these are referred to as delayed photons. Both, delayed and non-pointing photons can alternatively be detected via their conversion to e^+e^- pairs.

Emerging jets and trackless low electromagnetic-fraction (EMF) jets arise from dark sector radiation (dark showers) and as the detector signature of strongly interacting massive particles (SIMPs). SIMPs are assumed to interact strongly with baryons and thus leave little to no signal in the tracker and the ECAL, and large energy deposits in the HCAL.

Stable charged particles are quasi-stable charged LLPs, meaning they can traverse a substantial fraction of the detector or even exit it before decaying. In particular heavy stable charged particles (HSCPs) are slow-moving particles, and thus are expected to have a higher rate of energy loss via ionization (dE/dx) and a longer time-of-flight.

Displaced multitrack vertices can emerge in the tracking detector or muon spectrometer of a typical multiple purpose detector like the CMS or ATLAS detector. A long-lived neutralino or gluino decaying into a quark and a squark can create the signature of displaced vertices, where the long-lived particle itself remains invisible. The separation in space between the two secondary vertices can be used to distinguish be-

tween signal and backgrounds arising from SM displaced vertices. Signal events typically have two well-separated displaced secondary vertices from two LLPs emitted approximately back-to-back, and standard model background events are dominated by at most only one displaced secondary vertex.

The **displaced lepton** and **displaced dilepton** signatures target a charged or neutral long-lived particle decaying into one or two leptons, and an additional particle. The search for the decay of a neutral LLP to a WIMP or DM candidate using displaced leptons is the focus of this work and discussed in more detail in Chapter 3. The requirement of leptons in the signature of the LLP decay makes those distinguishable from many SM LLPs.

While the number of searches specifically targeting prompt decays of new particles is substantial, there have been fewer dedicated searches for exotic LLPs conducted at the LHC. For more detailed information on these searches, Section 3.2 can be referred.

2 Experimental Setup and Event Reconstruction

This thesis relies on simulation data and proton-proton collision data recorded in 2016 by the **C**ompact **M**uon **S**olenoid (CMS) experiment at the **L**arge **H**adron **C**ollider (LHC). In this chapter, introductory information on the LHC are given, followed by a description of the CMS experiment, including the relevant event and particle reconstruction processes for measured and simulated data.

2.1 Large Hadron Collider

The LHC is a particle collider situated near Geneva, Switzerland, at the European Organisation for Nuclear Research, CERN. It operates within a circular tunnel with a circumference of 26.7 kilometers. The LHC accelerates hadrons, such as protons, in two counter-rotating beams and causes them to collide at four intersection points. It is primarily designed for proton-proton collisions, achieving a maximum center-of-mass energy of 14 TeV, as well as heavy-ion (Pb-Pb) and xenon-xenon collisions [89].

The LHC is the final stage in a complex series of particle accelerators that accelerate particles and supply beams to various smaller experiments. For proton beams, the pre-accelerator chain brings the energy up to 450 GeV before the particles enter the LHC. Figure 2.1 illustrates location and overall layout of the LHC, including the Super Proton Synchrotron (SPS) as the last pre-accelerator in the chain, and the most prominent LHC experiments, such as the CMS experiment.

The LHC takes advantage of the pre-existing tunnel that was constructed for the former LEP collider. This tunnel is approximately 100 meters below the surface and has an inner diameter of 3.7 meters.

The LHC itself consists of two metal pipes that serve as vacuum chambers. Within these chambers, particles are accelerated using electric fields. This acceleration is made possible by Radio-Frequency (RF) cavities, which provide the necessary electric fields to accelerate the particles during each pass. One of the advantages of a circular collider like the LHC is that particles can be continuously accelerated with each revolution until the nominal energy has been reached. However, in order to keep the particles following a
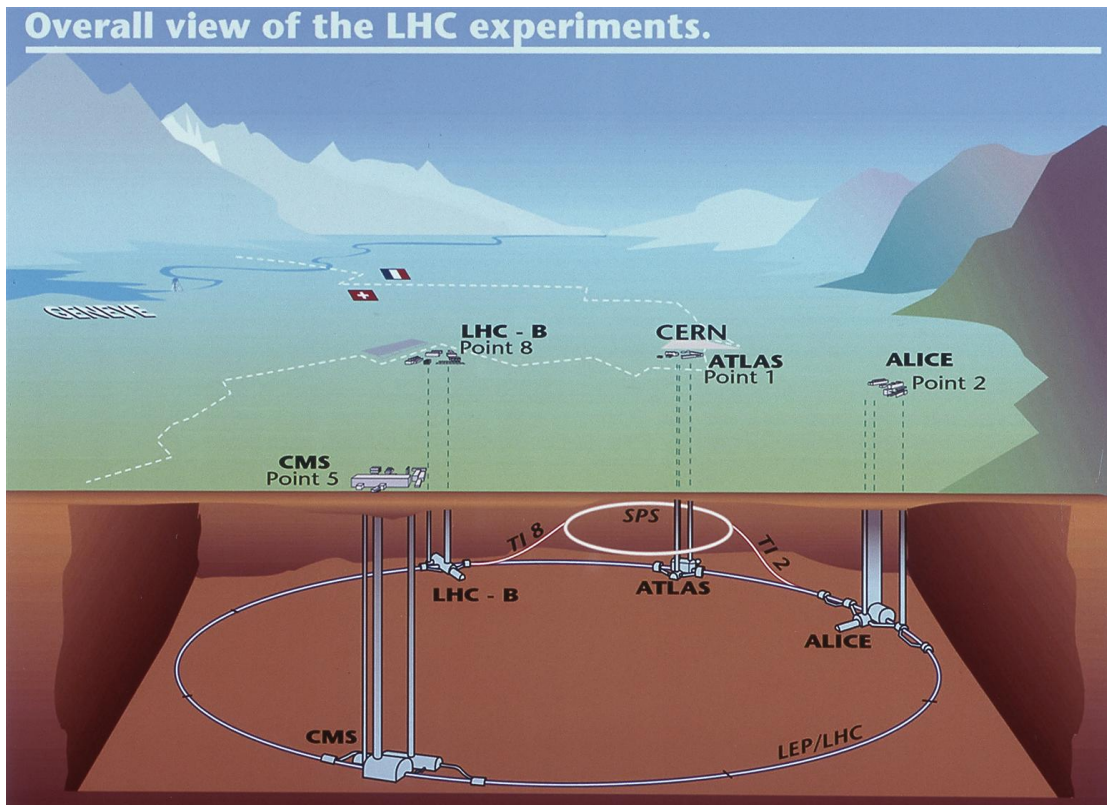
Figure 2.1: Sketch of the Large Hadron Collider with the main experiments ATLAS, AL-ICE, CMS and LHCb. Above ground, the positions of the experimental halls are shown in direct proximity to the French-Swiss boarder (white dashed line). Below ground, the experimental caverns which shelter the experiments and the supply shafts are drawn, along with the LHC and SPS storage and acceletor rings [90].

circular path, dipole magnets are employed as bending magnets. These magnets generate magnetic fields that bend the trajectory of the particles, allowing them to travel along the circular path. The strength of these bending magnets increases as the velocity of the particles increases. The dipole magnets are designed for a nominal magnetic field of up to 8.33 T for beam energies of up to 7 TeV per beam. In addition, quadrupole and sextupole magnets are used to guide, focus, and collimate the particles.

At four intersection points where the two beams are brought to cross, the experiments ALICE, ATLAS, CMS and LHCb are accommodated (cf. Fig. 2.1). Where ATLAS and CMS are so-called general purpose experiments, LHCb and ALICE are among many other things designed for measurements on CP violation and heavy-ion collisions, respectively.

During two scheduled shut-downs the LHC was upgraded from a beam energy of 3.5 TeV to 6.8 TeV per beam (13.6 TeV in collision). The first data-taking period from 2009 to

2013 is referred to as Run 1. This was followed by a long shutdown and a second major data-taking period from 2015 to 2018, Run 2, with energies of 6.5 TeV per beam. Since only the fraction of Run 2 data collected in 2016 is used for this thesis, all further machine values cited refer to the set up for Run 2 and in 2016, if not stated otherwise. Currently, Run 3 is ongoing. This latest data-taking period started in November 2021 after more than three years of upgrade and maintenance work and is planned for close to a four-year duration in total.

2.1.1 Luminosity

At collider experiments, the occurrence probability of a specific process, relies on the overall number of collisions taking place in the collider. The number of such events per second is given by:

$$N = L\,\sigma \quad , \tag{2.1}$$

where σ is the cross section of the specific process, known as an event, while L is the integrated luminosity of the machine L. The potential rate at which collisions can occur per second is given by the instantaneous luminosity $\mathcal{L} = dL/dt$, while the integrated luminosity serves as a measure of the total number of collisions produced over a specific time period. The instantaneous luminosity $\mathcal{L} = \frac{1}{\sigma}\frac{dN}{dt}$ is defined by

$$\mathcal{L} = \frac{N_1 N_2 f}{4\pi\sigma_x\sigma_y}F. \tag{2.2}$$

In Equation 2.2, $N_{1,2}$ is the number of particles per bunch (1.15×10^{11} for protons) and f the revolution frequency (11.25 kHz). The colliding beams are separated into bunches with each beam containing a maximum of 2808 bunches (as designed), colliding every 25 ns. Moreover, the spread in the transverse plane of the bunches is $\sigma_{x,y}$, and the crossing angle of the two bunches at the interaction point specify the beam profile F. The LHC design luminosity for pp collision of 10^{34} cm^{-2}s^{-1} leads to about 1 billion proton-proton interactions per second and a collision frequency of 40 MHz [89].

The integrated luminosity delivered by the LHC in 2016 was 41.58 fb^{-1}, whereof 38.25 fb^{-1} were recorded by CMS [91]. This is determined for the CMS experiment using van-der-Meer scans [92], where the transverse separation of the beams ($\sim F$) is varied over time. The area of the overlapping beams $4\pi\sigma_x\sigma_y$ is determined, along with a rate of a physical observable such as the number of charged particles in the tracking detector volume. As N_1, N_2 and f are known, the instantaneous luminosity can be determined from Equation 2.2.

2.2 Compact Muon Solenoid Detector

The CMS experiment is situated at the interaction point of LHC octant 5, beneath the French village of Cessy, approximately 100 meters underground. It has been specifically designed to investigate a wide range of physical phenomena both within and beyond the SM. It is a general-purpose detector for proton-proton, heavy-ion, and xenon-xenon collisions. The cylindrical CMS detector measures around 22 meters in length, has a diameter of 15 meters, and weighs 12,500 tons. The CMS detector is named after the high-field superconducting solenoid magnet of $B = 3.8$ T. Other main constituents of the CMS detector are a silicon-based tracking system, a crystal-based electromagnetic calorimeter, a hadronic calorimeter with scintillation detectors, and the muon chambers. The inner detector components are surrounded by the superconducting solenoid, while the outer region contains the iron return yoke interspersed with muon systems.

Figure 2.2 provides a transverse cross-sectional view of the general layout of the detector. Charged particles, such as electrons and charged hadrons, leave bent tracks within
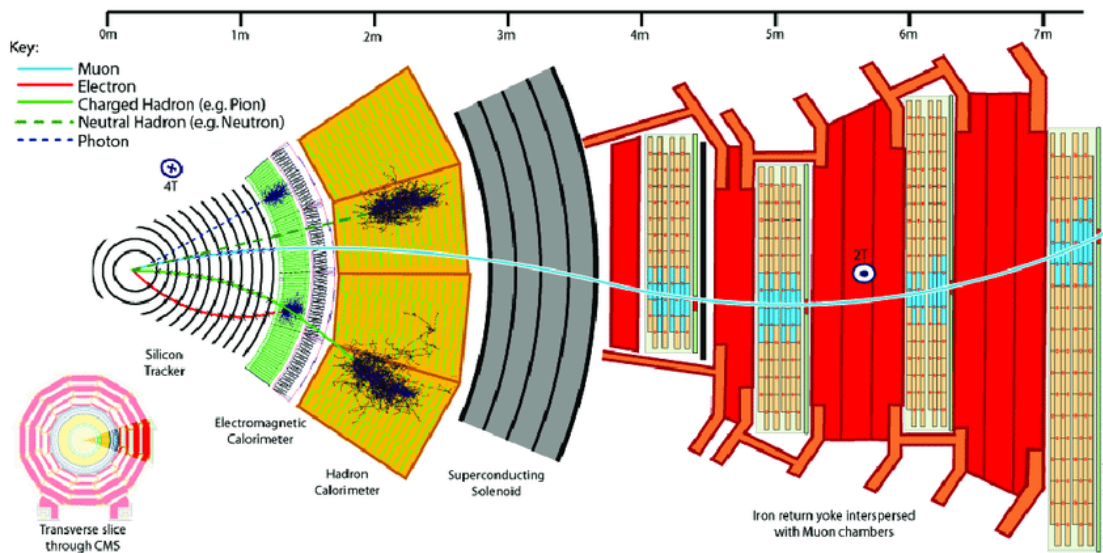
Figure 2.2: A transverse slice through one segment of the CMS barrel detector indicating the responses of the various detecting systems to different types of particles. Exemplary particle tracks are shown as colored lines, representing SM particles such as charged leptons and charged hadrons, neutral hadrons, and a photon [93].

the silicon tracker, with their energies deposited in the electromagnetic and hadron calorimeters, respectively. On the other hand, neutral particles like photons primarily deposit energy in the respective calorimeters, without leaving detectable tracks in the silicon tracker. Muons, which are minimum-ionizing particles (MIPs), can traverse the electromagnetic and hadron calorimeters and reach the muon chambers located outside, provided they possess sufficient energy.

The most relevant subsystems for the search described in this thesis will briefly be introduced in the following sections. For a more comprehensive understanding of the CMS detector, further detail can be found in references [89, 94].

2.2.1 Coordinate Conventions

The CMS experiment employs a coordinate system centered near the point of interaction. This system follows a right-handed convention, where the x-axis points toward the center of the collider, the y-axis points upwards, and the z-axis aligns parallel to the beam line in a counter-clockwise direction. In this coordinate system, the azimuthal angle ϕ is measured in the x-y plane from the x-axis, while the polar angle θ is measured from the z-axis. Figure 2.2.1 illustrates these conventions.
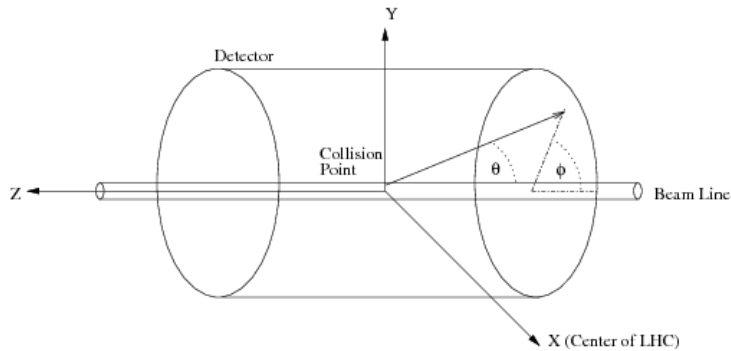
Figure 2.3: Conventional coordinates of the CMS detector. A right-handed cylindrical coordinate system is used, defining the angle with the beam axis (z-axis) θ, and the angle with the x-axis pointing to the centre ϕ [95].

The longitudinal coordinate is typically specified by the pseudorapidity:

$$\eta = -\ln\left[\tan\left(\frac{\theta}{2}\right)\right]. \tag{2.3}$$

The use of pseudorapidity is advantageous since differences in η are preserved under Lorentz transformations along the z-direction for massless particles. It is also an approximation of the rapidity for small masses. With the use of the pseudorapidity the barrel region ($|\eta| < 1.2$) and the endcap region ($1.2 < |\eta| < 2.4$) of the detector are defined.

As a measure of angular separation, the angular distance ΔR between two particles in the η-ϕ plane is used, defined as:

$$\Delta R = \sqrt{(\Delta\phi)^2 + (\Delta\eta)^2}. \tag{2.4}$$

46

2.2.2 Tracking Detector

The inner tracking system (tracker) is responsible for reconstructing the trajectories of charged particles, providing momentum information for the standard reconstruction and the high-level trigger system, measuring the ionization loss of charged particles, and identifying primary and secondary vertices.

Located in the innermost part of the CMS detector, the tracker has a cylindrical shape with a length of 5.8 m and a diameter of 2.6 m at its center. The tracker usually operates within a magnetic field of 3.8 T generated by the CMS solenoid. The tracker comprises a large silicon strip tracker with a small silicon pixel tracker inside it. The total acceptance of the tracker covers up to $|\eta| < 2.7$.

Both sub-detectors of the CMS tracker are made of silicon semiconductors. When charged particles pass through the silicon material, they create free electron-hole pairs, which drift in the electric field between oppositely charged electrodes, generating an electric signal. The magnitude of the resulting electric current is proportional to the energy lost by the particle as it traverses the tracker. Due to the small band gap of silicon, even a thin silicon layer can generate a strong signal, and particles with low ionization energies can be detected efficiently.

Silicon Pixel Detector
The silicon pixel detector is the closest detector to the beam pipe, with cylindrical layers roughly at 4 cm, 7 cm, and 10 cm and disks at either end, and so will be vital in reconstructing the tracks of short-lived particles. Each pixel module in the tracker is contains 16 readout chips (ROCs). These ROCs are bump-bonded to a pixel system consisting of a matrix of 52×80 pixels. The size of each pixel is 100 μm $\times$ 150 μm, with a sensitive volume thickness of 285 μm. The high pixel count and small size contribute to excellent spatial resolution of $10 - 20$ μm in $r - \phi$ and 40 μm in z-direction [89, 96]. The silicon pixel detector was replaced between data-taking in 2016 and 2017 with a more advanced detector featuring four different cylindrical layers in the barrel region (BPIX) and three (former two) discs in the outer endcap regions (FPIX). Additionally, the innermost pixel barrel layer was installed closer to the beam pipe, resulting in improved vertex resolution [97]. The purpose of the upgrade was to prepare for high-luminosity data taking in the following runs and to mitigate radiation damage. In this context, the detector conditions before the upgrade, which are used for data analyzed in this thesis, are referred to as Phase 0 while after the upgrade are referred to as Phase 1.

Silicon Strip Tracker
The silicon strip tracker surrounds the pixel detector completely and extends up to a radius of 1.1 m. It is divided into different subsystems. The barrel region consists of the Tracker Inner Barrel (TIB) and the Tracker Outer Barrel (TOB). The endcaps are composed of nine Tracker Endcap (TEC) disks on each side of the tracker, covering the region with 120 cm $< |z| < 280$ cm. Additionally, there are three tracker inner disks (TID) that bridge the gap between the TIB and TEC.

A sketch of the CMS tracker in the $r - z$ plane with the Phase-0 layout is shown in Figure 2.4.
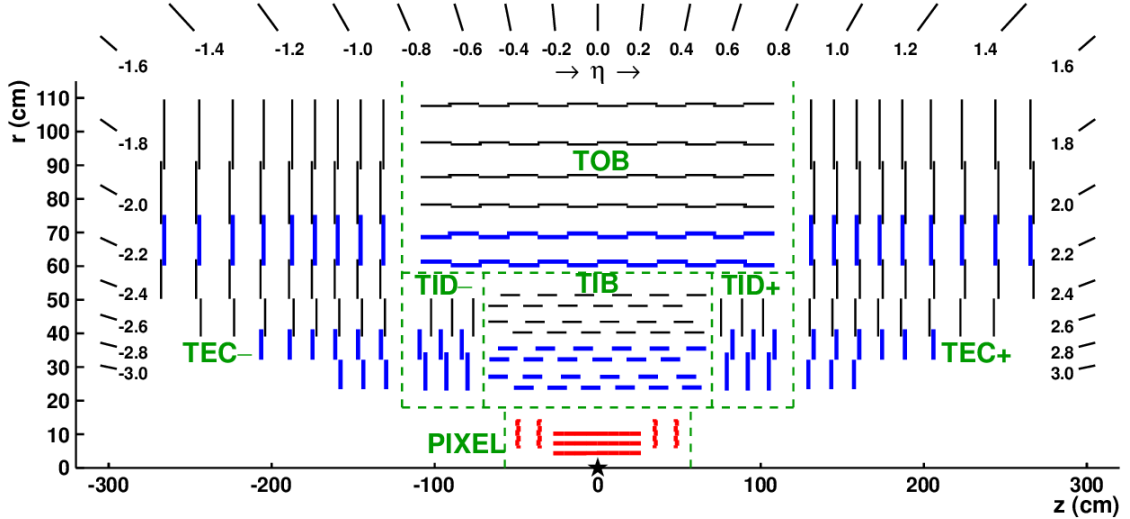

Figure 2.4: Schematic cross section of the CMS Phase-0 tracker in the $r - z$ plane. Shown are the silicon pixel detector (PIXEL) as well as different sub-systems of the silicon strip detector: Tracker Inner Barrel (TIB), Tracker Inner Disk (TID), Tracker Outer Barrel (TOB), and Tracker Endcap (TEC). Strip tracker modules that provide 2D-spatial information are shown by thin, black lines, while stereo-modules providing 3D-spatial information are shown by thick, blue lines [98].

2.2.3 Electromagnetic Calorimeter

The electromagnetic calorimeter (ECAL) is designed to detect and estimate the energy of particles that interact predominantly through the electromagnetic force, such as electrons and photons, which interact with matter primarily via bremsstrahlung and through pair production, respectively.

The ECAL is composed of 61,200 lead tungstate ($PbWO_4$) scintillating crystals in the central region, along with 7,324 crystals in each of the endcaps. The depth of the crystals, ranging between 24.5 and 25.7 radiation lengths (X_0), enables them to absorb a significant portion of the energy from electromagnetic showers, resulting in scintillation light emission. To measure the energy of incoming particles, the relatively low light yield is detected by photo-diodes. In the barrel region, Silicon Avalanche Photo-Diodes (APDs) are utilized, while vacuum photo-diodes are employed in the endcap regions. In front of the endcap crystal calorimeter, a preshower detector is positioned, consisting of two layers of silicon strip detectors. This additional detector aims to identify neutral pions that decay into pairs of photons.

48

2.2.4 Hadron Calorimeter

The hadron calorimeter is used to measure the energy of hadronic showers generated by particles that primarily interact via the strong force. It also contributes to the determination of the missing transverse energy, which is particularly important in searches for stable neutral particles like neutrinos (refer to Section 2.4.6).

Compared to electromagnetic showers, hadrons have a significantly longer characteristic interaction length. To account for that, the HCAL is constructed as a hadronic sampling calorimeter, meaning it measures the position, energy and arrival time of a particle using alternating layers of absorber and fluorescent scintillator materials that produce a rapid light pulse when the particle passes through. It consists of brass absorber material, with stainless steel utilized in the innermost and outermost regions, sandwiched between thin layers of plastic scintillators. Within the scintillator layers, wavelength-shifting fibers are integrated. These fibers convert the light emitted by the scintillators when a particle passes through, allowing the signal to be channeled to a hybrid photo-diode for detection and measurement. The HCAL is organised into barrel (HB and HO), endcap (HE) and forward (HF) sections. There are 36 barrel wedges, which form the last layer of detector inside the magnet coil. A few additional layers, the HO, sit outside the coil, ensuring no energy leaks out the back of the HB undetected. Similarly, 36 endcap wedges measure particle energies as they emerge through the ends of the solenoid magnet. Spanning a region of up to $|\eta| < 3.0$ including the endcaps, and up to $|\eta| < 5.0$ including the forward calorimeter, the hadron calorimeter completely surrounds the tracking system and the ECAL.

2.2.5 Muon Chambers

The muon systems, situated in the outermost region of the detector, is designed to detect muons. Unlike other charged particles, muons can traverse the inner tracking system and the calorimeters with minimal energy loss. Four layers of muon stations with three types of gaseous detectors are integrated in the iron yoke surrounding the solenoid.

In the barrel region of the muon system, drift tube chambers (DTs) are employed to detect muon hits, ensuring precise position resolution. In the endcap regions, cathode strip chambers (CSCs) are utilized to cover a wider angular range and maintain excellent position accuracy. The combination of DTs and CSCs detectors enhances the overall performance of the muon system. To facilitate efficient triggering, the muon system is complemented by resistive plate chambers (RPC) in the region where $|\eta| < 1.6$. These RPCs provide a high time resolution, which is crucial for effective triggering processes [89]. A sketch of a quadrant of the CMS detector including the muon systems is shown in Figure 2.5.
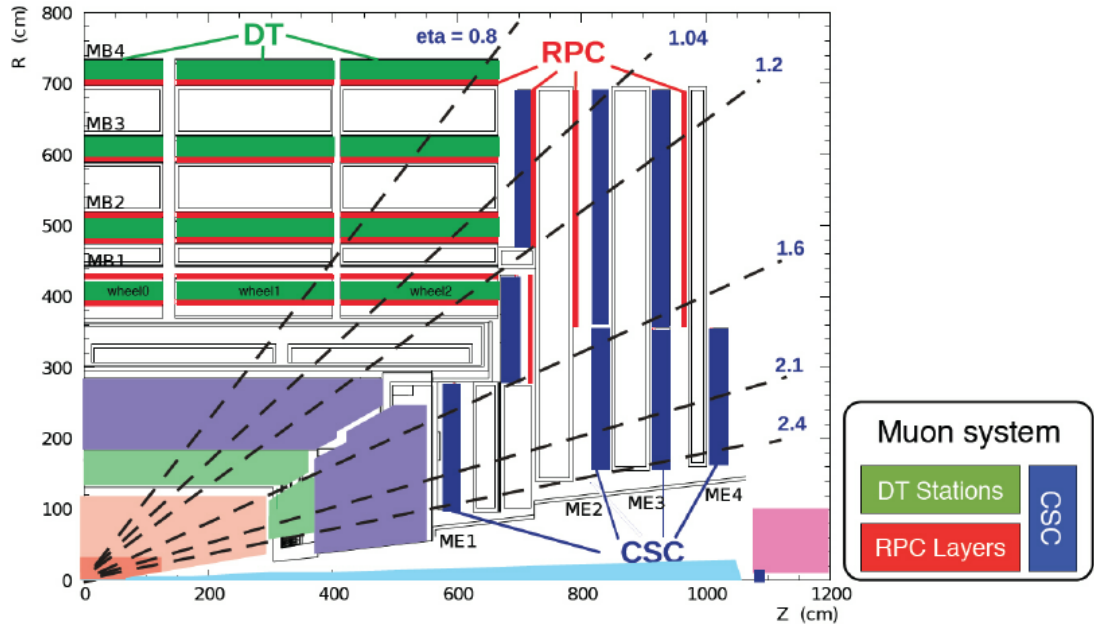
Figure 2.5: Longitudinal layout of one quadrant of the CMS detector including the muon detectors: the four drift tube stations (DT) in the barrel (MB1–MB4, green), the four cathode strip chamber stations (CSC) in the endcap (ME1–ME4, blue), and the resistive plate chamber stations (RPC) in both the barrel and the endcap (red) [99].

2.2.6 Trigger Systems

With the LHC design luminosity and nominal bunch crossing rate of 40 MHz, up to about 10^9 proton-proton interactions per second occur in the CMS experiment during data taking. However, not all detected events can be recorded and processed due to the high event rate, i.e., multiple interactions occur within the same bunch crossing. To address this challenge, a multistage trigger system is employed [89]. The CMS trigger system consists of two main components: the level-1 (L1) trigger system, which is hardware-based, and the high-hevel trigger (HLT), which is software-based [100].

The level-1 trigger is a fast process that searches for basic signatures of interesting physics in an event. It relies only on information from the muon system and the calorimeters to make trigger decisions. The reconstruction of objects and global observables, such as photons, electrons, muons, and jets, including their transverse momentum, is performed extremely quickly, with reduced precision compared to offline reconstruction. Subsequently, a data rate of 100 kHz (design value) is transferred from buffers near the individual detector components to the front-end readout. The data acquisition (DAQ) system then gathers the detector information, providing the specialized HLT software with a complete data readout. The HLT utilizes the L1 candidates and information from all sub-detectors to construct higher-level objects, further reducing the number of

recorded events to around 1 kHz. The recorded data are stored and processed within the CMS offline computing system, which facilitates data analyses.

2.3   Particle Reconstruction

In order to get from the measurements in the various components of the CMS detector to pysical objects such as muons, jets, or missing transverse momentum, the information from all sub-detectors is combined and translated such that single particles can be identified by their specific signatures in the detector. This is achieved by the Particle-Flow event reconstruction algorithm (PF). Complementary to PF, specific reconstruction techniques for individual particle or signature types can be employed, often to enhance the reconstruction efficiency in a specific kinematic region, as for example for low-momentum muons in the analysis presented in this thesis. The steps of the reconstruction and identification of physics objects and events that are of importance for the search outlined in this thesis are further explained in the following sections.

2.3.1   Track Reconstruction

In a vacuum filled with a uniform magnetic field, charged particles will follow a helical path. In the nearly uniform magnetic field of the CMS tracker the trajectory of a charged particle can be approximated by a helix. A helix is defined by five parameters, which for the track reconstruction in CMS are: d_0, z_0, the angle of rotation ϕ, the cotangents of the dip angle θ and the transverse momentum

$$p_T = \sqrt{p_x^2 + p_y^2}, \tag{2.5}$$

of the track.

These parameters are evaluated at the point of closest approach from the track to the measured beam spot, (x_0, y_0, z_0), which is called the impact point of a track. The beam spot refers to the three-dimensional position of the colliding beams at the interaction point. It represents the region where the two beams of particles cross and interact, and its precise determination is crucial for accurately reconstructing the trajectories and interaction points of particles produced in collisions. For more detail on the reconstruction of the beam spot in CMS, [101] can be considered. Subsequently,

$$|d_0| = -|d_{xy}| = -\sqrt{x_0^2 + y_0^2},$$

and $|d_z|$ define the coordinates of the impact point in radial direction (r) and along the beam line (z), respectively. The transverse momentum of a track, p_T, is related to the signed inverse radius of curvature $\frac{1}{R}$ via

$$\frac{1}{R} \propto \frac{B}{p_T} \sqrt{1 + (\tan(\theta))^2}, \tag{2.6}$$

for a magnetic field of strength B. Therefore, subjected to the same magnetic field, a low-transverse-momentum particle has a more narrow (curling) trajectory, while a very high-transverse-momentum particle of the same type can almost travel a straight line.

To reconstruct the trajectories of charged particles, signals from the tracking detector above a certain threshold are transformed into reconstructed hits in two steps: first, so-called clusters are formed from neighboring pixels or strips with a hit. Second, these clusters are converted into reconstructed hits, which possess position information with corresponding uncertainties in the local coordinate system of the silicon sensors. These reconstructed hits are used as the input for the main reconstruction step, the global reconstruction.

In the global reconstruction process, tracks are reconstructed by the *combinatorial track finder* from the hits with the goal to provide momentum and a global position information for the charged particles along with their trajectory through the tracking detector. The global reconstruction is subdivided into four major steps:

1. Trajectory seeding: starting points for the tracks are identified;

2. Pattern recognition: all hits possibly corresponding to the trajectory of a track are collected;

3. Final fit: collected measurements are fitted using the Kalman Filter [102, 103], reconstructed track candidates are produced;

4. Quality & cleaning: tracks that pass certain filters are labeled with quality flags; wrongly reconstructed tracks are discarded.

The Kalman Filter is a mathematical technique used for estimating the state of a dynamic system based on incomplete and noisy measurements; the effect of the material, and inhomogeneities of the magnetic field are taken into account, which cause the particle to not fly on a perfect helix; The equations of motion have to be solved numerically. This is done with the use of a detailed map of the magnetic field that was measured to a precision $<$ 0.01 % [101] before LHC collisions.

Track reconstruction follows an iterative approach, where the four stages described above are performed multiple times in sequence. For each iteration, the hits associated to highest purity tracks are removed from further consideration. Tracks are selected on the basis of the number of hit layers (N_{layers}), the goodness of the final fit, the χ^2 divided by the number of degrees of freedom χ^2/dof, and the compatibility of the track with the leading vertex or pileup vertices. Quality requirements are imposed to the tracks to reduce the rate of fake tracks, which are reconstructed tracks that are not truly the result of single charged particle. Afterwards, the algorithm runs again with progressively looser algorithmic cuts, to recover tracks that would be discarded by too stringent requirements, such as tracks from secondary decay vertices that do not originate in the primary interaction vertex. In total, ten iterations of the combinatorial track finder are run in the nominal track reconstruction.

Adjustments in the positions of various components within the tracking detectors, which are influenced by the operational conditions during data collection, necessitate regular updates to the geometry of the detector. This is crucial for ensuring precise characterization of the spatial arrangement, orientation, and curvature of the tracker modules. The process employed to determine the updated parameters of the tracker's geometry is termed alignment. This alignment procedure is carried out multiple times while data are being collected, utilizing reconstructed tracks from both collision and cosmic ray muon data. Subsequently, it is further refined after the data collection phase concludes [104].

The average number of interactions per bunch crossing increased from about 25 in the LHC runs with 50 ns bunch spacing up to a limit of 50 pileup events per crossing after the LHC switched to a 25 ns spacing with the start of Run 2. The simultaneously enlarged instantaneous luminosity led to increased pileup. Since the tracking is mainly a combinatorial problem, pileup has a strong effect on the tracking efficiency, accuracy, leading generally to a high occupancy in the tracker.

Despite these challenges, the tracking algorithms reconstruct tracks over a pseudorapidity range of $|\eta| < 2.5$, finding charged particles with a p_T as low as 0.1 GeV, or produced as far as 60 cm from the beam line (such as pions from K^0 decays) [101].

One approach to assess the performance of the track reconstruction is by evaluating the reconstruction efficiency for charged particles in simulated $t\bar{t}$ events. The use of simulated inclusive $t\bar{t}$ events with superimposed pileup interactions provides a good estimate of the average LHC conditions in terms of the complexity for track reconstruction. The track reconstruction efficiency, presented in Figure 2.6 is derived in simulated $t\bar{t}$ events, considering p_T and η as variables. These events are simulated at a center-of-mass energy of $\sqrt{s} = 13$ TeV under various pileup conditions. The track reconstruction efficiency is quantified as the ratio of simulated particles associated with a reconstructed track to all simulated charged particles. A simulated particle is considered as associated with a reconstructed track if the fraction of shared hits between them exceeds 75%.

The drop in efficiency for p_T below 0.9 GeV (cf. Figure 2.6) can be attributed to hadron-nucleus interactions, particularly the increased pion-nucleus cross-section for pions with such low momenta. The majority of charged particles produced in LHC collisions are hadrons, experiencing multiple scattering, energy loss through ionization, and, most significantly, elastic and inelastic nuclear interactions. Additionally, track selection criteria are more stringent for low- p_T tracks. In $t\bar{t}$ events, charged particles with very high momentum are primarily produced within jets. The choice of the pion mass as an estimate for all particles during the trajectory-building step, when estimating potential scattering effects, is a reasonable assumption for relativistic particles but becomes less accurate at lower energies when the masses become more significant. The inadequacy of the tracking algorithm to handle such high particle densities results in the efficiency drop for $p_T > 80$ GeV. An increase in pileup marginally degrades the efficiency.
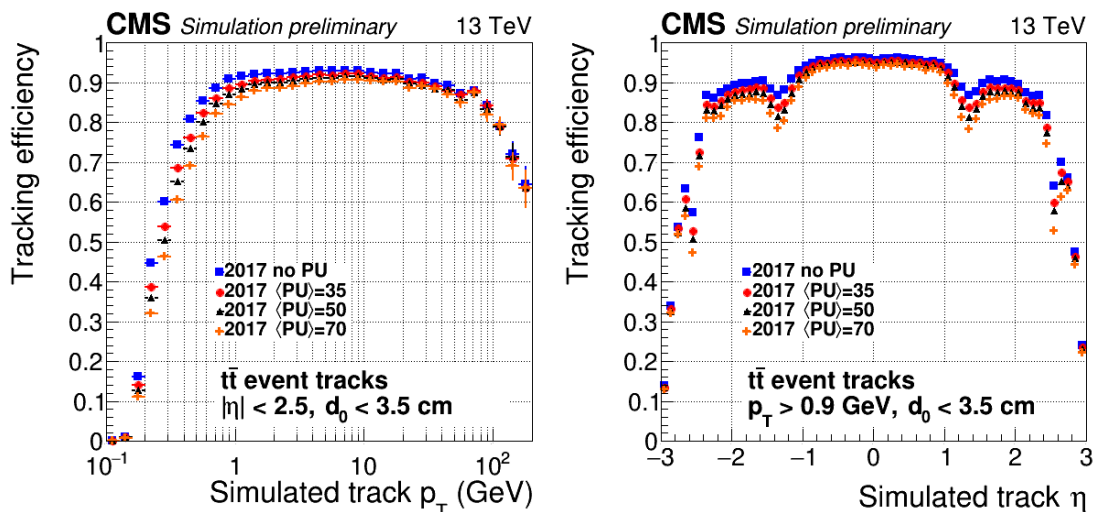
Figure 2.6: The efficiency in simulated $t\bar{t}$ events with different superimposed pileup interactions, generated randomly as Gaussian distributions with a mean number of primary vertices given as $< \mathrm{PU} >$. The efficiency is shown for tracks that fulfill the high-purity requirements and simulated particles generated with a production point $|d_0| < 3.5$ cm, and within $|\eta| < 2.5$ (as a function of p_T, left), or with $p_T > 0.9$ GeV (as a function of η, right), respectively [105].

2.3.2 Vertex Reconstruction

The silicon pixel detector is important for the reconstruction of the tracks of charged particles and for the reconstruction of primary and secondary vertices. Using the reconstructed tracks, the primary-vertex (PV) reconstruction aims to measure the location and the associated uncertainty of all proton-proton interaction vertices in an event. Events from collisions with high track density and many particle interactions in the tracker volume are the main challenges for the vertex reconstruction.

The reconstruction of vertices involves finding vertices based on a given set of tracks (e.g. a jet), or the full event, (e.g. in case of primary vertex finding). It also includes the determination of the vertex position, assuming it is formed by a given set of tracks, in the vertex fitting. The goodness of the fit may be used to accept or discard a vertex hypothesis. In addition the vertex fit is often used to improve the measurement of track parameters at the vertex.

The vertex-finding algorithms differ depending on the physics case (primary or secondary vertex finding, reconstruction of exclusive decays, etc.) and not all are part of the CMS standard reconstruction sequence. For the PV reconstruction, the vertex reconstruction is made by the Kalman Vertex Finder [103], which applies the principles of the Kalman filter. The algorithm takes into account various sources of uncertainty such as the covariance matrix of the tracks, including measurement errors and multiple scattering, to

iteratively refine the estimation of the particle tracks and the position of the vertices. It starts with an initial estimate of a vertex position and the parameters of the particle tracks. The Kalman Vertex Fitter updates these estimates using a combination of the measured data and the predictions based on the previous state estimation, as the calculations of the particle trajectories are updated. By incorporating both, the current measurements and the knowledge of the particle's behavior, the algorithm provides an optimal estimate of the vertex position and the track parameters.

The track selection involves choosing tracks consistent with being produced promptly in the primary interaction region, by imposing requirements on the maximum value of significance of the transverse impact parameter relative to the center of the beam spot, the number of strip and pixel hits associated with a track, and the normalized χ^2/dof from the fit to the trajectory. The selected tracks are further clustered on the basis of their z-coordinates at their point of closest approach to the center of the beam spot. This clustering allows for the reconstruction of any number of proton-proton interactions in the same bunch crossing. The leading vertex is then defined as the vertex with the largest sum of charged tracks, jets and missing energy among the so found vertices. Often, the term *the PV* is used when only the leading vertex is meant. The remaining vertices are from pile-up interactions or LLPs.

Figure 2.7 shows the spatial resolution of the primary vertex reconstruction as a function of the number of tracks associated to the vertex, using both minimum-bias and jet-enriched data samples at $\sqrt{s}$=7 TeV. No comparable measurement has been performed with 2016 data at $\sqrt{s}$=13 TeV at the current state. The resolution in y is almost identical to that in x, and is therefore omitted. The resolution of the position of a PV depends on the number of tracks taken into account for the reconstruction and the p_T of those tracks. For more than 50 tracks originating from the PV the spatial resolution is around 10 - 15 μm in x/y-direction and around 20 μm in z-direction. The tracks in the jet-enriched data set have significantly higher mean p_T, resulting in higher resolution in the track impact parameter and consequently better vertex resolution [96, 101].

2.3.2.1   Secondary Vertex Reconstruction for LLPs

The decay of LLPs, be that SM particles with longer lifetimes such as kaons, pions, or potential BSM particles such as HSCPs (cf. Section 1.3.2), results in a second (i.e. secondary) decay vertex in an event, which can be reconstructed given the decay happens within the detector volume. The quality and cleaning procedure in the CMS vertex reconstruction process however, especially constraints on the minimum number of tracks and the maximum displacement of the vertex, exclude secondary vertices from the reconstruction with only few exceptions[1].

---

[1]A trimmed version of the Kalman Vertex Finder is used in CMS to reconstruct secondary vertices inside jets from b-hadron decays using tracks that were discarded from the PV finding. These vertices involve tracks within a jet with a minimum p_T of 1 GeV and a maximum transverse displacement from the PV of 2 mm.
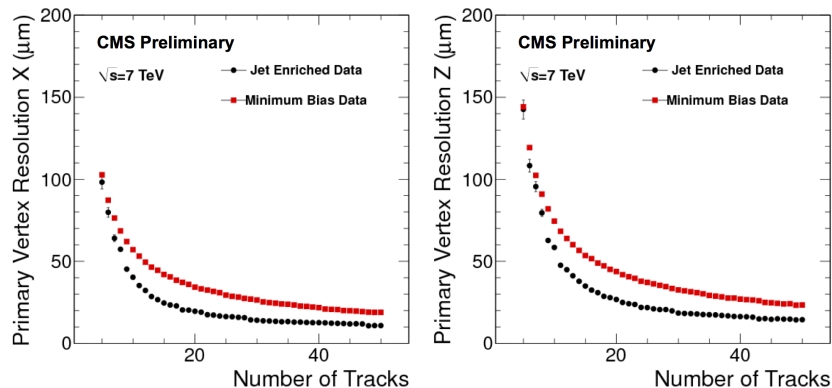
Figure 2.7: Primary-vertex resolution in x (left) and in z (right) as a function of the number of tracks at the fitted vertex, for two kinds of events with different average track p_T values [101].

For the reconstruction of the targeted signal processes in the analysis presented in this thesis, a sensitivity to secondary vertices in the region of 100 μm to 10 cm is required (cf. Section 3.5). For this purpose an adapted version of the $V0$ Fitter is used. The $V0$ Fitter is a reconstruction algorithm for SV from neutral strange hadrons (K^0 and Λ^0, collectively known as $V0$ particles) using oppositely charged track pairs. Intrinsically, it uses also the Kalman Vertex Fitter described above.

Selected tracks are taken as input to the fitter to reduce combinatorics (cf. Section 3.6.3). These tracks are transformed into so-called transient tracks. These are track objects useful for higher-level reconstruction, which encode information about the magnetic field and the tracker geometry, to estimate the track parameters at arbitrary points along a given trajectory.

Afterwards, during the SV fit procedure, the distance of closest approach (DCA) and the 3D point of closest approach (PCA) between each oppositely charged transient track pair is calculated. This is done using the closest approach in the $r - \phi$ plane. Given two trajectories, the point of closest approach in the transverse plane for the helices extrapolated from these is determined. As helices are circles in the transverse plane, three cases are distinguished concerning their intersections: either the circles have one, or two intersection points; or the circles do not cross; In the first case, the crossing point is unambiguous and defines the PCA in the transverse plane. The corresponding z-coordinate is computed along with the 3D PCA and DCA. In the second case, the circles have two intersections. The point for which the z-coordinates on the two transient tracks are the closest is chosen as the PCA. In the third case the PCA is defined by the point of closest approach of the two circles with the corresponding z-coordinate.

The momenta of both transient tracks are calculated at the PCA assuming the pion mass in the trajectory fit to account for material effects. Finally, the track parameters of the

two tracks used in the SV are updated with the results of this refit. After the refitting, quality criteria are applied to the SV to reduce the amount of spurious vertices.

The $V0$ Fitter is used to determine the reconstruction performance for SVs in CMS [106]. The results are shown in Figure 2.8. The invariant mass of K_s^0 (Λ^0) particles is reconstructed from oppositely-charged pion (and proton) candidates in data. A fit is performed using a double-gaussian with a common mean for the signal, plus a linear (quadratic) polynomial for the background. As can be seen, the $V0$ Fitter provides excellent resolution on the invariant mass with an average σ of below 10 MeV. The overall shape as a function of η is well described by simulation. The 0.5 MeV shift for K_s^0 is attributed to imprecise modeling of detector material. For completeness, the invariant mass reconstructed from oppositely-charged pion/proton candidates in simulation and the invariant mass as a function of p_T, ϕ, and the decay length are shown for K_s^0 and Λ^0 in the Appendix (cf. Appx. A.1).

2.3.3 Muon Reconstruction

The reconstruction of muons in CMS is performed in three different ways, but always requires signals in the muon system. In the first approach, muon trajectories of standalone muons are reconstructed from all segments in the muon system, similar to the track reconstruction. Compatibility with the interaction point is imposed to reconstruct only muons produced in LHC collisions (no cosmic ray muons). In the second approach, tracks from the tracker fulfilling certain quality criteria are extrapolated to the muon system. They are considered tracker muons when they match at least one reconstructed muon segment. A tracker muon is reconstructed from tracks with $p_T > 0.5$ GeV and $p > 2.5$ GeV. In the third case, global muons are reconstructed in an outside-in approach, checking for each reconstructed standalone muon its compatibility with the reconstructed tracks in the tracking system [107].

2.4 Particle Identification

The standard tool for particle identification in CMS is the **Particle-Flow algorithm** (PF) [108, 109]. The PF algorithm combines information from all sub-detectors of the CMS detector to enhance particle identification and reconstruction. It aims to link individual detector measurements to arrive at a collection of final state objects, satisfying certain requirements. This collection includes leptons, charged and neutral hadrons as well as the missing transverse momentum in an event, which are of special importance to this analysis. The PF algorithm makes use of three main ingredients: reconstructed tracks of charged particles passing the tracking system, clusters from both calorimeter, and tracks from the muon chambers. Consequently, a high track-reconstruction and calorimeter clustering performance are key to the PF algorithm. The reconstruction procedure of tracks and muons is briefly described in Section 2.3.
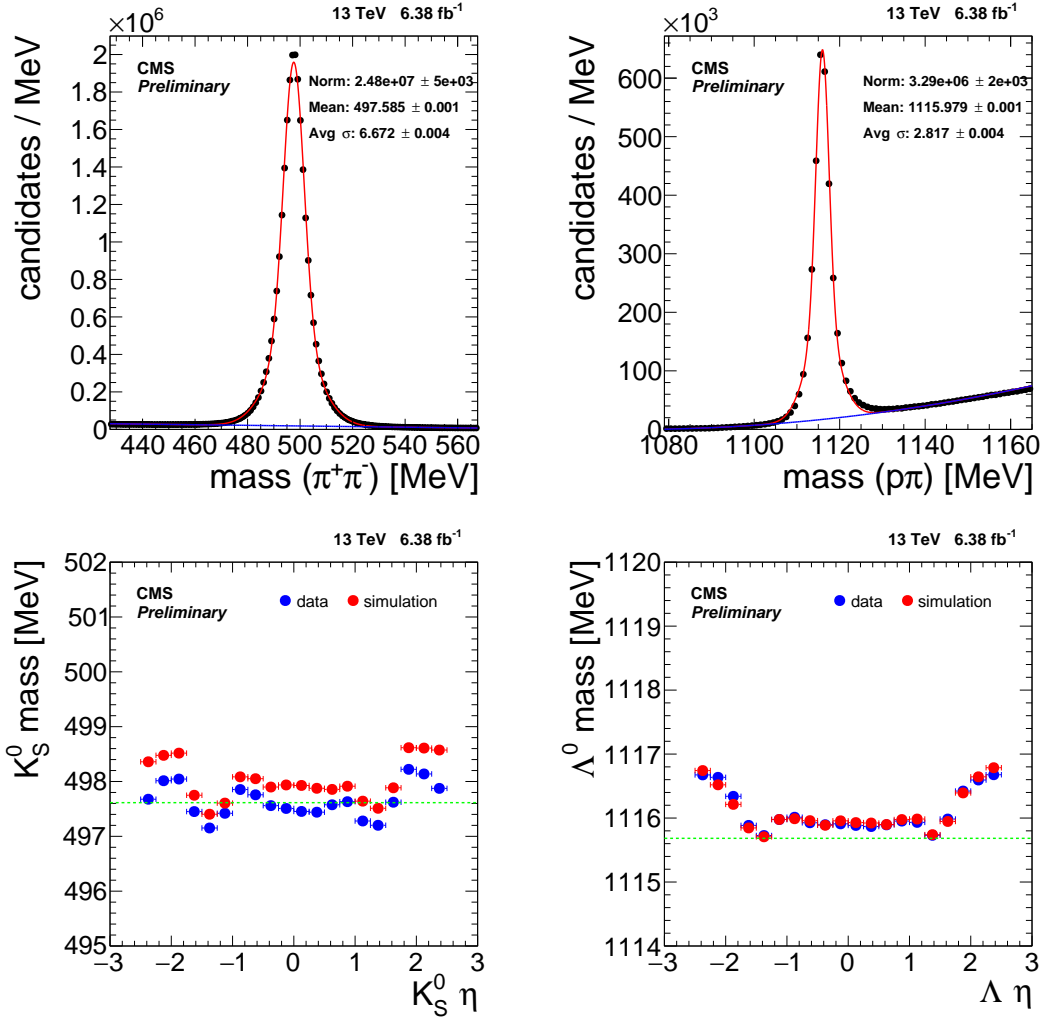
Figure 2.8: Top: Invariant mass of $V0$ particles reconstructed from oppositely-charged pion (and proton) candidates in 2016 data. A fit is applied to the number of K_s^0 (Λ^0) candidates in the left (right) Figure, using a double-gaussian with a common mean for the signal (red line), plus a linear (quadratic) polynomial for the background (blue line). Bottom: Invariant mass as a function of η for data (blue points) and simulation (red points). The expected mass of the K_s^0 (Λ^0) particles is contained in the plot (dashed green line). [106].

2.4.1 PF Muons

In the PF algorithm, global and tracker muons are considered. Charged hadrons may be mis-reconstructed as muons if some of the hadron shower remnants reach the muon system (punch-through). In order to reject hadrons, mis-identified as muons, additional inner tracks and calorimeter energy deposits within an angular distance of $\Delta R < 0.3$

to the muon are summed and must not exceed 10% of the transverse muon momentum. This acts as an isolation requirement.

2.4.2 Soft Muon Identification

The PF muon identification is designed to retain prompt muons (e.g., from decays of W and Z bosons), as well as muons from hadrons (e.g., from decays of pions). In contrast, the soft muon identification (soft ID) aims to achieve efficient identification of low-momentum muons from decays of quarkonia states. A *soft muon* is a tracker muon with a tracker track with a χ^2/dof of the track fit smaller than 1.8 and hits from at least six layers of the inner tracker including at least one pixel hit. The tracker muon reconstruction must have tighter muon segment matching compared to PF muons. Moreover, a soft muon is only loosely compatible with the primary vertex, having a transverse impact parameter $|d_{xy}| < 3$ cm and a longitudinal impact parameter $|d_z| < 30$ cm [108].

The efficiency of the soft muon reconstruction and identification as a function of the muon p_T in 2010 data ($L_{\text{int}} = 40$ pb^{-1}) and simulation is shown in Figure 2.9. The soft muon efficiency contains the efficiency of muon reconstruction in the muon system, including the matching of this muon to the tracker track, and the efficiency of the ID criteria. The measurement is made by applying the tag-and-probe technique to muons from $J/\Psi \to \mu\mu$ decays. In that method, the tag muons are well identified, triggered muons with tight selection criteria, while the probe muons consist of an unbiased set of muon candidates. The efficiency ϵ is given by the fraction of probe muons that pass the soft muon identification criteria:

$$\epsilon = \frac{\text{probe muons passing the soft ID}}{\text{all probe muons}}. \tag{2.7}$$

The denominator corresponds to the number of resonance candidates (tag+probe pairs) reconstructed in the dataset. The numerator corresponds to the subset for which the probe passes the criteria. The invariant-mass distribution from the tag-and-probe is used to select signal from J/Ψ candidates decaying to dimuons. As can be seen, the efficiency to reconstruct and identify soft muons with $p_T \approx 1$ GeV is still around 60 % for muons reaching the tracker endcaps.

2.4.3 PF Electrons and Photons

The possibly large energy losses of electrons due to bremsstrahlung that can change the direction of the electron significantly, make the detection of electrons especially challenging. Similar to the detection of photons, which can convert into electron-positron pairs. The PF algorithm incorporates two approaches to identify isolated electrons and photons.

The Gaussian Electron Driver (ged) algorithms make use of Gaussian-shaped energy distributions to model the energy deposition patterns of electrons and photons in the
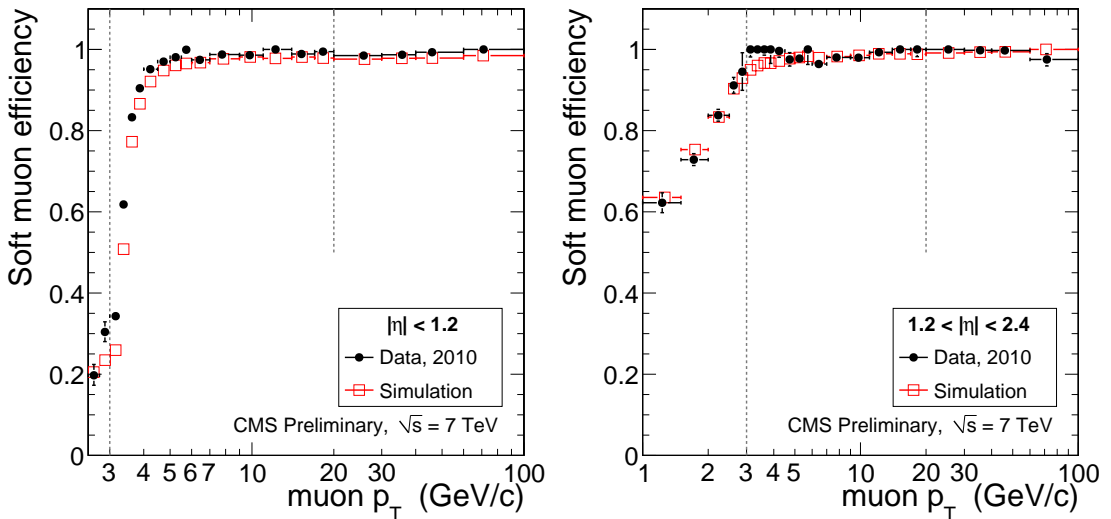
Figure 2.9: Soft muon reconstruction and identification efficiency as a function of the muon transverse momentum in 2010 data and simulation ($L_{\text{int}} = 40 \text{ pb}^{-1}$) in the tracker barrel (left) and endcaps (right) [110].

calorimeters. The deposited energy in the ECAL is measured in clusters of clusters (superclusters). Superclusters are matched with charged particle tracks from the tracker to improve electron reconstruction. Afterwards, criteria based on the ECAL energy, shape, and track agreement are applied. For electrons, calorimeter deposits with $E > 4$ GeV are considered and an energy deposition in the HCAL in a cone of $\Delta R < 0.15$ around the electromagnetic energy deposit is required not to exceed 10% of the energy measured in the ECAL. Tracks are then iteratively linked with the energy deposit if the track momentum and the measured energy deposit is compatible with the electron hypothesis. For photons similar criteria as for electrons are used, without requiring associated tracks and excluding clusters that have already been associated to electrons.

For non-radiating electrons with $p_T > 2$ GeV, an optimized track reconstruction for electrons is performed in order to account for changes in the direction through radiation losses. A Gaussian sum filter (gsf) is used in place of the Kalman Filter (cf. Section 2.3.1). A resulting track with a fit result $\chi^2/\text{dof} \approx 1$ which can be matched to a deposit in the electromagnetic calorimeter is then classified as an isolated electron, unless the energy deposit itself can be matched to ≥ 3 tracks. Contrarily, energy deposits in the electromagnetic calorimeter without a linked track are classified as photons [111].

2.4.4 PF Hadrons and Jets

Once muons, electrons, and isolated photons are identified, the remaining particles to be identified are hadrons from jet fragmentation and hadronization. The ECAL and HCAL clusters not linked to any track give rise to photons and neutral hadrons. Within

the tracker acceptance, all these ECAL clusters are turned into photons and all HCAL clusters are turned into neutral hadrons. This procedure is motivated by measurements showing that in hadronic jets, 25% of the jet energy is carried by photons. Neutral hadrons leave only 3% of the jet energy in the ECAL. Beyond the tracker acceptance, ECAL clusters linked to a given HCAL cluster are assumed to arise from the same (charged- or neutral) hadron shower, while ECAL clusters without such a link are classified as photons.

Due to QCD confinement, quarks and gluons create a collimated spray of hadrons, which appear as a cluster of energy deposited in a localized area of the detector, called a jet. Thus, jets provide a link between the observed particles and the underlying physics at the partonic level, and consist mainly of hadrons and photons. Proton constituents, which are final state quarks or gluons, are called partons. The identification of such jets requires a clustering of the PF candidates to a jet. This way, the jet energy can be inclusively measured by the calorimeters.

It is possible to reconstruct several types of jets, based on different algorithms. Moreover, it is possible to subtract charged particles from pile-up vertices before clustering and to calibrate the energy of the jets and propagate these corrections onto missing transverse momentum [112].

The most common algorithm used by CMS for the clustering of PF particles into jets is the anti-kt algorithm (AK). It iterates over particle pairs, finds the two closest and determines whether to combine them. For this purpose, the distance of the particles d_{ij} and the beam distances d_{iB} are calculated:

$$d_{ij} = \min(p_{T,i}^{-2}, p_{T,j}^{-2})\frac{\Delta R_{ij}^2}{R^2}$$
$$d_{iB} = p_{T,i}^{-2}.$$
(2.8)

Afterwards, the particles with the smallest distance d_{ij} are combined or, if d_{iB} is smallest, a new proto jet is defined. This procedure is repeated until no particles are left. By the negative momentum power, higher momentum particles are clustered first. This leads to jets with a round shape which tend to be centered on the hardest particle. Different cone sizes ΔR can be used in Equation 2.8. A larger ΔR captures more particles within the jet cone and tends to merge softer particles into a single jet. Typically, values of $\Delta R = [0.4, 0.8]$ are used. Subsequently, jets found by the AK with $R = 0.4$ are also referred to as *AK4-jets*.

A the LHC, the identification of jets originating from heavy flavour quarks (*b* or *c*-tagging) is of special importance for searches for new physics and for measurements of SM processes. Thus, a variety of algorithms have been developed by CMS to select *b*-quark jets based on variables such as the impact parameters of particle tracks, properties of reconstructed decay vertices, and the presence or absence of a low-momentum lepton.

These algorithms heavily rely on machine learning tools since the start of Run 2. One prominent example of a b-tagging algorithm used by CMS is the DeepCSV, which uses a deep neural network.

2.4.5 Tau Lepton Identification

Tau leptons can decay into different final states, referred to as decay modes. These include decays with one or three charged particles (accompanied by neutrinos), e.g. one or more charged hadrons. The reconstruction of hadronically decaying tau leptons (τ_h), is operated in CMS with the hadron-plus-strip (HPS) algorithm, which works on top of PF objects. The HPS aims to search for the τ_h decay products, which tend to form a collimated and well isolated jet. Therefore, the HPS uses as input the jets clustered from PF and assigns different decay modes to the τ_h by counting its number of charged hadrons and ECAL clusters. Moreover, a convolutional deep neural network (DNN) and boosted decision tree (BDT) are employed for further identification. Both take as input information on high-level variables, such as quantities related to the lifetime of the τ_h candidate, isolation, and information on the PF hadrons, muons, electrons and photons in the jet. From the classifier outputs, tau lepton discriminants are derived, which efficiently reject misidentified muons, electrons and jets.

2.4.6 PF Missing Transverse Momentum

The missing transverse momentum $|\vec{p}_T^{\text{miss}}|$ is defined as the absolute value of the negative vectorial sum over the p_T of all PF particles above a certain p_T threshold visible in the event:

$$|\vec{p}_T^{miss}| = |-\sum_i \vec{p}_{T_i}|. \qquad (2.9)$$

Neutral particles that only interact weakly, such as neutrinos, or DM candidates such as neutralinos (cf. Section 1.3.2), pass through all detector components without leaving signatures. However, since the colliding particles in the LHC ideally have no transverse momentum, neglecting momentum or energy mismeasurements, the PF missing transverse momentum can provide access to the transverse momentum of the sum of all such neutral particles in an event. A precise estimation on the amount of missing transverse momentum requires the correction of the transverse momentum of all jets contained in the event [113].

The combination of $|\vec{p}_T^{\text{miss}}|$ with missing hadronic transverse energy (H_T^{miss}) measurements can provide a more comprehensive understanding of the overall transverse momentum balance in high-energy collision events. The H_T^{miss} is defined similarly to $|\vec{p}_T^{\text{miss}}|$, but it specifically focuses on the hadronic components of the event, which are particles expected to interact strongly with the detector. It is calculated as the absolute value of the negative vectorial sum over the transverse momenta of all hadronic particles with a

$p_T > 30$ GeV and $|\eta| < 5$ in the event

$$H_T^{miss.} = |-\sum_i \vec{p}_{T_i}^{\text{hadronic}}|. \tag{2.10}$$

3 Analysis

In this chapter, a search for electroweakino production at the LHC using two soft opposite-sign (OS) displaced muons is presented. The analysis is optimized for the two scenarios with compressed mass spectra as described in Section 1.3.1.2, which are realized as simplified models. This search targets final states containing two low-momentum, opposite-charge, displaced muons from the leptonic decay $\tilde{\chi}_2^0 \to Z^* \, \tilde{\chi}_1^0$, $Z^* \to \mu\mu$, and a large magnitude of missing transverse momentum from the undetectable lightest neutralinos. The rationale behind the choice of this specific decay channel is discussed in Section 3.5.

Experimental constraints on these compressed scenarios are weak so far due to the small momenta of the visible decay products of below 5 GeV, and because of the small electroweak production cross sections of the order of 10^4 fb and below. Because the leptonic decay products of the $\tilde{\chi}_2^0$ can have low momentum, decreasing with smaller mass splittings, the leptonic decay products often fail identification and only the particle tracks are measured. Previously published analyses [114, 115, 116, 117, 118, 119, 120, 121] targeting the detection of compressed neutralinos have mostly used identified leptons (cf. Section 3.2). This analysis targets the unexplored region of the compressed MSSM phase space with mass splittings between the respective particles below 3 GeV by relaxing the lepton identification criteria and allowing one of the leptons to be reconstructed only as a track. Figure 3.1 shows the reconstruction efficiency of the two muons from a neutralino decay using either reconstructed muons, just the muon tracks, or both. The efficiency of reconstructing the muons is dependent on which detector subsystems are traversed by the muons. Muon pairs with such low p_T mostly fail the global muon reconstruction, because no sufficient traces in the muon systems can be reconstructed. The efficiency to reconstruct just the *tracks* in the inner silicon detectors is significantly higher. Thus, the reconstruction efficiency is highest for the use of the inclusive track selection, but this comes at the cost of thousands of possible pairs per event. For the search presented in this thesis, two tracks are required where at least one of the tracks is required to have a soft muon tag. Thus, the analysis profits from higher reconstruction efficiencies, while still limiting the background through the strict requirements of the muon tag. The two tracks are required to be consistent with originating from a common SV. For this purpose, a dedicated vertexing tool was developed in the scope of this thesis, which is documented in Section 2.3.2.1. Thus, in contrast to previous searches, the distinctive
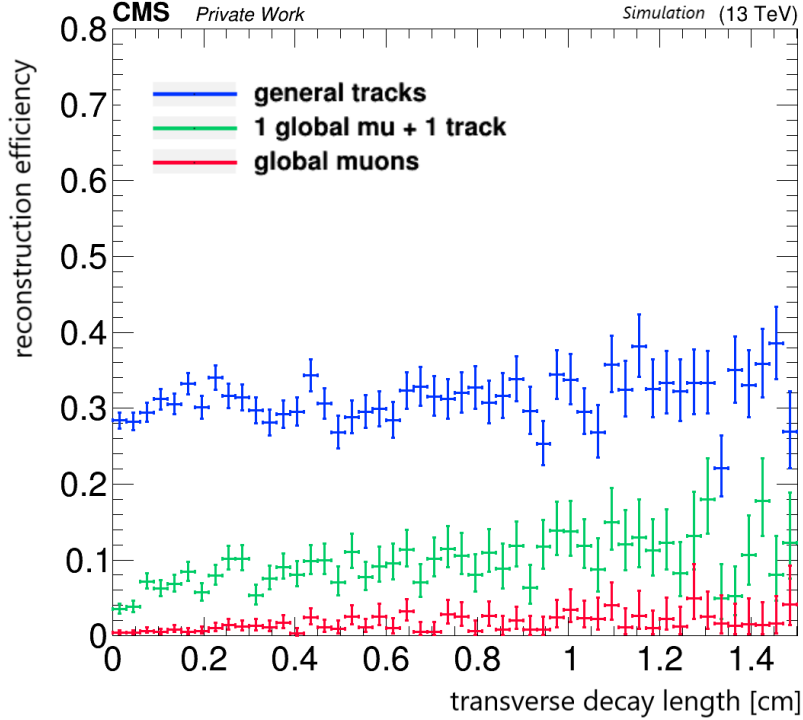
Figure 3.1: Reconstruction efficiency for muon pairs from the decay of the neutralino to the LSP ($\chi_2^0 \to Z^* \chi_1^0$, $Z^* \to \mu\mu$) using the corresponding reconstructed tracks (blue), one track and one identified muon (green), and two identified muons (red) in the full range of the CMS detector. The efficiency is determined in a benchmark signal model point with a $\tilde{\chi}_2^0$ mass of 115 GeV, a mass difference $\Delta m_0 = 1.14$ GeV, and a decay length $c\tau = 5$ mm.

strength of the search presented in this thesis, lies in its capacity to mitigate lepton identification constraints through the incorporation of supplementary SV requirements.

In the following, the targeted signal models in this search are introduced. Next, information on previous searches targeting similar regions of the MSSM phase space through the same signature are given. Next, a description of the experimental and simulated data used for the analysis is given. Thereafter, the strategy and methodology of this search are discussed, starting with a study on the most relevant signal characteristics. This then leads to the discussion of the selection used for potential $\tilde{\chi}_2^0$ candidates. In this context, a displaced low-momentum muon selection is described, which is used along with the V0 Fitter (cf. Section 2.3.2.1) and a multivariate classifier to reconstruct and identify signal vertices with corresponding tracks in candidate events. Next, background sources that may mimic the signature of the signal in the search are identified, and the procedure for estimating them is described. Lastly, sources of experimental uncertainty are identified and the systematic uncertainties are estimated for the background estimation method

and the signal efficiency.

3.1 Signal Models

For the interpretation of the results, two supersymmetric scenarios are identified in the context of the MSSM: the compressed mass higgsino and the bino coannihinaltion model, as introduced in Section 1.3.1.2. These scenarios are realized as simplified models. Simplified models describe hypothetical particles and their production and decay sequences based on a small number of free parameters. Masses for any further new particles not considered in this model are set to infinity.

As introduced in Section 1.3.1.2, the nearly-pure higgsino LSP is a prime DM candidate that has not been excluded by observational data. In the simplified model of compressed mass higgsinos [84], the free parameters are the masses and lifetimes of the lightest long-lived electroweakinos: $\tilde{\chi}_{1,2}^0$ and $\tilde{\chi}_1^\pm$. The minimum allowed mass difference is only attributed to radiative corrections as $M_{1,2} \to \infty$. Further, it is assumed that the second lightest neutralino $\tilde{\chi}_2^0$ is the next-to-next-to-lightest supersymmetric particle (NNLSP) where the relations:

$$m_{\tilde{\chi}_2^0} > m_{\tilde{\chi}_1^\pm} > m_{\tilde{\chi}_1^0}$$
$$\Delta m_0 = 2\Delta m_\pm.$$

$$(3.1)$$

are fulfilled. These relations are consistent with the limit of large $\tan\beta$ in the simplified model described in [84]. In the MSSM, the mass of the pseudoscalar Higgs boson (A^0) and the charged Higgs boson ($H^\pm$), may have masses that are inversely proportional to $\tan\beta$. Therefore, in the limit of large $\tan\beta$, the charged Higgs boson can become relatively lighter and the lightest neutral Higgs boson (h^0) can approach the mass of the Z boson.

For the model of bino-wino-coannihilation as elaborated in Section 1.3.1.2, a bino-like LSP is assumed with a fully mass degenerate wino-like NLSP triplet state. In the bino coannhihilation *simplified* model, the chargino proper decay length is set to $c\tau = (1, 3, 5)$ mm, resulting in different decay lengths in the detector frame, depending on the boost of the decay products of the electroweakinos. Compared to the higgsino simplified model, this results in increased lifetimes in the compressed regime, which is consistent with the neutralino lifetimes when relaxing gaugino universality, .i.e., allowing more complex mass matrices and bino-wino-coannihilation states (cf. Figure 1.9). In this model, the second lightest neutralino is the NLSP along with the chargino:

$$m_{\tilde{\chi}_2^0} = m_{\tilde{\chi}_1^\pm} > m_{\tilde{\chi}_1^0}$$
$$\Delta m_0 = \Delta m_\pm.$$

$$(3.2)$$
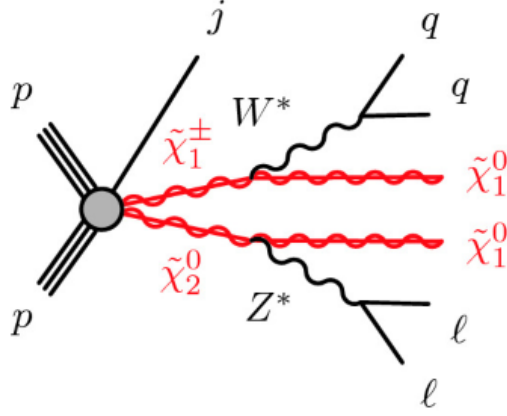
Figure 3.2: Exemplary pair production and decay of electroweakinos in the simplified models considered in this thesis.

In the case of the higgsino simplified model, direct electroweakino ($\tilde{\chi}_1^0$, $\tilde{\chi}_1^\pm$, $\tilde{\chi}_2^0$) pair production is considered, with the possible parings:

$$\tilde{\chi}_2^0 \tilde{\chi}_1^\pm, \ \tilde{\chi}_2^0 \tilde{\chi}_1^0, \ \tilde{\chi}_1^0 \tilde{\chi}_1^\pm, \ \tilde{\chi}_1^\pm \tilde{\chi}_1^\pm. \tag{3.3}$$

Of all possible pairings, $\tilde{\chi}_1^0 \ \tilde{\chi}_1^0$ and $\tilde{\chi}_2^0 \ \tilde{\chi}_2^0$ vanish. In the case of the bino coannhihilation simplified model, also the LSP-associated neutralino production mode ($\tilde{\chi}_2^0 \ \tilde{\chi}_1^0$) vanishes [122, 123]. An example diagram for the production of one $\tilde{\chi}_2^0$ is shown in Figure 3.2. In that case, the $\tilde{\chi}_2^0$ is produced in association with a $\tilde{\chi}_1^\pm$ and decays leptonically. In general, all-hadronic final states, final states with four leptons, and mixed final states can occur through the decay of the produced electroweakinos via off-shell W^* or Z^* or γ^* bosons. However, muon pairs from a common decay vertex can enter the final state only through electroweak decays $Z^* \to \mu\mu$.

For the simulated signal models in this thesis, the branching fraction (BF) of the second lightest neutralino is set to 50% hadronic decays and 50% leptonic decays, whereof 25% are electrons and muons, respectively. A realistic scenario will in general have other decay modes, resulting in different branching fractions. Therefore, the total signal cross section is weighted to match the expected realistic branching ratios. To obtain a realistic scenario, at first order, one can consider the BF of the Z boson to leptons, which is $\approx 30\%$, mainly neutrinos. The branching ratio to charged leptons is approximately 10%, equally distributed between all three generations. However, the BF of the Z^* gives a more accurate description. The BF of the Z^* boson to muons and electrons is approx. 5% for each, as the decay to tau leptons is kinematically forbidden for virtual Z^* in the compressed region of the simplified models (cf. Figure 3.3) [124, 125].

67
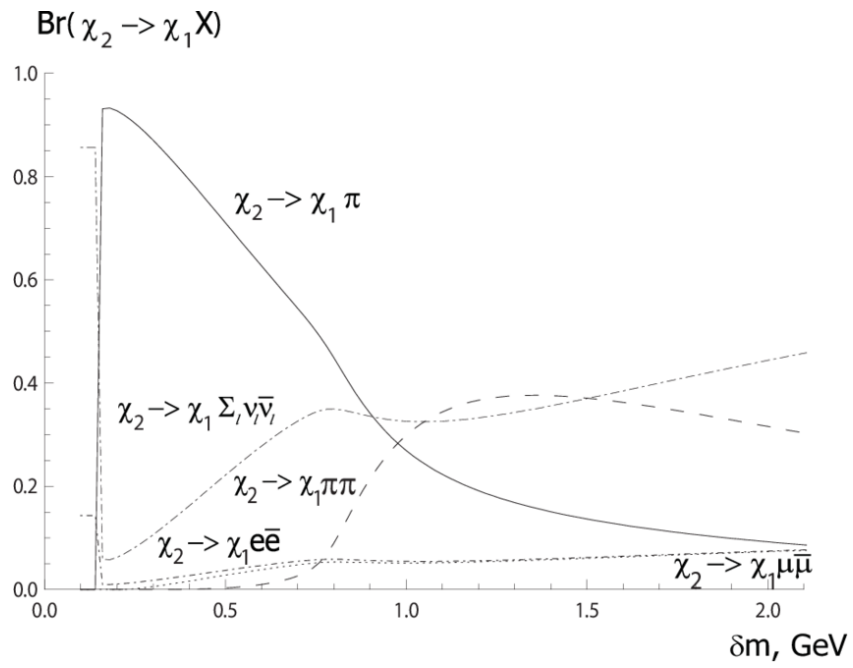
Figure 3.3: Branching ratios (Br) for the decay of the $\tilde{\chi}_2^0$ to the $\tilde{\chi}_1^0 + X$ as a functions of the mass splitting δm. Br is given for the respective particle types X in lines with different styles [124].

3.2 Previous Searches

The focus of this summary is on searches that share similar phase space and final states with this study, specifically those associated with higgsino production involving leptons resulting from the non-prompt decay of compressed electroweakinos. Constraints in these compressed scenarios were initially established at LEP [126], where lower bounds on the chargino mass from direct production were found. Thereafter, the CMS and ATLAS experiments in Run 2 have significantly constrained the MSSM through their searches for new physics [127]. As no supersymmetric particle has been discovered so far, these searches have resulted in exclusion limits on the available parameter space.

The exclusion limits for higgsino production from two ATLAS searches and the LEP results are shown together in Figure 3.4. In this case, constraints on $\Delta m_{\pm}$ directly relate to Δm_0 via Equation 3.1. The ATLAS collaboration has set stringent limits on chargino-neutralino pair production using a search for final states with two or three leptons and missing transverse momentum [114, 115] as well as a search for long-lived charginos based on a disappearing-track signature [116]. The lepton search targets either two identified same-flavor opposite-charge leptons (muons or electrons) or one identified lepton and one track matching to a nonidentified lepton. In the analysis, muons are required to have $p_T > 3$ GeV, while tracks are required to have $p_T > 1$ GeV. Additionally, the angular separation between muons or between a muon and a track must satisfy $\Delta R_{\mu\mu} > 0.05$. Mainly through the requirement of a minimum p_T for the leptons in the ATLAS prompt lepton search, a gap remains in the plane of $\Delta m_{\pm} - m(\tilde{\chi}_1^{\pm})$ between constraints from the disappearing track search and the lepton searches.

Similar searches have been carried out by the CMS collaboration. A search for supersymmetry in final states with two or three soft leptons and missing transverse momentum has been conducted using 137 fb^{-1} of data collected at $\sqrt{s} = 13$ TeV [121]. Final states with two **s**oft **o**pposite-sign **s**ame-flavor leptons are targeted in the analysis which is called the SOS analysis for short. The SOS analysis sets a lower threshold on the transverse momentum of muons, requiring $p_T > 3.5$ GeV. Additionally, it requires a minimum angular separation between the leptons, with $\Delta R_{\mu\mu} > 0.3$. The SOS analysis targets predominantly prompt muons from the electroweakino decay, whereas the analysis outlined in this thesis focuses on displaced signatures. In the higgsino simplified model, excluded $\tilde{\chi}_2^0$ masses up to 205 GeV for a mass splitting $\Delta m_0 \approx 7.5$ GeV, and 150 GeV for a more compressed scenario with $\Delta m_0 \approx 3$ GeV. In the bino-wino coannihilation model, only mass splittings greater 6 GeV are excluded. Figure 3.5 shows the expected and observed exclusion contours where $\tilde{m}_{\tilde{\chi}_1^0} \times \tilde{m}_{\tilde{\chi}_2^0} < 0$, since this is the combination allowed when the higgsino is the LSP. In addition, a search for long-lived charginos using disappearing tracks with the CMS experiment excludes chargino masses up to $m_{\tilde{\chi}_1^{\pm}} \leq 210$ GeV and mass splittings $\Delta m_{\pm} < 0.3$ GeV [118] for a simplified model featuring a nearly-pure higgsino DM candidate (cf. Figure 3.6) .

The analysis presented in this thesis aims to extend these exclusion limits towards smaller Δm compared to the SOS analysis and larger Δm with respect to the search for disap-
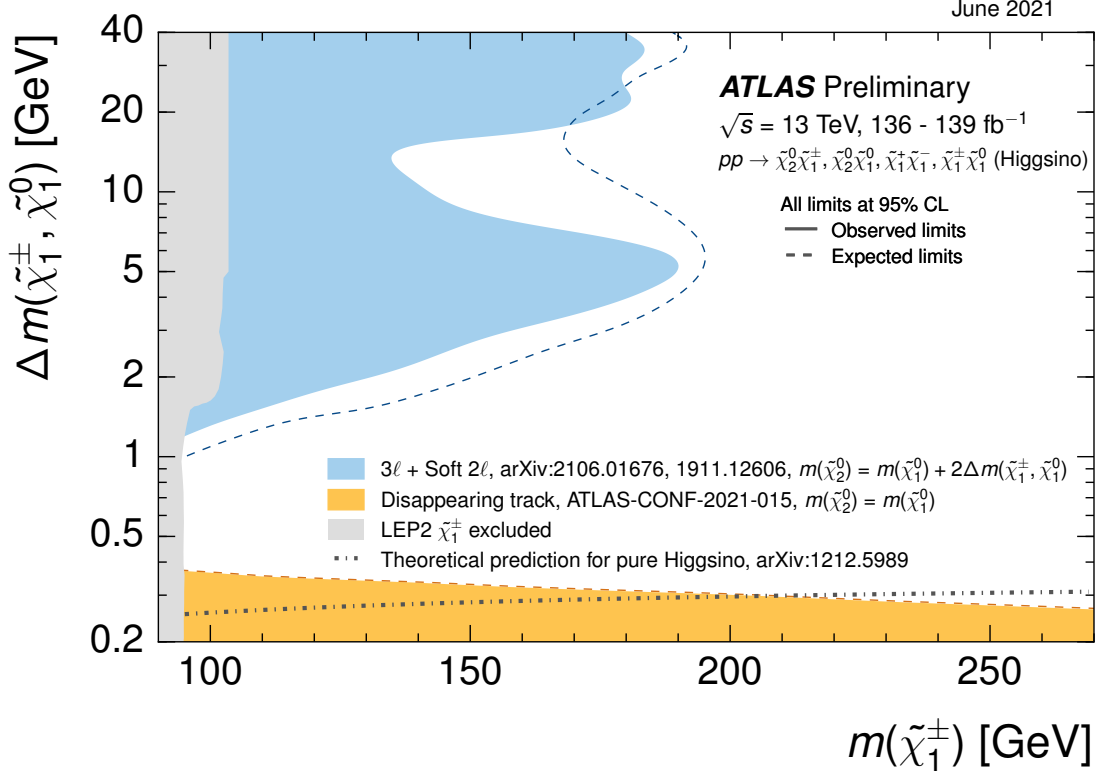
Figure 3.4: ATLAS Exclusion limits at 95% CL for higgsino pair production with off-shell SM-boson-mediated decays to the lightest neutralino ($\tilde{\chi}_1^0$) as a function of the chargino mass and the mass difference $\Delta m_{\pm}$ (cf. Equation 3.1). Expected and observed limits form an ATLAS search for higgsinos in the two and tree lepton final state [114, 115] are shown as the blue filled area and the blue dashed line. Exclusion limits from an ATLAS search for disappearing tracks [116] are shown as the orange filled area. The exclusion limits from previous direct searches at LEP2 are shown in grey along with theoretical constraints on the mass difference from calculations at two-loop level as black dashed line [128, 129].
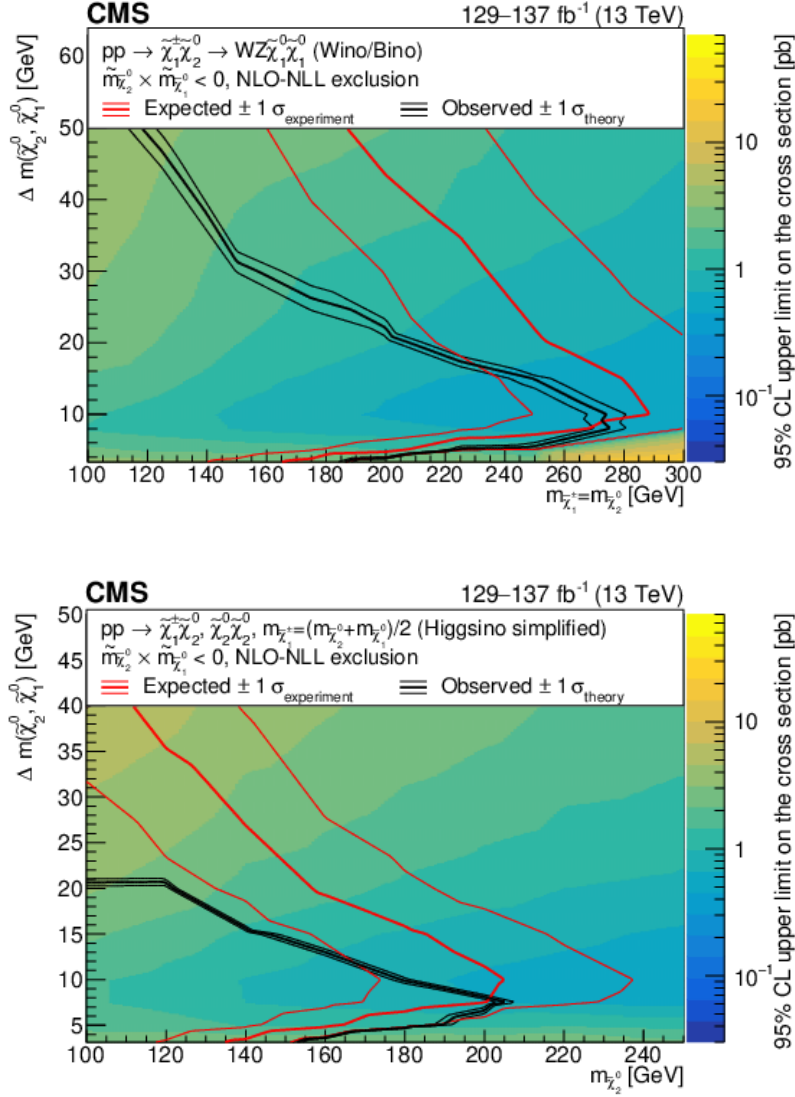
Figure 3.5: Exclusion limits for the production of a wino pair decaying into bino LSPs (top) and in a higgsino simplified model (bottom) from the CMS SOS analysis of final states with two or three soft leptons. The observed 95% CL exclusion contours (black curves) assuming cross sections at NLO+NLL precision are given with the variations (thin lines) corresponding to the uncertainty in the cross section for the simplified signal models. The red curves indicate the 95% CL expected limits with the band (thin lines) covering 68% of the limits in the absence of signal. The range of luminosities of the analysis regions included in the fit is indicated on the plot [121].

pearing tracks. The region $1 \lesssim \Delta m_0 \lesssim 3$ GeV is targeted, which remains unconstrained by the previous searches, especially the Run 2 CMS and ATLAS analyses.
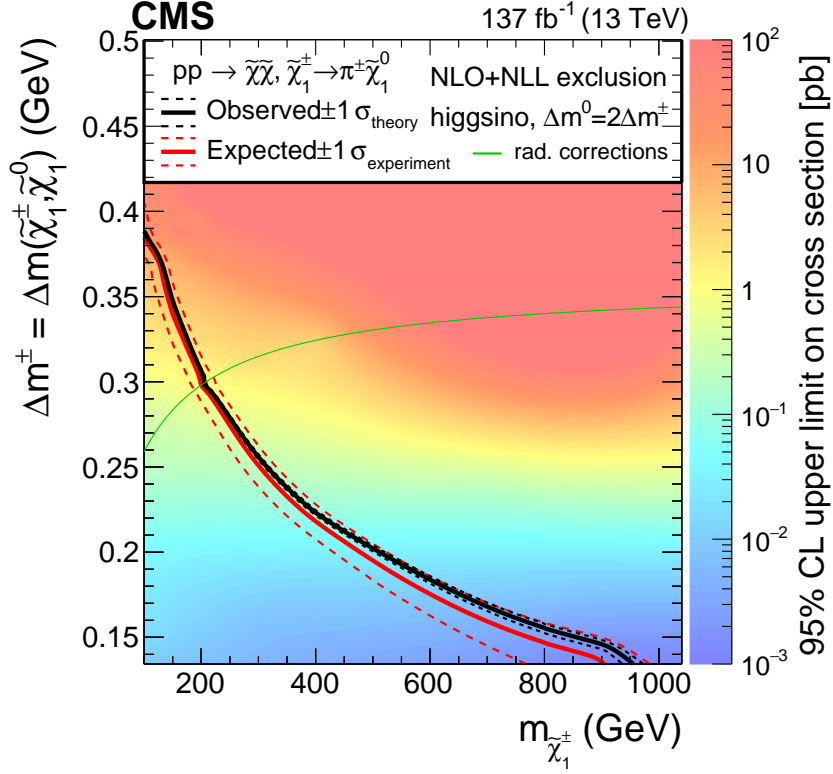
Figure 3.6: Limits on the electroweakino production cross section at 95% CL for a simplified model featuring a nearly-pure higgsino DM candidate. The observed limits are shown as a function of the mass splitting between the lightest electroweakinos and the chargino mass as the black line with the respective uncertainties as dashed line from a search for disappearing tracks with the CMS experiment. The red solid line indicates the boundary where the upper limit is equal to the cross section of fully degenerate higgsino production with the respective uncertainties as dashed lines. The green line represents the set of model points corresponding to a pure higgsino model where only radiative corrections to the mass splitting are assumed [118].

3.3 Simulated Data Sets

This section presents information on the data from simulation and the collected collision data employed in the analysis. Monte Carlo (MC) simulation is utilized for the estimation of the signal yields in the signal region, and for a closure test of the background method. The MC is also employed to train a multivariate classifier that selects signal-like displaced vertices while rejecting SM backgrounds.

3.3.1 Simulated Signal Models

MC techniques involve generating a large number of random inputs or parameters to model, in this case, high-energy proton-proton collision processes. Based on the choice of the generator, the generation of the primary hard process, and subsequent steps like parton showering and hadronization can be included. The term hard process signifies the initial high-energy collision between partons. A parton shower generator seeks to simulate the surrounding underlying event and additional radiation effects. The simulation outputs are subsequently processed by a simulation of the response of the detector. More specific information on data simulation is given in the following, first for signal model samples, followed by simulated SM data.

Signal events are generated using the PYTHIA8 [130] event generator at LO to simulate the signal processes including the complete final state of the collision, the hadronization, parton showers, and the underlying event taking into account the parton distribution function. All production processes are generated simultaneously using the PYTHIA option for inclusive production.

The CMS detector simulation employs the GEANT4 [131] toolkit, which is integrated into the CMS software (CMSSW). It simulates the interaction of particles with matter, accommodating complex geometries. This encompasses electromagnetic, hadronic, and optical processes, with diverse materials influencing stochastic parameters for the simulation. The CMS detector response simulation can be conducted through either a full simulation or including only a part of the full simulation approach, e.g., in the CMS fast detector simulation program, FASTSIM [132]. FASTSIM provides a notable advantage in terms of computational efficiency, reducing the computing time by approximately a factor of 20. This gain is achieved by utilizing a simplified material geometry and deriving parameterized responses for simulated particles. To save execution time, a fast tracking is employed. As a result, there are no fake hits and fake tracks in events generated with FASTSIM. For this analysis, generated signal events are processed through FASTSIM.

To enhance statistical precision while keeping the computing demands constant, only the subset of events that meet the generator-level event filter criterion $H_T > 180$ GeV has been simulated, where H_T is computed as the scalar sum of the p_T of generator-level AK4-jets with $p_T > 30$ GeV and $|\eta| < 5.0$. The total signal cross section is weighted to account for the filter efficiency which is 93%.

The production cross sections (σ) are computed at NLO plus next-to-leading-log (NLL)

precision and in a limit of mass-degenerate higgsino (wino) with all the other sparticles assumed to be heavy and decoupled. The production cross sections thus depend only on the LSP mass. The cross sections are calculated for fixed masses and then interpolated. The interpolated cross sections for pure higgsino-like electroweakino production and the wino-like chargino-neutralino production for the considered neutralino masses are shown in Figures 3.7 and 3.8 [122, 123].
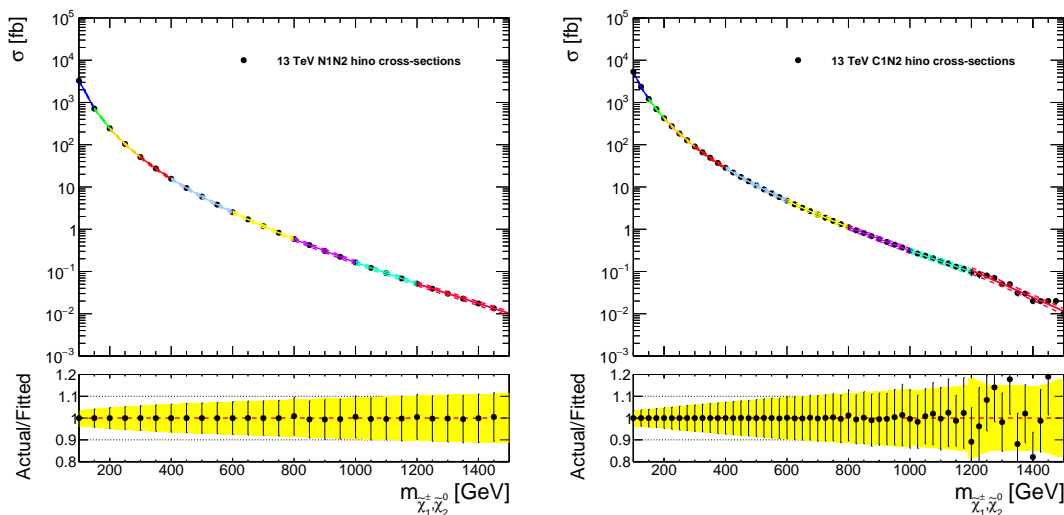

Figure 3.7: Interpolated cross sections for pure higgsino-like neutralino-neutralino (left) and neutralino-chargino (right) pair production as a function of the degenerate mass, assuming fully degenerate mass $m_{\tilde{\chi}}$. Cross sections have been calculated for $\sqrt{s} = 13$ TeV at NLO-NLL [122, 123].

As discussed before in Section 3.1, the free parameters of the compressed higgsino simplified model are the mass of the LSP ($\tilde{\chi}_1^0$) and the mass difference to the LSP. The lifetimes of the neutralinos are determined from phase space using the spectrum generator package SUSYHIT [133]. A grid mass scan is performed over the model parameter, where for each model point, 500×10^3 events have been generated in the grid represented in Figure 3.9. The bino-wino-coannihilation simplified model has an additional free parameter, which is the proper decay length. For the simulation of the bino-wino-coannihilation simplified model, a $\tilde{\chi}_2^0$ mass of 115 GeV is studied, and different Δm_0 are scanned (cf. Figure 3.10) for proper decay lengths of $c\tau = (1, 3, 5)$ mm. For each combination of $\Delta m_0 < 1$ GeV and $c\tau$, 500×10^3 events have been generated, and for each combination of $\Delta m_0 \geq 1$ GeV and $c\tau$, 2×10^6 events have been generated.
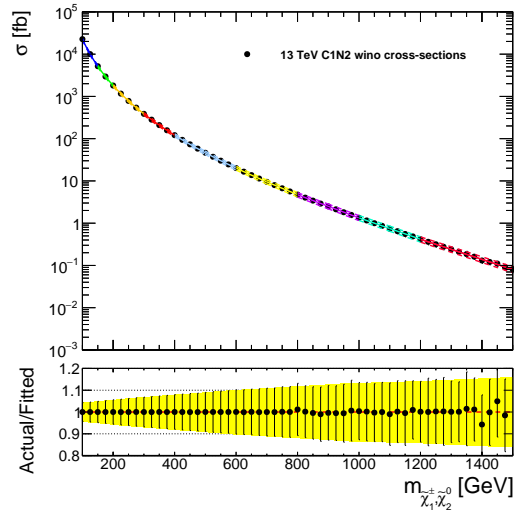
Figure 3.8: Interpolated cross sections for wino-like neutralino-chargino pair production as a function of the degenerate mass $m_{\tilde{\chi}}$. Cross sections have been calculated for $\sqrt{s} = 13$ TeV at NLO-NLL [122, 123].
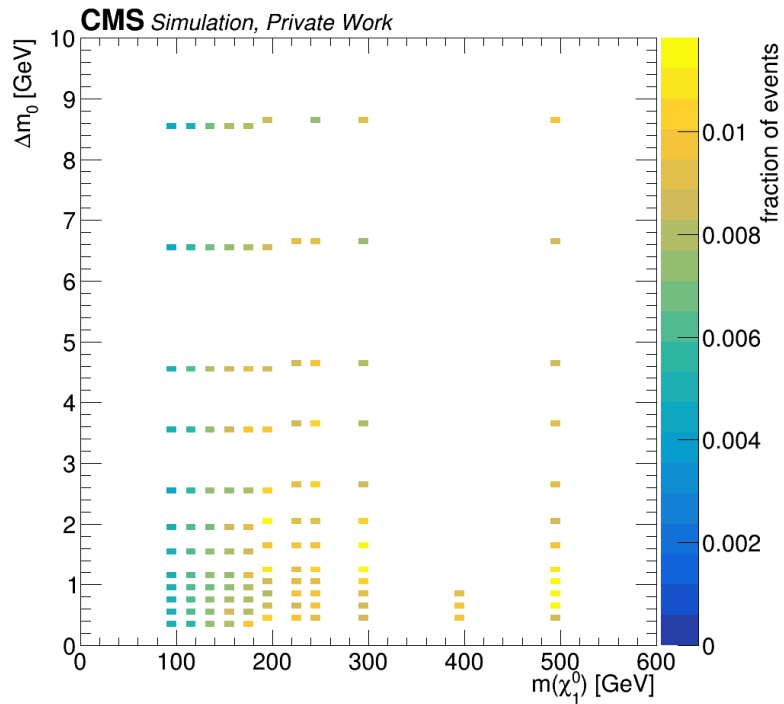
Figure 3.9: Distribution of signal model points in the compressed higgsino simplified model chosen for simulation after generator-level event filters.

76
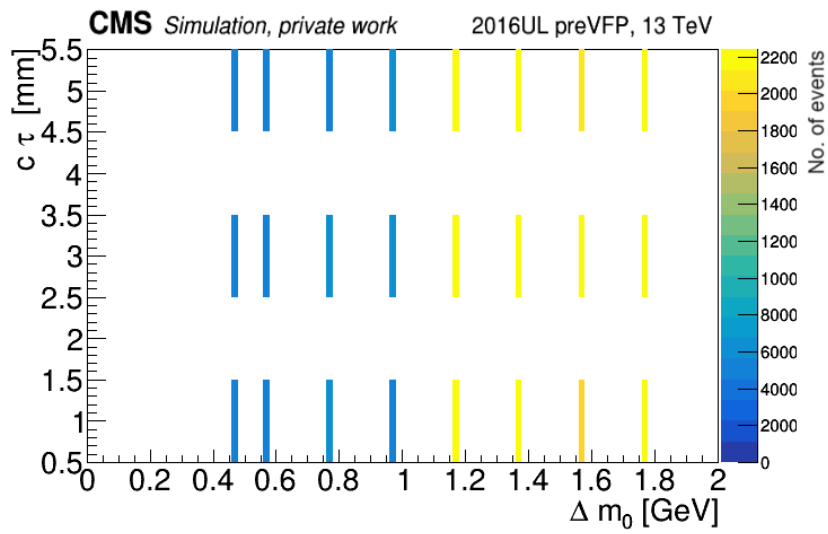
Figure 3.10: Distribution of signal model points in the bino-wino-coannihilation simplified model chosen for simulation after generator-level event filters. A $\tilde{\chi}_2^0$ mass of 115 GeV is studied, and different Δm_0 are scanned for proper decay lengths of $c\tau = (1, 3, 5)$ mm.

3.3.2 Standard Model Background

The simulation of SM events is used for the evaluation of the multivariate classifier, to estimate the significance of the analysis, and perform closure tests, as well as to aid in understanding various aspects of the analysis. The SM processes were simulated using MADGRAPH5 aMC@NLO and PYTHIA8. MADGRAPH5 aMC@NLO [134] is used for the calculation of the hard process. In general, the framework is capable of simulating both SM and BSM processes. QCD corrections to SM processes can be determined with NLO accuracy. PYTHIA8 is used for the simulation of the hadronization and showering. The SM samples use the full CMS detector simulation, which is performed using the GEANT4 toolkit.

To improve the description of 2016 data in the period affected by a saturation issue in the pre-amplifier of the APV25 readout chip (cf. below, Section 3.4) [135], around half of the MC events generated for the 2016 Run 2 ultra legacy campaign underwent a dedicated simulation of the APV25 chip dynamic gain in the strip tracker partitions. A set of APV baseline distributions, which represent the charge accumulated on a strip over several bunch crossings, are provided as an input, separately per layer, and in bins of PU and z within a layer. Subsequently, each time a charge is deposited on a strip, the APV response is simulated. This is linear for low APV baselines (small amount of charge from previous interactions remaining on strips) but becomes non-linear for high APV baselines. As a result, the charge effectively deposited and read out from a strip is reduced. SM MC datasets that match the different conditions during the APV saturation issue in data taken in early 2016 have been employed in the thesis.

Table 3.3.2 shows the SM MC data sets with the respective data set paths, along with the cross section and resulting luminosity used in this analysis.

2016 data set name	σ[pb]	L[fb^{-1}]
WJetsToLNu_HT-100To200_TuneCP5_13TeV-madgraphMLM-pythia8	1256.00	17.39
WJetsToLNu_HT-200To400_TuneCP5_13TeV-madgraphMLM-pythia8	335.50	53.79
WJetsToLNu_HT-400To600_TuneCP5_13TeV-madgraphMLM-pythia8	45.25	55.97
WJetsToLNu_HT-600To800_TuneCP5_13TeV-madgraphMLM-pythia8	10.97	220.11
WJetsToLNu_HT-800To1200_TuneCP5_13TeV-madgraphMLM-pythia8	4.93	508.92
WJetsToLNu_HT-1200To2500_TuneCP5_13TeV-madgraphMLM-pythia8	1.16	1827.56
WJetsToLNu_HT-2500ToInf_TuneCP5_13TeV-madgraphMLM-pythia8	8.00	487.60
TTJets_SingleLeptFromT_TuneCP5_13TeV-madgraphMLM-pythia8	109.60	276.26
TTJets_SingleLeptFromTbar_TuneCP5_13TeV-madgraphMLM-pythia8	108.70	270.22
TTJets_DiLept_TuneCP5_13TeV-madgraphMLM-pythia8	54.17	269.28
ZJetsToNuNu_HT-100To200_TuneCP5_13TeV-madgraph-pythia8	264.30	29.54
ZJetsToNuNu_HT-200To400_TuneCP5_13TeV-madgraph-pythia8	72.43	104.46
ZJetsToNuNu_HT-400To600_TuneCP5_13TeV-madgraph-pythia8	9.93	681.83
ZJetsToNuNu_HT-600To800_TuneCP5_13TeV-madgraph-pythia8	2.38	879.21
ZJetsToNuNu_HT-800To1200_TuneCP5_13TeV-madgraph-pythia8	1.07	656.08
ZJetsToNuNu_HT-1200To2500_TuneCP5_13TeV-madgraph-pythia8	0.25	549.97
ZJetsToNuNu_HT-2500ToInf_TuneCP5_13TeV-madgraph-pythia8	5.60	20.02
DYJetsToLL_M-50_Zpt-200toInf_BPSFilter_TuneCP5_13TeV -madgraphMLM-pythia8	108.33	91.17

Table 3.1: Simulated SM samples used in the analysis (2016 MC). The cross sections are calculated to NNLO.

2016 data set name	$L[\text{fb}^{-1}]$
MET B_ver1_HIPM	}5.83
MET B_ver2_HIPM	
MET C_HIPM	2.60
MET D_HIPM	4.29
MET E_HIPM	4.08
MET F_HIPM	}3.15
MET F	
MET G	7.66
MET H	8.75
Total	36.36

Table 3.2: Table of collision datasets with integrated luminosity values used in the analysis. The data were recorded by CMS during 2016 Run 2 data-taking.

3.4 Collision Data

For this analysis data recorded by CMS during Run 2 in 2016 with a center-of-mass energy of $\sqrt{s} = 13$ TeV is analyzed. The ultra legacy version of data reconstruction from *21Feb2020* is used. The term ultra legacy refers to several updates to the re-processing of Run 2 data that were implemented during the 1-year delay in the long shutdown as a response to the COVID-19 pandemic. Of most importance for this analysis is perhaps the precision of the tracker alignment calibration, which corresponds to the ultimate accuracy achieved (cf. Section 2.3.1). The ultra legacy data reconstruction also includes many more improvements to calibration and reconstruction not related to the tracker, such as ECAL calibrations [136].

As introduced in Section 2.1.1, the amount of data collected during data-taking is measured in terms of the integrated luminosity. Table 3.4 lists the (integrated) luminosity for the data sets used, split up by data-taking periods. The data set is measured to have a luminosity of 36.36 fb^{-1} using the BRIL WORK SUIT [137].

Strip Preamplifier Saturation

As previously mentioned (cf. Section 3.3.2), in the later months of 2015 and the early months of 2016, the silicon strip tracker encountered a notable decline in the signal-to-noise ratio, coupled with a reduction in the recorded hits on tracks. This resulted in a reduced hit efficiency in the silicon strip detector, as can be seen in Figure 3.11. The hit efficiency is the averaged probability to find a cluster in a given silicon sensor that has been traversed by a charged particle. The phenomenon was linked to saturation effects occurring in the pre-amplifier of the APV25 readout chips. The drain speed of the preamplifier was affected more strongly by the change in operating temperature than anticipated, leading to a slower discharge of the amplifier under high occupancy

conditions. During the period characterized by this issue, approximately 20 fb^{-1} of data from 2016 were impacted. To expedite recovery, modifications were made to the drain speed. These adjustments allowed for more rapid recuperation. With the implementation of the novel APV pre-amplifier settings, the hit efficiency rebounded to the same level as observed in Run 1. Subsequently, 16 fb^{-1} of 2016 data were collected using these updated settings.
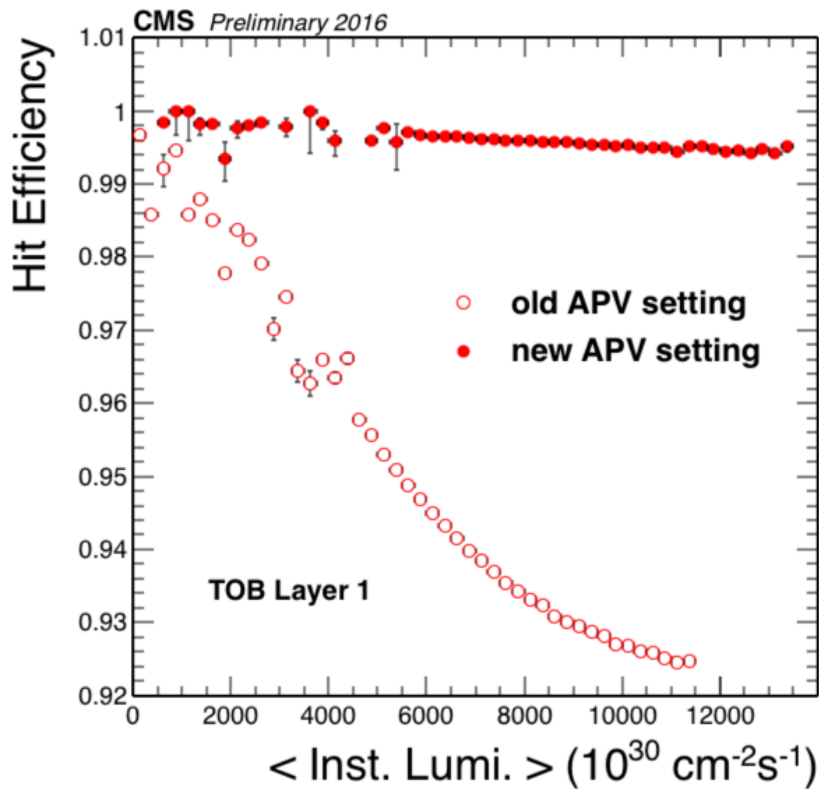

Figure 3.11: Hit efficiency of the silicon strip detector during 2016 Run 2 data-taking as a function of the instantaneous luminosity. The averaged probability to find a cluster in a given silicon sensor that has been traversed by a charged particle is measured using tracks that have a minimum of eight hits in the pixel and strip detectors in events with less than 100 tracks. Only tracks that fall within the respective sensor acceptance are used. Bonding region for modules with two sensors, and modules that are knowingly malfunctioning are excluded from the efficiency measurement [138].

3.5 Signal Characteristics

In this search, the DM candidate is the LSP and assumed to be a neutralino $\tilde{\chi}_1^0$. It originates from the pair production of a $\tilde{\chi}_2^0$ together with another neutralino or chargino and the leptonic decay $\tilde{\chi}_2^0 \to Z^* \tilde{\chi}_1^0$, with $Z^* \to \mu\mu$. The search is focused on investigating

final states characterized by the presence of two displaced muons with low momentum, and opposite charges. A representative signal event is shown in Figure 3.12. The event display highlights distinctive features of the signal process, including a considerable transverse momentum imbalance, an $\vec{p}_T^{\mathrm{miss}}$ component opposing a high-p_T initial-state radiation (ISR) jet. As the $\tilde{\chi}_1^0$ does not interact with the detector, its kinematics can only be inferred based on the $\vec{p}_T^{\mathrm{miss}}$. An ISR jet is created when one of the incoming protons emits radiation (such as a quark or a gluon) before the interaction. The requirement of a high-p_T jet in the event selection serves a dual purpose. First, it is required in order to induce enough $|\vec{p}_T^{\mathrm{miss}}|$ to satisfy the trigger. Second, it contributes to amplifying the event's characteristics. Due to R-parity conservation, signal events contain two massive electroweakinos in the final state, which are usually produced back-to-back. If a jet with sufficiently high p_T is emitted, the remainder of the interaction recoils against the jet and imparts momentum onto the system of invisible particles in the opposite direction. This way, the ISR jet leads to a more probable scenario wherein the two electroweakinos produced, tend to decay within the same detector hemisphere, or relatively collimated. The boosted neutralinos give rise to higher $|\vec{p}_T^{\mathrm{miss}}|$, such that in signal evens with a high-momentum ISR jet, a considerable magnitude of $|\vec{p}_T^{\mathrm{miss}}|$ is expected.

As a result, the baseline event selection correspond to those of a monojet analysis. The latest CMS monojet analysis [120] establishes that the dominant background processes are $Z \to \nu\nu$ and $W \to l\nu+$ jets. This is expected to be the case for the presented search since the baseline selection is largely synchronized with the CMS monojet search. Subleading backgrounds are DY, top quark, and QCD processes (cf. Section 3.7.1).

A key challenge in this analysis is the identification of the signal muons. As the two neutralinos are nearly mass degenerate and the mass difference Δm_0 determines the momentum-sum of the two muons, these are low-momentum muons that often fail standard muon identification (cf. Figure 3.1). Consequently, these muons are usually reconstructed just as a track but not as an identified PF muon. Selecting the tracks of these two muons (marked in red in the event display in Figure 3.12) among the hundreds of low-momentum tracks from the hard scattering primary vertex, from PU, and the underlying event is a difficult task that necessitates dedicated reconstruction techniques, such as the SV-building method introduced in Section 2.3.2.1.

To summarize, the fundamental challenge of the targeted signal signature lies in utilizing the unique characteristics inherent to the signal process to distinguish it from the SM background. The following sections will describe the strategies employed to address this challenge.

3.5.1 Kinematic Distributions

In this section, the distinct signal features discussed above are illustrated with generator-level distributions - that is, distributions of observables defined at the level of the signal event generation. These distributions are not affected by detector or reconstruction features. Studying these distributions aids in examining the influence of different simplified
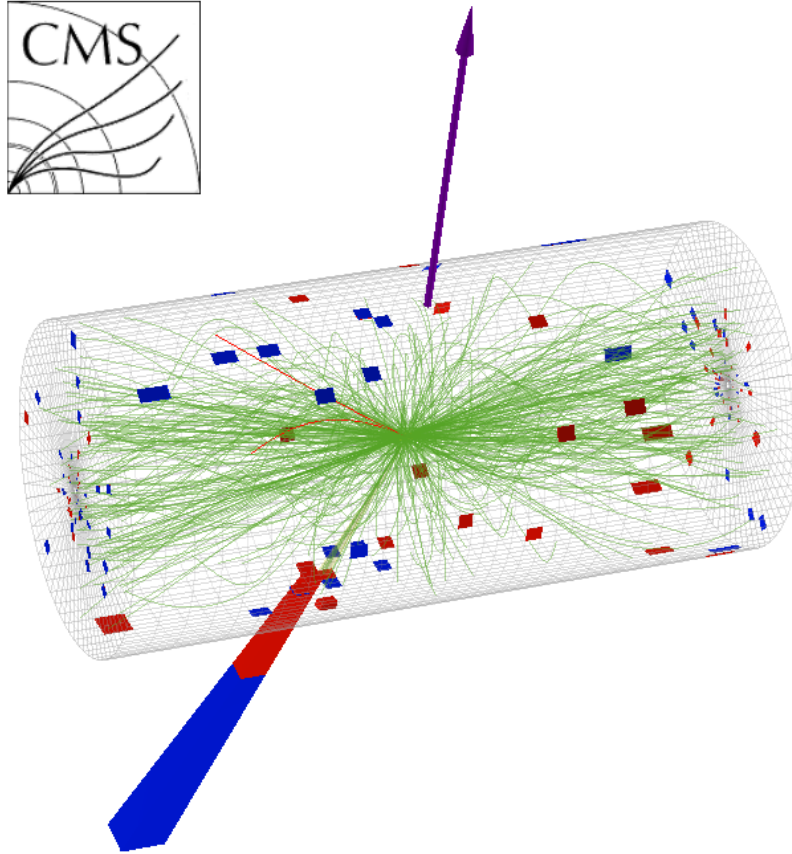
Figure 3.12: 3D Event display featuring the production and decay $\tilde{\chi}_2^0 \to \tilde{\chi}_1^0 \, \mu\mu$ in the CMS Phase-0 detector. The $\tilde{\chi}_1^0$ and $\tilde{\chi}_2^0$ manifest as a large amount of $|\vec{p}_T^{\,\mathrm{miss}}|$ recoiling against the ISR jet. The $\vec{p}_T^{\,\mathrm{miss}}$ is given by the purple arrow. The ISR jet is visible as by the HCAL and ECAL deposits (red and blue towers). The moun-pair tracks from the signal process are marked in red among all tracks (green) in the event. Simulated event, displayed with the CMS Event Visualization Environment [139].
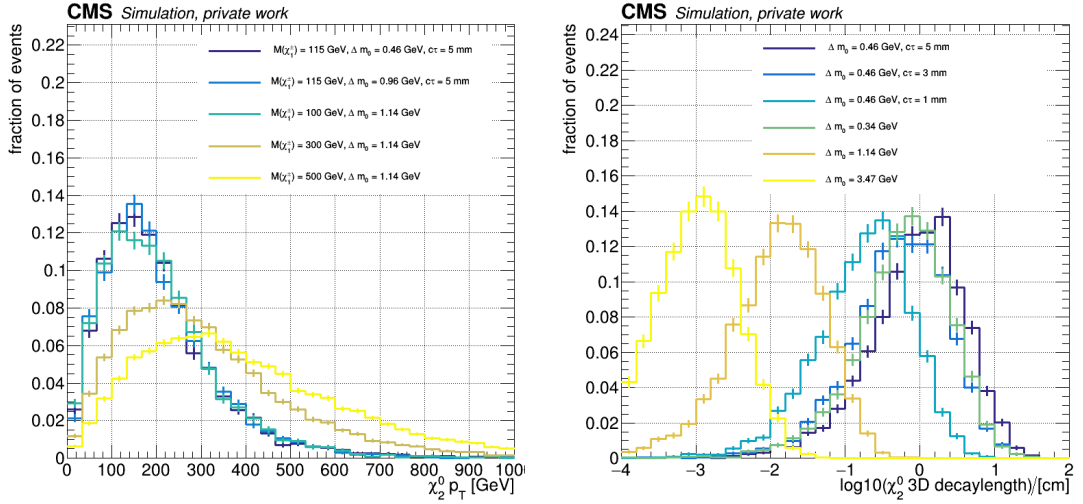
Figure 3.13: Signal $\tilde{\chi}_2^0$ distributions of the transverse momentum (left) and 3D decay length (right) at generator level. Shown are example model points from the bino-wino-coannihilation simplified model and the compressed higgsino simplified model. The mass of the $\tilde{\chi}_2^0$ is 115 GeV for all model points displayed in the right plot.

model parameters on the signal kinematics. In the case of the bin-wino coannihilation model, the mass $M(\tilde{\chi}_2^0) = M(\tilde{\chi}_1^\pm)$ is fixed to 115 GeV, while Δm_0 and $c\tau$ are free parameters. In the case of the compressed higgsino model however, the proper lifetime is a result of the model parameters, and Δm_0 as well as $M(\tilde{\chi}_2^0)$ are free parameters. Correlations between the neutralino lifetime and object kinematics are important for the analysis strategy.

As depicted in Figure 3.13, the transverse momentum of the $\tilde{\chi}_2^0$ is significantly influenced by the mass $M(\tilde{\chi}_2^0)$. The momentum is almost entirely transferred to the nearly equally heavy LSP in the decay process. The transverse momentum (p_T) of the signal leptons is thus mainly determined by the mass difference of the neutralinos, as shown in Figure 3.14. The muon reconstruction efficiency sharply rises with the momentum of the track, reaching an efficiency peak exceeding 90% for prompt muons with $p_T > 3$ GeV (cf. Figure 2.9). Likewise, the track reconstruction efficiency reaches its maximum for prompt tracks with a $p_T > 3$ GeV (cf. Figure 2.6). Larger Δm_0 values result in higher lepton momenta and more efficient track reconstruction.

In contrast to the p_T distribution, the $|\eta|$ distribution of the signal leptons is largely unrelated to the free parameters of the models, as visible in Figure 3.15. Given that the soft muon pair from the signal decay will be identified based on its tracks, only decays where both muons are within the tracker acceptance of $|\eta| < 2.5$ can be reconstructed. This leads to a signal efficiency loss of up to 8%. A substantial portion of signal events extend beyond the barrel region and into the tracker's endcap region. The efficiency
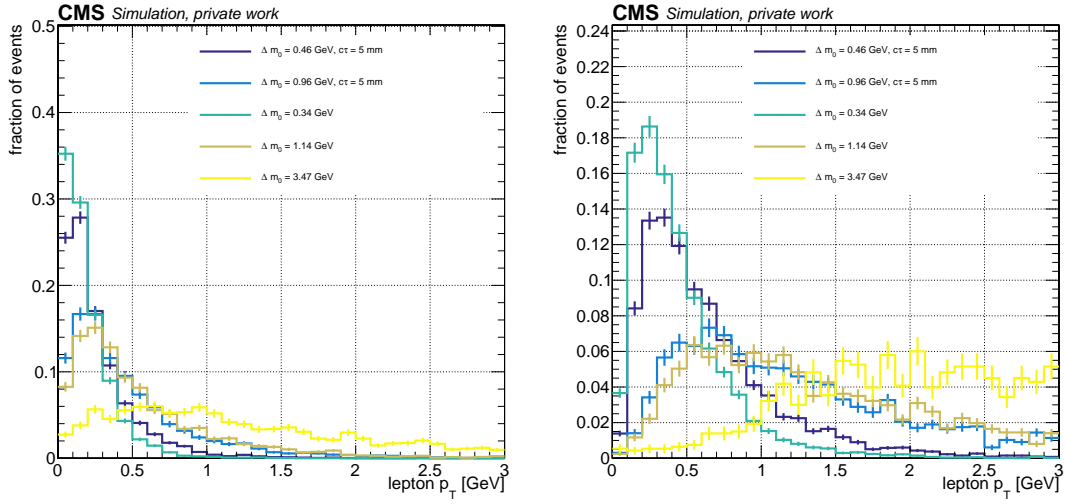
Figure 3.14: Transverse momentum distribution of the lower-p_T (left) and higher-p_T (right) lepton at generator level in signal events with an OS same-flavor signal lepton pair. Shown are example model points from the bino-wino-coannihilation simplified model and the compressed higgsino simplified model in different colors.

and identification for low-momentum muons is higher in the endcaps compared with the barrel region, as evident from Figure 2.9. Thus, this analysis profits from the large muon reconstruction efficiency in the endcaps at low p_T.
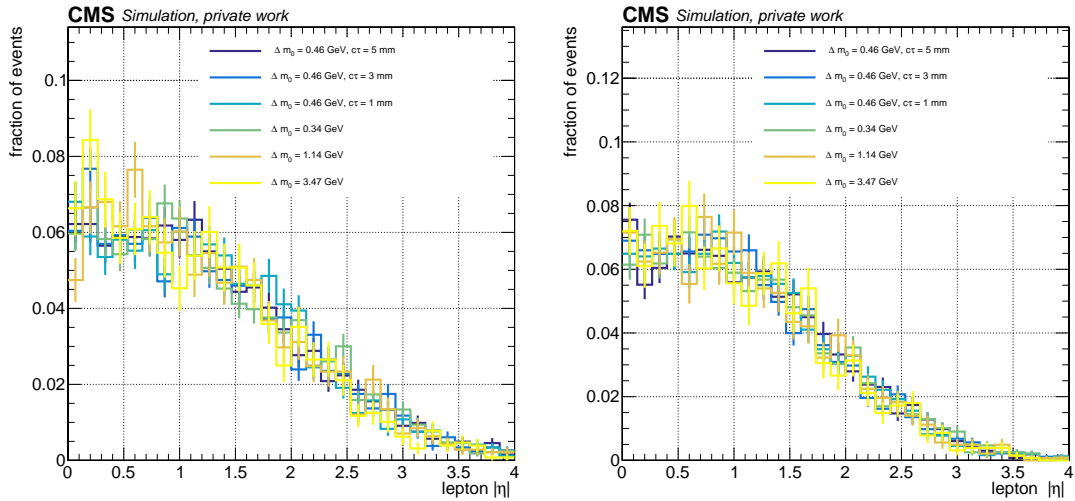
Figure 3.15: Signal lepton $|\eta|$ distribution of the lower-p_T (left) and higher-p_T lepton at generator level in a OS signal muon pair. Shown are example model points from the bino-wino-coannihilation simplified model and the compressed higgsino simplified model.

85

In this analysis, the pairing of tracks and the construction of secondary decay vertices (SVs) serve as powerful tools to identify signal tracks from the multitude of tracks present in each event. The efficiency of the SV building is dominated by the decay length of the $\tilde{\chi}_2^0$, which corresponds to the displacement of the lepton-pair vertex from the primary interaction vertex. To ensure successful reconstruction, this SV must be distinguishable from the PV and separable from PU vertices. Figure 3.13 reveals two distinct behaviors for the two simplified models. In the bino-wino-coannihilation simplified model, the proper lifetime of the $\tilde{\chi}_2^0$ is a model parameter. Examination of all signal model points showed that approx. 98% of the $\tilde{\chi}_2^0$ have a 3D decay length above 100 μm (cf. Figure 3.13), similar to the longitudinal resolution of the vertex reconstruction with the Kalman Vertex Finder in CMS for vertices with two tracks (cf. Figure 2.7).

In the compressed higgsino model, the $\tilde{\chi}_2^0$ decay length is primarily influenced by the mass difference of the neutralinos. According to Fermi's golden rule (cf. Equation 1.30), a larger mass difference translates into a larger phase space for decays, resulting in a more prompt decay on average. In contrast to the relationship between momentum and the mass difference (Δm_0), larger Δm_0 values lead to shorter mean decay lengths of the $\tilde{\chi}_2^0$, making SV reconstruction more challenging. In summary, the neutralino mass difference introduces two opposing effects that impact both the lepton's momentum and the $\tilde{\chi}_2^0$ decay length, leading to a trade-off in terms of signal sensitivity.

3.6 Event Selection

A flowchart of the main selection steps in this analysis is given in Figure 3.16. The signal characteristics as described in the previous section help to define the event selection in four major steps. The $|\vec{p}_T^{\text{miss}}|$ and H_T^{miss} trigger to make use of the invisibly escaping neutralinos. A monojet event selection requiring an ISR jet to boost the respective electroweakinos. The selection of a pair of soft and displaced muons in an event. And the application of a multivariate event classifier.

At the heart of this selection chain is the identification of the soft, displaced signal muon pair within a candidate event. This task is subdivided into three selection steps on object level, which are: the selection of tracks, the selection of track pairs, and the selection of SVs. To obtain the SVs, the V0 Fitter (cf. Section 2.3.2.1) is employed to build collections of candidate vertices which are later selected from using machine learned methods. The various steps of the selection chain are described in more detail in the following sections.

3.6.1 Trigger

In the initial stage of the event selection process, events within the data set that pass both the L1 and HLT are selected. A combination of $|\vec{p}_T^{\text{miss}}|$ and H_T^{miss} trigger paths is used, selecting events with a trigger turn-on of $|\vec{p}_T^{\text{miss}}|$, $H_T^{\text{miss}} > (90, 100, 110, 120)$ GeV. The use of different trigger paths compensates for potential losses in efficiency from lower
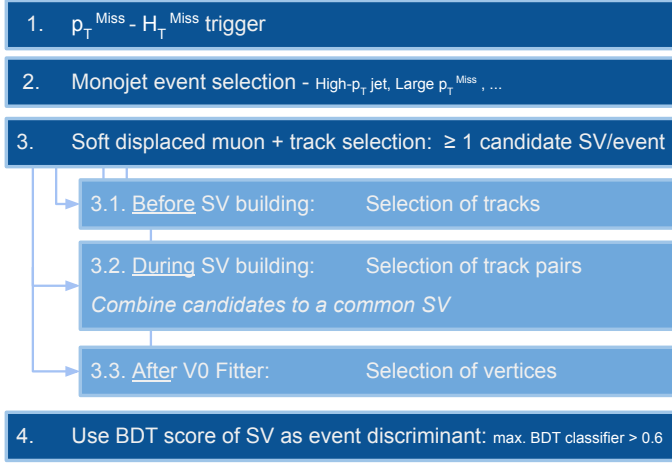
1. p_T^{Miss} - H_T^{Miss} trigger

2. Monojet event selection - High-p_T jet, Large p_T^{Miss}, ...

3. Soft displaced muon + track selection: ≥ 1 candidate SV/event

   3.1. _Before_ SV building: Selection of tracks

   3.2. _During_ SV building: Selection of track pairs
   Combine candidates to a common SV

   3.3. _After_ V0 Fitter: Selection of vertices

4. Use BDT score of SV as event discriminant: max. BDT classifier > 0.6

Figure 3.16: Overview over the different selection steps applied in the analysis. The arrows indicate selection processes on object level (light blue) that are needed for the overall event selection (dark blue).

trigger thresholds, due to prescaling during periods of higher instantaneous luminosity. Events are selected in data if at least one of the triggers fires.

The efficiency of the trigger selection is measured and applied to simulated data via event weights. To quantify this efficiency, the fraction of events meeting the trigger criteria to the overall number of events in a reference sample is calculated as a function of the offline $|\vec{p}_T^{\text{miss}}|$. Importantly, this evaluation is conducted within a reference sample that is distinct from the trigger under scrutiny, ensuring an orthogonal set of selection for the reference and measurement triggers. In this case, a single-electron dataset was chosen as a reference sample. Single-electron events are selected by requiring at least one single-electron trigger be fired, with an online threshold on the transverse momentum of the electron $p_T^e > (27, 32, 35)$ GeV and an offline electron reconstructed and identified with a tight working point. As previously described for the combination of $|\vec{p}_T^{\text{miss}}|$ and H_T^{miss} trigger paths, different trigger turn-on values of p_T^e are considered to compensate for efficiency losses due to pre-scaled trigger thresholds. The trigger efficiency, as illustrated in Figure 3.17, is presented as a function of both jet multiplicity and offline H_T^{miss} and subject to baseline selection criteria of $H_T > 150$ GeV and a requirement of $N_{\text{jet}} \geq 1$. This figure demonstrates that the trigger exhibits efficiency levels exceeding 95% for $|\vec{p}_T^{\text{miss}}|$ values surpassing 250 GeV, and nearly 100% for $|\vec{p}_T^{\text{miss}}| > 300$ GeV. Inefficiencies, reaching up to 15%, are observed in the lowest jet multiplicity categories.
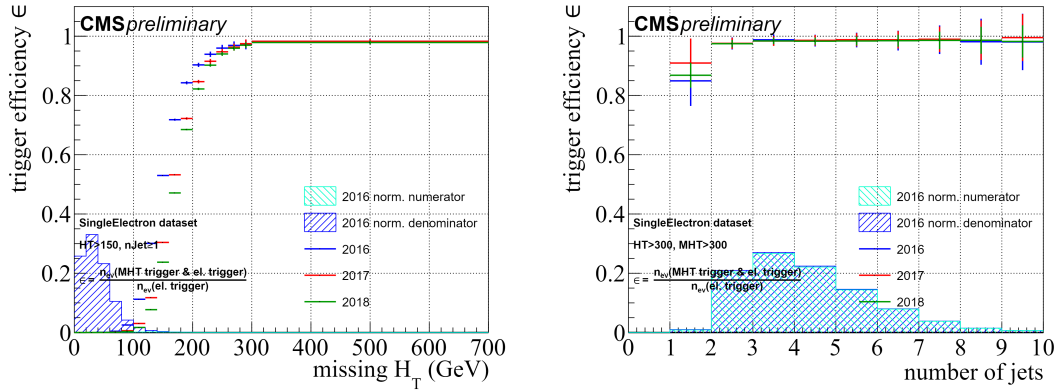
Figure 3.17: Efficiency of the set of $|\vec{p}_T^{\mathrm{miss}}|$-MHT cross triggers with $|\vec{p}_T^{\mathrm{miss}}|$, $H_T^{\mathrm{miss}} >$ $(90, 100, 110, 120)$ GeV, measured in a single-electron control region, shown for H_T^{miss} (left) and number of jets (right). The jet multiplicity is shown for $H_T^{\mathrm{miss}} > 300$ GeV to account for the trigger turn-on. The efficiency is given for the years 2016 (blue), and 2017 (red) as well as 2018 (green) for comparison. The distributions of the normalized number of events that pass the electron trigger and the $|\vec{p}_T^{\mathrm{miss}}|$-$H_T^{\mathrm{miss}}$ cross triggers is the numerator for the efficiency (light-blue dashed area). The distributions of the normalized number of events that pass the electron trigger is the denominator for the efficiency (dark-blue dashed area) [118].

3.6.2 Monojet Selection

The monojet event selection is applied to all events before building the SVs. While the subsequent selection steps are designed to specifically select the muonic decay of the $\tilde{\chi}_2^0$, this part of the selection chain aims to select events with the desired overall event topology described above, i.e., a high momentum ISR jet opposing a large $\vec{p}_T^{\mathrm{miss}}$. The criteria used to select signal region events are similar to those in the latest CMS monojet analysis [120]. The selection criteria are listed in Table 3.6.2.

In the offline selection, the requirement $|\vec{p}_T^{\mathrm{miss}}| > 250$ GeV is applied. In this regime, the trigger efficiency is found to be larger than 95% (cf. Section 3.6.1). Furthermore, a leading jet with $p_T > 100$ GeV and $|\eta| < 2.4$ is required. This ISR jet gives a boost to the system of two neutralinos, thus increasing the missing transverse momentum and thereby the sensitivity of the analysis. All jets in the event selection are required to be ak4-jets (cf. Section 2.4.4). The distributions of the $|\vec{p}_T^{\mathrm{miss}}|$ and the p_T of the leading jet are displayed in Figure 3.18 for a selection of signal model points and SM backgrounds.

Moreover, a veto on events with an isolated electron, muon photon, or tau lepton is applied. The lepton vetos reduce backgrounds from $W \to l\nu$ decays, where the neutrino and a missed lepton can give rise to large amounts of $|\vec{p}_T^{\mathrm{miss}}|$. The PF-based isolation is used where for a given lepton or photon candidate, where the transverse momenta

Variable	Value
$\lvert\vec{p}_T^{\,\mathrm{miss}}\rvert$	> 250 GeV
$N_{\mathrm{jet}}(p_T > 100 \text{ GeV}, \lvert\eta\rvert < 2.4)$	≥ 1
$N_{\mathrm{b\text{-}jet}}(p_T > 30 \text{ GeV}, \lvert\eta\rvert < 2.4)$	$= 0$
$N_{\gamma \text{ iso.}}(p_T > 15 \text{ GeV})$	$= 0$
$N_{e,\mu \text{ iso.}}(p_T > 10 \text{ GeV})$	$= 0$
$N_{\tau \text{ iso.}}(p_T > 18 \text{ GeV})$	$= 0$
$\Delta\phi(\vec{p}_T^{\,\mathrm{miss}}, \vec{\mathrm{jet}}_{1,2,3,4})$	> 0.5

Table 3.3: Selection criteria in the monojet selection step.

of all PF candidates of type charged or neutral hadron are added in a cone around the respective candidate [140]. A lepton (or photon) is considered isolated if the summed transverse momentum found this way is $< 20\%$ of the lepton (photon) momentum.

In addition, b-tagged jets are vetoed since the signal process does not contain b-jets. This veto is efficient in rejecting background from $t\bar{t}$ decays, in which the b quarks arise from a t-quark decay. For this purpose jets potentially originating from b-hadrons or quarks are identified using the DeepCSV b-tagging algorithm using the medium working point (cf. Section 2.4.4).

QCD multijet background arises from the strong force between quarks and gluons in proton collisions and represents a common and challenging source of background. The QCD background is suppressed in the analysis by requiring a large amount of $\lvert\vec{p}_T^{\,\mathrm{miss}}\rvert$, as well as a minimal azimuthal angle between $\vec{p}_T^{\,\mathrm{miss}}$ and the four leading jets with $p_T > 30$ GeV and $\lvert\eta\rvert < 2.5$, $\Delta\phi(\vec{p}_T^{\,\mathrm{miss}}, \vec{\mathrm{jet}}_{1,2,3,4})$, to be larger than 0.5 radians. The requirement of a high-p_T jet in the event leads to a topology where the $\vec{p}_T^{\,\mathrm{miss}}$ points in the opposite direction of the jet for signal events. In QCD events, only little $\lvert\vec{p}_T^{\,\mathrm{miss}}\rvert$ is produced, for example due to jet energy miss-measurements. This results in large values $\Delta\phi(\vec{p}_T^{\,\mathrm{miss}}, \vec{\mathrm{jet}}_1)$, as can be seen in Figure 3.18. This demonstrates the power of the use of the ISR jet in correlation to the $\vec{p}_T^{\,\mathrm{miss}}$ for this kind of analyses.
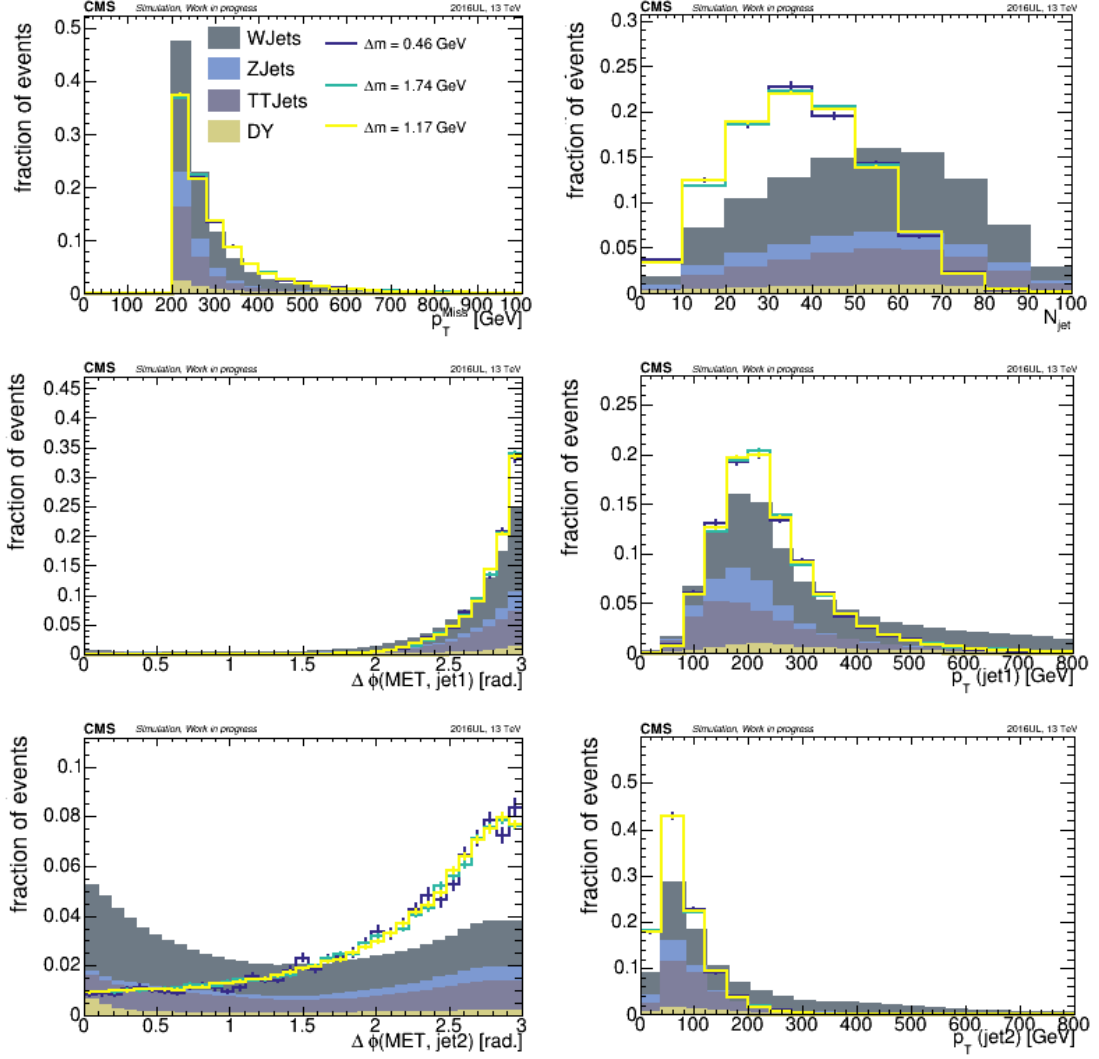
Figure 3.18: Signal and MC background distributions of the number of jets (N_{jet}) and the $|\vec{p}_T^{\text{miss}}|$ (top), as well as the minimal azimuthal angle of the two leading jets with respect to $\vec{p}_T^{\text{miss}}$, $\Delta\phi(\vec{p}_T^{\text{miss}}, \vec{\text{jet}}_{1,2})$ and transverse momentum of the two leading jets ($p_T^{\text{j1,j2}}$) (middle and bottom). A baseline selection of $|\vec{p}_T^{\text{miss}}| > 200$ GeV has been applied in all plots. Events with a $\tilde{\chi}_2^0$ for three signal model points characterized by different Δm_0 are displayed as colored lines. The GEANT4-based simulation of events is shown for the background as colored, filled areas divided into different SM processes.

3.6.3 Soft Displaced Muon Selection

As previously described and depicted in Figure 3.16, the soft displaced muon selection comprises three steps on object level. The three steps of the soft displaced muon se-

90

Variable	Value
Muon type	tracker muon
No. tracker hits	≥ 10
No. pixel layers	> 1
χ^2/Ndof (track fit)	< 2.2
d_{xy}	< 3 cm
d_z	< 20 cm

Table 3.4: Soft muon selection criteria that at least one track in an OS pair of candidate tracks has to fulfill.

lection, the selection of tracks, the selection of track pairs before as well as in the SV building process, and the selection of SVs are detailed in the following.

3.6.3.1 Selection of Tracks

In the first step, candidate tracks that have 180 MeV $< p_T < 15$ GeV and are isolated from jets with a $p_T > 30$ GeV in a cone of 0.4 are selected. The resulting momentum distribution for such pre-selected tracks is given in Figure 3.20. A typical CMS event with the average LHC conditions in terms of the complexity contains around 1000 tracks, where most are low-momentum due to PU and underlying event activity. Thus, it is essential to further reduce the number of possible track-track combinations before and during the SV building process. This is achieved in a second step by a selection on all possible parings.

3.6.3.2 Selection of Track Pairs in the SV Building Process

During the SV building process all possible combinations of OS tracks which satisfy a few criteria are used: first, at least one of the two tracks must be matched to a muon. The matching is done by requiring ΔR between the track and the muon to be less than 0.01. Moreover, the same charge is required of the track and the matching muon. To further identify soft muon tracks, the requirements of the soft muon identification as described in Section 2.4.2 are applied. A list of the selection criteria of the soft muon ID as applied in this search is given in Table 3.4. The requirement on χ^2/Ndof is loosened slightly compared with the value in the CMS soft ID to enhance the signal efficiency. Distributions of observables used in the selection of soft displaced muons and muon-track pairs are given in Figure 3.19. In this case, as for all following Figures, the SVs (tracks) that are matched to the signal process at generator level are referred to as true signal SVs (tracks). In all track pairs, at least one track is required to match a muon, while the soft muon quality criteria are not applied in these distributions. For true signal candidates, the higher-p_T track is matched to a muon in 95% of cases whereas the lower-p_T track is only matched in 20% of cases; in the latter case, often both tracks are muon-matched. Complementary to Figure 3.19, further characteristics of the soft displaced muon in candidate signal and MC background events can be found in the Appendix, Figure A.2.
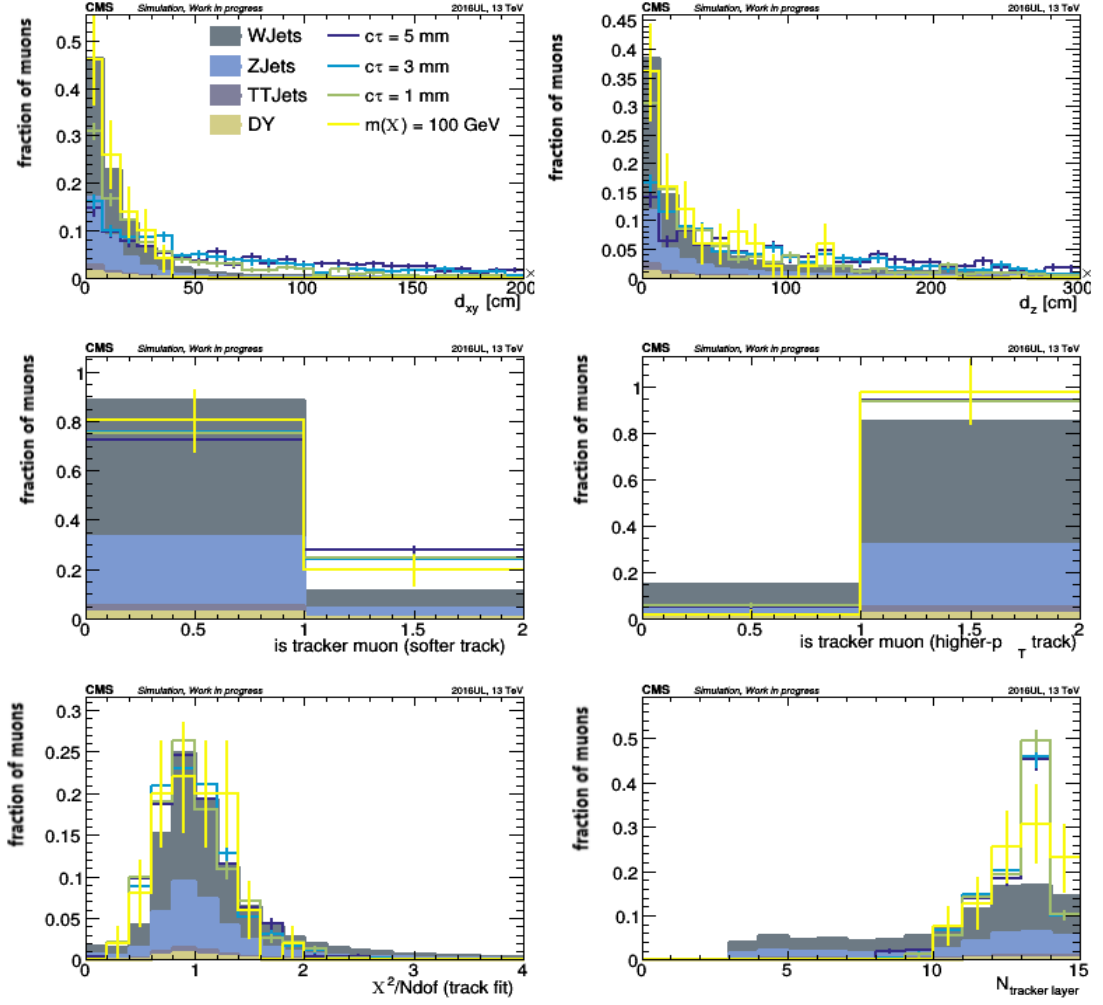
Figure 3.19: Distributions of soft muon selection criteria applied to at least one track in an OS candidate track pair. The distributions are shown for true signal muon-track pairs and reconstructed muon-track pairs from SM MC background events. Four example signal mass points are shown as colored lines: the bino-wino-coannihilation simplified model with $\Delta m_0 = 1.17$ GeV and three decay lengths ($c\tau$) along with the simplified higgsino model with neutralino mass of 100 GeV and $\Delta m_0 = 0.7$ GeV. The GEANT4-based simulation of events is shown for the background as colored, filled areas divided into different SM processes. All events have to pass the monojet selection as described in Section 3.6.2.

The overall muon efficiency is given by a product of the muon reconstruction efficiency and the soft muon identification efficiency. These efficiencies were previously studied (cf. Figure 2.9).

In addition to the muon tag, further selection criteria are applied to OS track pairs in the SV building process to reduce the number of combinations in the fitter and speed up the fitting algorithm. The distributions of these observables are shown in Figure 3.20 for all candidate SVs with a muon-tagged track in events passing the monojet event selection. The 3D DCA between two tracks in a pair is required to be less than 0.5 cm during the SV building process. This requirement suppresses most random combinations. It estimates the proximity of two given OS tracks based on the full track helix backwards extrapolations including the detailed knowledge of the detector material and magnetic field conditions (cf. Section 2.3.2.1).

Moreover, the invariant mass of a track pair is calculated, and only pairs with $m_{tt} < 3.5$ GeV are considered, where

$$m_{tt} = \sqrt{E_{\text{total}}^{tt}{}^2 - (p_x^{tt2} + p_y^{tt2} + p_z^{tt2})} \tag{3.4}$$

with the total energy

$$E_{\text{total}}^{tt} = E_{t1} + E_{t2} = \sqrt{|P_{t1}|^2 + m_\mu^2} + \sqrt{|P_{t2}|^2 + m_\mu^2}. \tag{3.5}$$

This expression is in agreement with Equation 1.1.2, and assumes the muon mass m_μ for both tracks. The momentum components of the track pair system p_i^{tt} are obtained by summing the momentum components of the two single tracks in each direction. The upper bound on the invariant mass corresponds to the small Δm_0 targeted with this analysis. It also excludes certain known SM low-mass resonances from the selection, such as the J/Ψ-meson for example, and thus leads to a further reduction in the number of possible combinations. For the signal, the distribution of m_{tt} shows a prominent edge, with an endpoint corresponding to the mass difference Δm_0 of a given model. This unique shape results from the limited allowed phase space of the 3-body decay. In the decay $\tilde{\chi}_2^0 \rightarrow \tilde{\chi}_1^0 \, l^+ l^-$ through a Z^*, the allowed phase space of the dilepton pair is given by the mass difference between the $\tilde{\chi}_2^0$ and $\tilde{\chi}_1^0$. Therefore, the m_{ll} distribution at the generator level is expected to have an endpoint at Δm_0. This cut-off is smeared out in the distribution of m_{tt} in Figure 3.20, due to reconstruction and resolution effects on the lepton tracks.

Figure 3.21 shows the number of tracks and SVs in signal and SM MC events that pass the monojet event selection. As these events have more than 500 tracks on average, the selection of candidate tracks including the soft muon tag, as well as the selection of track pairs in the SV building process is essential to reduce the number of possible OS track-track combinations. The right plot of Figure 3.21 shows the number of SVs obtained after the tracks selections and the SV building process. Instead of several thousand, only about 40 track-track combinations pass all prior selection criteria and are reconstructed as an SV.
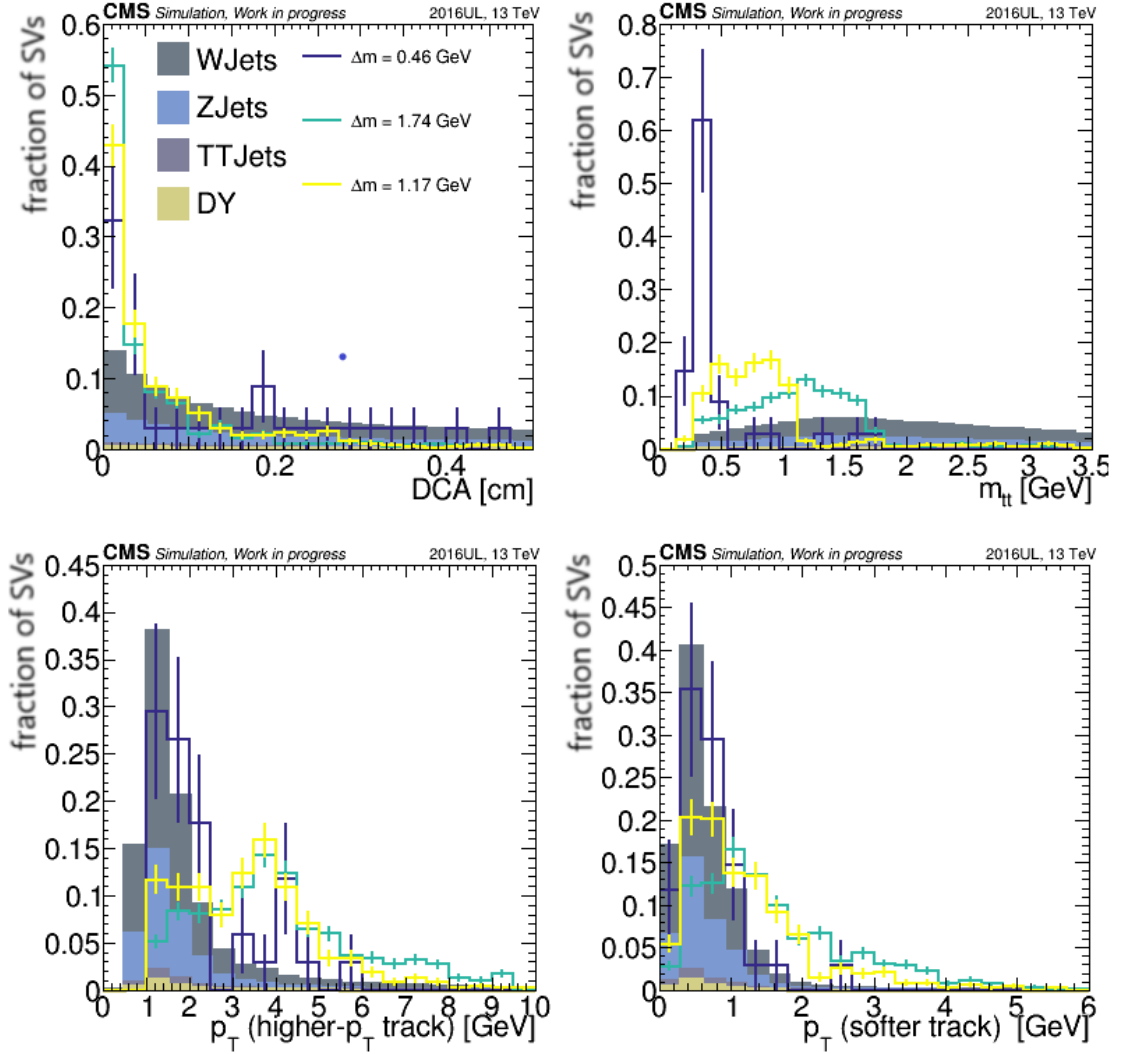
Figure 3.20: Distributions of selection criteria applied to OS track pairs in the SV building process. The distributions are shown for true signal muon-track pairs and reconstructed muon-track pairs from SM MC background events. Events with an $\tilde{\chi}_2^0$ for three signal model points characterized by different Δm_0 are displayed as colored lines. The GEANT4-based simulation of events is shown for the background as colored, filled areas divided into different SM processes. All events have to pass the monojet selection as described in Section 3.6.2. Moreover events have to have at least one SV from a track pair with a soft muon tag (cf. Table 3.4).
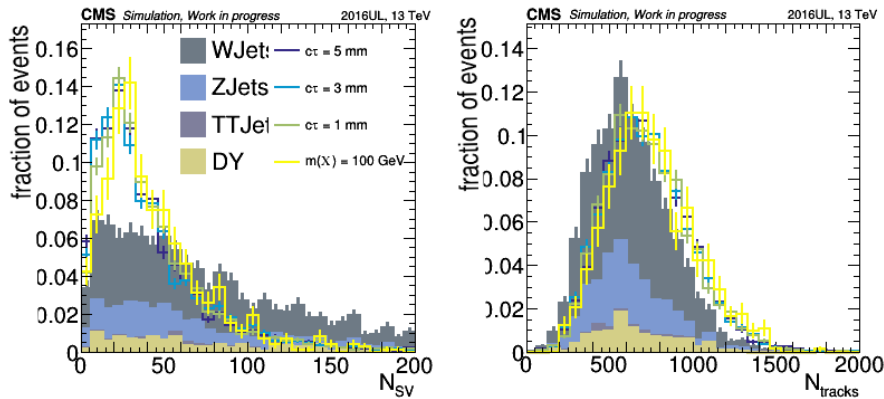
Figure 3.21: Distribution of the number of tracks and SVs in a selection of signal model points and SM MC background events. Four example signal mass points are shown as colored lines: the bino-wino-coannihilation simplified model with $\Delta m_0 = 1.17$ GeV and three decay lengths ($c\tau$) along with the simplified higgsino model with neutralino mass of 100 GeV and $\Delta m_0 = 0.7$ GeV. The GEANT4-based simulation of events is shown for the background as colored, filled areas divided into different SM processes. All events have to pass the monojet selection as described in Section 3.6.2. Moreover events have to have at least one SV from a track pair with a soft muon tag (cf. Table 3.4).

3.6.3.3 Selection of SVs

In the last selection step on object level, multiple SV candidates per event are used as input to a multivariate classifier, to select the true neutralino decay vertex. The selection of candidate tracks, and the selection of track pairs during the SV building method as described in the previous section, are followed by a selection on the SVs after the SV building process. This is the final selection step in the soft displaced muon selection, and the SV-related information can be used as an additional powerful handle. Each secondary vertex has two associated input tracks, that entered the vertex building process. At least one of these two is matched to a soft muon. As described in Section 2.3.2.1, the track fit is repeated for all considered pairs during the SV building, updating the track parameters. Thus, each vertex provides a new estimate of its tracks' momentum and trajectory, subject to the constraint of the vertex. In addition, the vertex itself possesses position and quality information. These three types of objects (input/pre-fit tracks, post-fit tracks, and SVs) are used to select the best candidate SV in each candidate event.
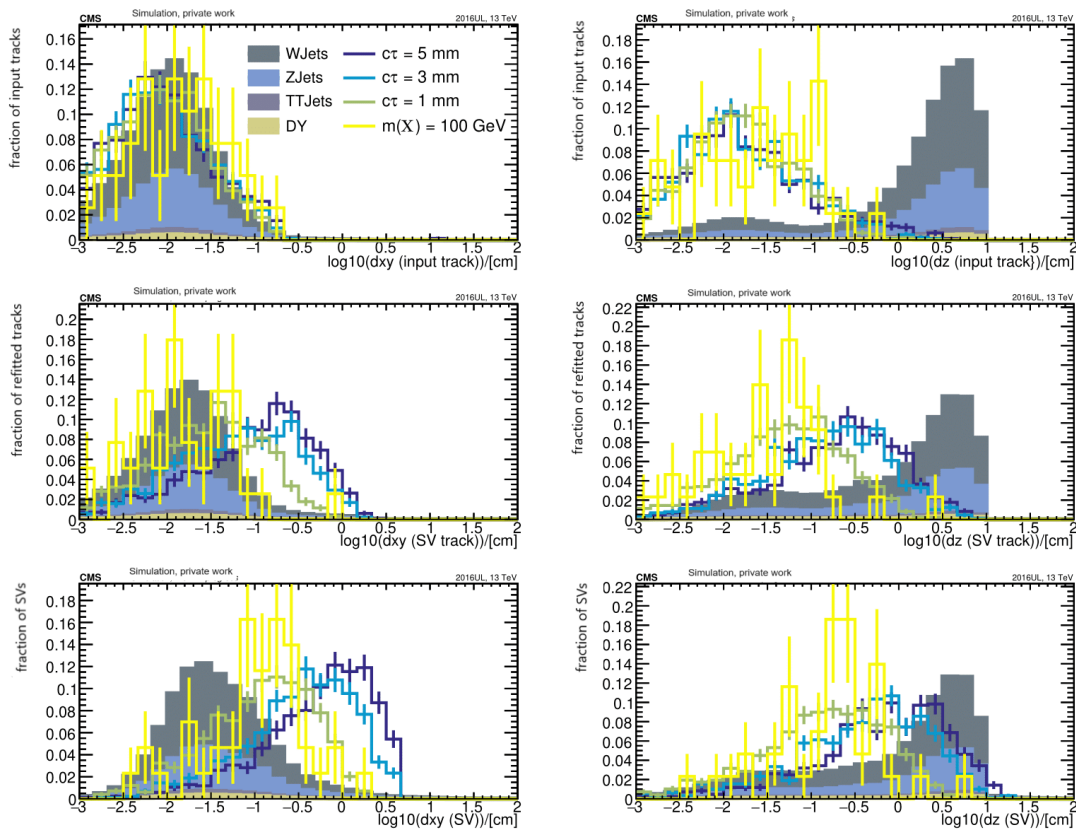
In Figure 3.22, distributions of the longitudinal and transverse impact parameters with respect to the PV are shown for the input tracks (top), the refitted tracks after SV building (middle), as well as the longitudinal and transverse SV-to-PV distance (bottom). With the use of the input tracks, the displacement of the signal with respect to prompt vertices in both longitudinal and transverse directions is not visible from the

95

impact parameters. However, a significant difference becomes visible in the distributions of the impact parameters of the SV tracks (post-fit) and even more clearly in the distributions of the SV-to-PV distance. The reason is that the impact parameters of the input tracks are determined with a linear approximation from the last hit of a track to the PCA with respect to the PV. This linear interpolation is a good approximation for high-momentum tracks but fails to give precise estimates of the impact parameters for softer, curly tracks. A better approach is taken with the V0 Fitter, which uses the track helix. Not only the updated track parameters are more precise, but the impact parameters of the SVs also better distinguish between the displaced signal and prompt tracks from the PV in $d_{xy}(SV)$. However, the distribution of the pre-fit longitudinal track displacement d_z(input track) yields the best separation in that direction between PU vertices and prompt vertices for background tracks. Therefore this quantity is used to reduce drastically the amount of background from PU vertices which have typically large displacements in the z direction of $O(10$ cm$)$. In result, candidate SVs are required to have a longitudinal distance $d_z(\mathrm{SV}) < 10$ cm and d_z(input track) < 1 cm , as well as a transverse distance $d_{xy}(SV) > 100$ μm with respect to the PV. The latter assures that the SV be significantly displaced in the longitudinal plane and therefore distinguishable from the PV, based on the longitudinal resolution of the vertex reconstruction when using only two input tracks to the vertex fit (cf. Figure 3.22).

The selection of candidate SVs serves a dual purpose. First, events are required to have at least one candidate SV, to further reduces the rate of SM background. Second, the background within selected events, in other words mis-matched tracks, can be reduced. Signal (MC background) events with an SV have 40.8 (76.5) SVs (cf. Figure 3.21); there off 20.5 (14.0) are candidate SVs passing the candidate SV selection (cf. Figure 3.33). This reduction of about 50 - 80% in the number of SVs simplifies the identification of the signal SV among all SVs in an event. For this task, a multivariate classification tool is used. The classifier scores each SV in an event based on how signal-like its attributes are, and it is required that the candidate SV be the highest-scoring SV in an event, where the score is computed using the classifier network. This classifier is described in the following section.

Figure 3.22: Distributions of the longitudinal (xy) and transverse (z) impact parameters with respect to the PV for the input tracks selected for the SV building (top), the refitted tracks after SV building (middle), and the SV-to-PV distance (bottom). The distributions are shown for true signal muon-track pairs and reconstructed muon-track pairs from SM MC background events. Four example signal mass points are shown as colored lines: the bino-wino-coannihilation simplified model with $\Delta m_0 = 1.17$ GeV and three decay lengths ($c\tau$) along with the simplified higgsino model with neutralino mass of 100 GeV and $\Delta m_0 = 0.7$ GeV. The GEANT4-based simulation of events is shown for the background as colored, filled areas divided into different SM processes. All events have to pass the monojet selection as described in Section 3.6.2. Moreover events have to have at least one SV from a track pair with a soft muon tag (cf. Table 3.4).

3.6.3.4   BDT as Multivariate Classifier

A multivariate classification algorithm using on the Toolkit for Multivariate Data Analysis with ROOT (TMVA) [141] is used to identify SV from the muonic decay of the $\tilde{\chi}_2^0$. Various architectures were studied for the analysis, including the Boosted Decision Trees, BDTs, and Deep Neural Networks, DNN. Various hyperparameters for both the BDT and DNN were systematically tested. The optimal configuration was chosen based

on the area under the receiver operating characteristic (ROC) curve. ROC curves show the true positive rate against the false positive rate of a classifier at various thresholds. Thus, the area under curve (AUC) of a ROC measures the ability of the classifier to distinguish between classes, with a higher value indicating better performance. The ROC curves for a subset of four of the tested classifier configurations are shown in Figure 3.23. The method chosen for the classification task is the BDT with 150 trees (N = 150). The further hyperparameters for the classifier are specified below in Section 3.6.3.5.
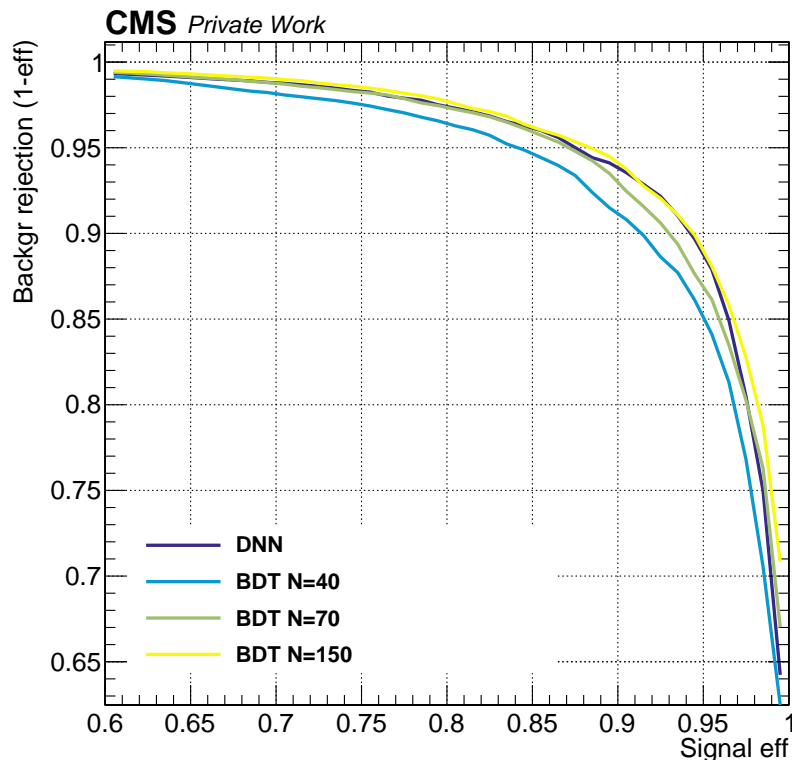
Figure 3.23: Receiver operating characteristic curve for a TMVA DNN classifiers as the dark blue line and three TMVA BDTs with different configurations for the number of trees (N) as the colored lines based on the testing sample in the classifier training (cf. Section 3.6.3.5).

Decision trees are versatile tools used for both classification and regression tasks. In the context of classification, they are employed to categorize samples into multiple categories, such as signal and background, based on input features. *Binary* decision trees are often used for the classification of signal and background, as in this thesis. In a BDT, the classifier assess the extent to which the input data resembles either a signal or background event. The tree consists of n nodes, where each node generates two new nodes based on

a decision expression. The number of nodes on each layer is defined as

$$n_d = 2^d \tag{3.6}$$

with d representing the number of layers or the maximum number of consecutive nodes traversed. A binary decision tree evaluates an expression with a single variable at each node to determine whether the variable exceeds or falls below a predefined threshold. This threshold corresponds to regions in the variable distribution that are either signal-like or background-like.

In Figure 3.24, a representation of a binary decision tree illustrates this structure. It starts from the root node and proceeds with a series of binary divisions based on discriminating variables, denoted as x_i. At each node in the tree, the variable that provides the most effective separation between signal and background when used as a threshold is chosen for the split. Consequently, the same variable may be employed at multiple nodes, while some variables may not be utilized at all. At the end of the tree, where the divisions culminate, are the leaf nodes. These leaf nodes are assigned labels S for signal and B for background, determined by the majority of events that lead to those specific nodes.

To enhance the generalization of the BDT classifier and reduce overfitting, several trees can be ensembled into a collection, or forest. This way, distinctions from multiple individual trees are averaged, making the prediction less sensitive to noise and outliers in the training data.

Each decision tree in a forest is trained to classify the data into signal and background events. The output of each single tree $h(x)$ for a given input x is associated with a weight (w) that characterizes the ability of the tree to distinguish between signal and background. These weighted outputs are then summed for all N trees to form a single classifier

$$y(x) = \sum_{i=1}^{N} w_i h_i(x), \tag{3.7}$$

where $h(x) = -1 \ (+1)$ for background (signal), and small (large) values of $y(x)$ indicate background-like (signal-like) events.

The process of combining multiple decision trees into a single, improved classifier, is known as boosting. In this analysis the adaptive boosting (AdaBoost) algorithm is employed. AdaBoost is designed for binary decision trees and enhances their performance by giving a higher weight to previously misclassified samples in the next iteration, i.e., the training of the following tree. The boost weight α is derived from the misclassification rate (err) of the previous tree

$$\alpha = \frac{1 - \text{err}}{\text{err}} \tag{3.8}$$

normalizing the weights such that the sum of weights remains constant. This changes
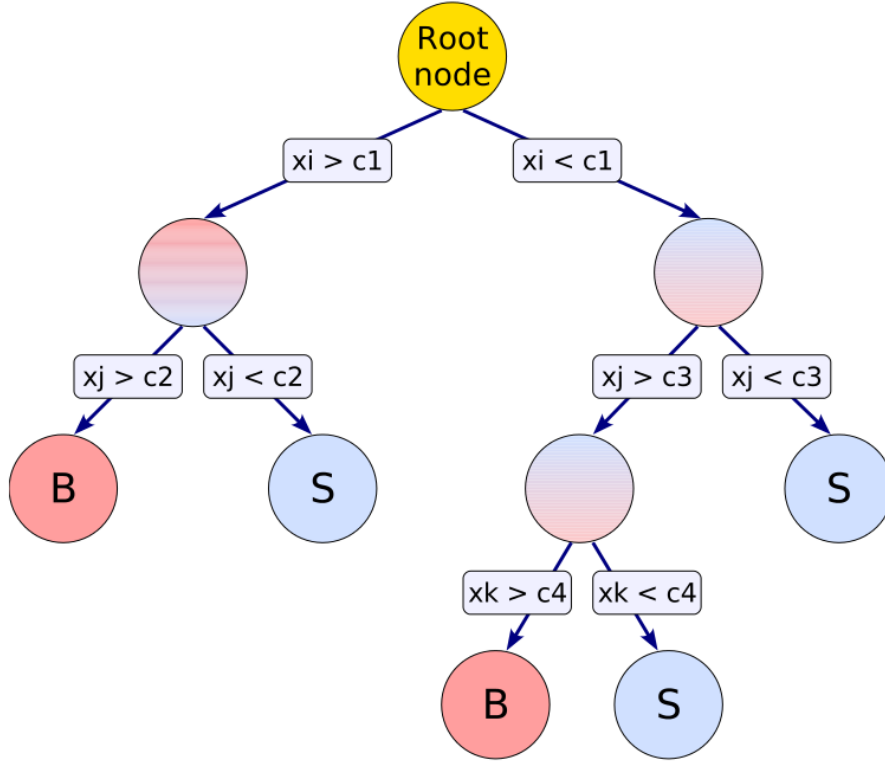
Figure 3.24: Schematic view of a simplified binary decision tree with two layers, for which three variables $x_{i,j,k}$ are considered, in this case exactly one per layer. The output of the decision tree is a classifier to determine if the input is signal (S)- or background-like (B) [141].

Equation 3.6.3.4 accordingly:

$$y_{\mathrm{boost}}(x) = \frac{1}{N} \sum_{i=1}^{N} \ln(\alpha_i h_i(x) \tag{3.9}$$

where the sum is over all N classifiers in the forest.

Training decision trees is the process that defines the splitting criteria for each node. It is an iterative process with several iterations depending on the number of trees used in the classifier. Parameters like maximal depth d and the number of trees N can be adjusted for the training to optimize the separation of signal and background events (cf. Figure 3.23). During the training, the input data are divided into a training and a testing sample. The training set is used to train the model, while the test set is used to assess the classifier's ability to generalize beyond the training data as well as estimate its performance on data it has not encountered during training. This helps prevent

overfitting and to ensure that the model not be just memorizing the training data but learning patterns that can be applied to new data, thus providing a reliable assessment of its prediction capability.

3.6.3.5 Selection of SVs with a BDT

In the final stage of the selection, the most signal-like SV per event is selected using a BDT classifier which takes track-level, SV-level, and event-level information as input. Signal SVs are obtained matching both tracks in an SV to a generator-level muon with a $\tilde{\chi}_2^0$ mother particle within a cone of $\Delta R(\text{track, gen. muon}) < 0.01$ to ensure that no background SVs enter the training as the signal. All SVs that do not fulfill this matching criteria form the background training sample. The approach has the advantage of using the generator-level information to label signal and background SVs, thus allowing supervised learning. SVs used for the signal and background in the training are both obtained from simulated signal events. Background, taken from SVs in signal events that are not matched to the true signal process is subsequently referred to as in-signal background. Learning to optimally reject in-signal background also leads to good rejection of SM backgrounds because the kinematics of low-pT tracks are similar across the signal production and most SM background production processes. Moreover, this choice has the advantage that the classifier is not biased to learn differences in the simulation of the signal compared to backgrounds, as it could be the case when using MC background samples generated with the comprehensive detector simulation (FULLSIM) rather than FASTSIM, as for signal events (cf. Section 3.3 and Section 3.6.3.6).

All generated model points are used in the case of the simplified bino-wino-coannihilation model for the training, while for the compressed higgsino simplified model, only points with $\Delta m_0 < 2$ GeV are used (cf. Section 3.1). This choice results in samples with neutralinos with longer expected mean lifetime. The BDT is made to target these scenarios because they correspond to the unexplored phase space regions of the MSSM. Secondary vertices and the corresponding tracks from dedicated FASTSIM signal simulations described in Section 3.1 are used for the training. The BDT is trained with 150 trees in the forest and a maximum of six layers. The training sample contains 9688 events after the generator filter and selection, which provide both one signal and about 19 background SVs per event on average. To check for overtraining, the pre-selected events are randomly split into a training and testing sample with equal proportions. In total 4844 signal SVs and 10000 background SVs are used in the training, while 4844 signal events are spared for testing.

The input variables to the BDT are chosen based on properties that distinguish signal-matched tracks and SVs from background tracks, such as spurious tracks and random track combinations. These are properties of the input tracks to the SV, the two refitted tracks in the SV, and the SV itself are used in the classification. The refitted tracks are distinguished by their transverse momentum. The track with the lower transverse momentum, i.e., the *softer* track, is denoted as t_s and the track with the higher transverse momentum, usually the muon tagged track, as t_h. TMVA provides a summary of the

relative importance of variables encountered in the training. The input variables ordered by that importance are

1. $\Delta R(t_h, t_s)$,
2. $\Delta\phi(\vec{t}_{\text{sys.}}, \vec{p}_T^{\text{miss}})$,
3. the invariant mass m_{tt},
4. $\log_{10}(\hat{d}_{xyz}^{PU}(t_s)/\sigma(\hat{d}_{xyz}^{PU}(t_s)))$,
5. $p_T(t_s)$,
6. $\vec{t}_{\text{sys.}xy}$,
7. $\Delta\phi(\vec{t}_{\text{sys.}}, \vec{n})$,
8. $\log_{10}(\hat{d}_{xyz}^{PU}(t_s))$,
9. $\log_{10}(\hat{d}_{xyz}^{PU}(t_h)/\sigma(\hat{d}_{xyz}^{PU}(t_h)))$,
10. $N_{\text{valid hits}}(t_s)$,
11. $\log_{10}(\hat{d}_{xyz}^{PU}(t_h))$,
12. 3D DCA[1] between t_h and t_s,
13. $\Delta\phi(\vec{n}, \vec{P}_T^{\text{miss}})$,
14. $p_T(t_h)$,
15. $\log_{10}(\hat{d}_{xyz}^{PV}(t_s))$,
16. $\log_{10}(\hat{d}_{xyz}^{PV}(t_h))$,
17. $\log_{10}(d_{xy}(\text{SV}))$,[1]
18. $|\eta(t_h)|$,
19. $\log_{10}(\hat{d}_{xyz}^{PV}(t_s)/\sigma(\hat{d}_{xyz}^{PV}(t_s)))$,
20. $\log_{10}(d_z(\text{SV}))$,[1]
21. $\log_{10}(\hat{d}_{xyz}^{PV}(t_h)/\sigma(\hat{d}_{xyz}^{PV}(t_h)))$,
22. $N_{\text{valid hits}}(t_h)$,
23. $|\eta(t_s)|$,
24. $\chi^2/$ Ndof (V0 fitter). [1]

Here, $\vec{n}$ is defined as the spatial vector pointing from the PV to the SV,

$$\vec{n} = \begin{bmatrix} x_{SV} \\ y_{SV} \\ z_{SV} \end{bmatrix} - \begin{bmatrix} x_{PV} \\ y_{PV} \\ z_{PV} \end{bmatrix}. \tag{3.10}$$

The vectorial sum of the spatial vectors of the two refitted tracks in an SV is $\vec{t}_{\text{sys.}} = \vec{t}_s + \vec{t}_h$. The d_{xy}, and d_z denote the displacement with respect to the PV, and the invariant mass m_{tt} is defined in Equation 3.6.3.2. The significance of the impact point (IP) of a track is defined as $\hat{d}_{xyz}^{PV}/\sigma(\hat{d}_{xyz}^{PV})$, where $\hat{d}_{xyz}^{PV}$ is the 3D displacement of a track with respect to the PV derived with a helical approximation [142]. The helical approximation is a calculation that uses less information compared to the V0 Fitter and is applied to single tracks. However, it can still improve on the precision of the determination of a track's impact parameter. As a standard method, the displacement of a track is defined using a linear approximation from the reference point of a track to the PV (cf. Section 2.3.1). However, this is increasingly imprecise for progressively softer tracks due to the smaller curvature (larger bending) of these tracks. Therefore, in the helical approximation, tracks are extrapolated from their reference point along a helix with constant radius. A constant magnetic field is assumed, which is a good approximation in the concerned region within a few millimeters around the beam line. The helical approximation technique leads to a more precise determination of the displacements for

---

[1]calculated in the SV building process

signal-like tracks. The IP significance with respect to PU is defined as $\hat{d}_{xyz}^{PU}/\sigma(\hat{d}_{xyz}^{PU})$ with $\hat{d}_{xyz}^{PU}$ being the 3D distance to the closest PU vertex.

This search does not rely on MC simulation for the final estimation of background sources. However, any mismodeling of track properties in the MC simulation used to train the BDT could lead to a suboptimal classifier. A less-than-optimal modeling of the input observables for the BDT training can affect the signal and background rejection efficiency when applied to data.

Figures 3.25 to 3.28 show the corresponding distributions of the BDT input variables for data and SM MC background events, as well as the in-signal background as used in the training of the BDT. In addition to that, four example signal mass points are shown: the bino-wino-coannihilation simplified model with $\Delta m_0 = 1.17$ GeV and three different lifetimes along with the simplified higgsino model with $\Delta m_0 = 0.32$ GeV. The distributions are shown after the monojet event selection and the soft displaced muon selection, before the evaluation of the BDT (steps 1 to 3.4. in Figure 3.16). All events are required to have at least one candidate SV. The most significant difference between signal and background shape can be seen for the opening angle of the two tracks forming an SV, $\Delta R(t_s, t_h)$, for which the MC background shows a flat shape in comparison to a peaking signal distribution. This indicates that signal tracks with small Δm_0 have small opening angles, while the background is dominated by combinations of spurious tracks, which are distributed isotropically. The second-leading BDT input variable is $\Delta\phi(\vec{t}_{\text{sys.}}, \vec{p}_T^{\text{miss}})$.[2] While the signal tracks are aligned with the direction of $\vec{p}_T^{\text{miss}}$, which is correlated with the direction of the neutralinos, the background tracks are distributed more isotropically. This is consistent with processes arising from pileup and spurious tracks, which are in principle randomly scattered in ϕ. Furthermore, the invariant mass of the track pair m_{tt} (cf. Equation 3.6.3.2) shows the prominent mass edge for signal. No prominent resonance occurs in the background, which leads to a clear separation of the signal over a flat background. The impact parameters (IP) $\hat{d}_{xyz}$ and IP significances $\hat{d}_{xyz}/\sigma(\hat{d}_{xyz})$ are useful in particular for rejecting pile-up background as well as background from spurious prompt tracks.

Figure 3.26 (middle) shows a considerable difference between the momentum of the softer track and the higher-momentum track in a candidate SV for signal. This is another significant difference between the signal and the background, which consists of two similarly soft tracks, with transverse momenta around 1-2 GeV. The distribution of the number of valid hits of the softer track, cf. Figure 3.27, shows that soft background tracks have less valid hits than signal tracks on average. For the softer track in background SVs two potential sources can be identified from Figure 3.27 (middle, right). In the figure, two populations are visible for in-signal and SM backgrounds: tracks with 12 or fewer valid hits, which can be regarded as fakes, mal-reconstructed or forward tracks, and tracks with an average nominal number of hits of around 15 to 25. Thus, the transverse momentum in combination with the number of valid hits are useful variables to distinguish

---

[2] Note that $\vec{p}_T^{\text{miss}}$ is denoted as MET in Figures 3.25 to 3.28.

signal tracks from badly reconstructed tracks and fake tracks from SM background SVs.

The in-signal background, behaves differently than the SM MC backgrounds in many of the shown kinematic distributions. In the in-signal background one of the signal tracks can be paired with a second random or fake track, giving rise to two populations in these distributions: a signal-like population from the signal component in the background, and a population at similar values as the SM MC background. The effects of this on the BDT performance are discussed in the next section.
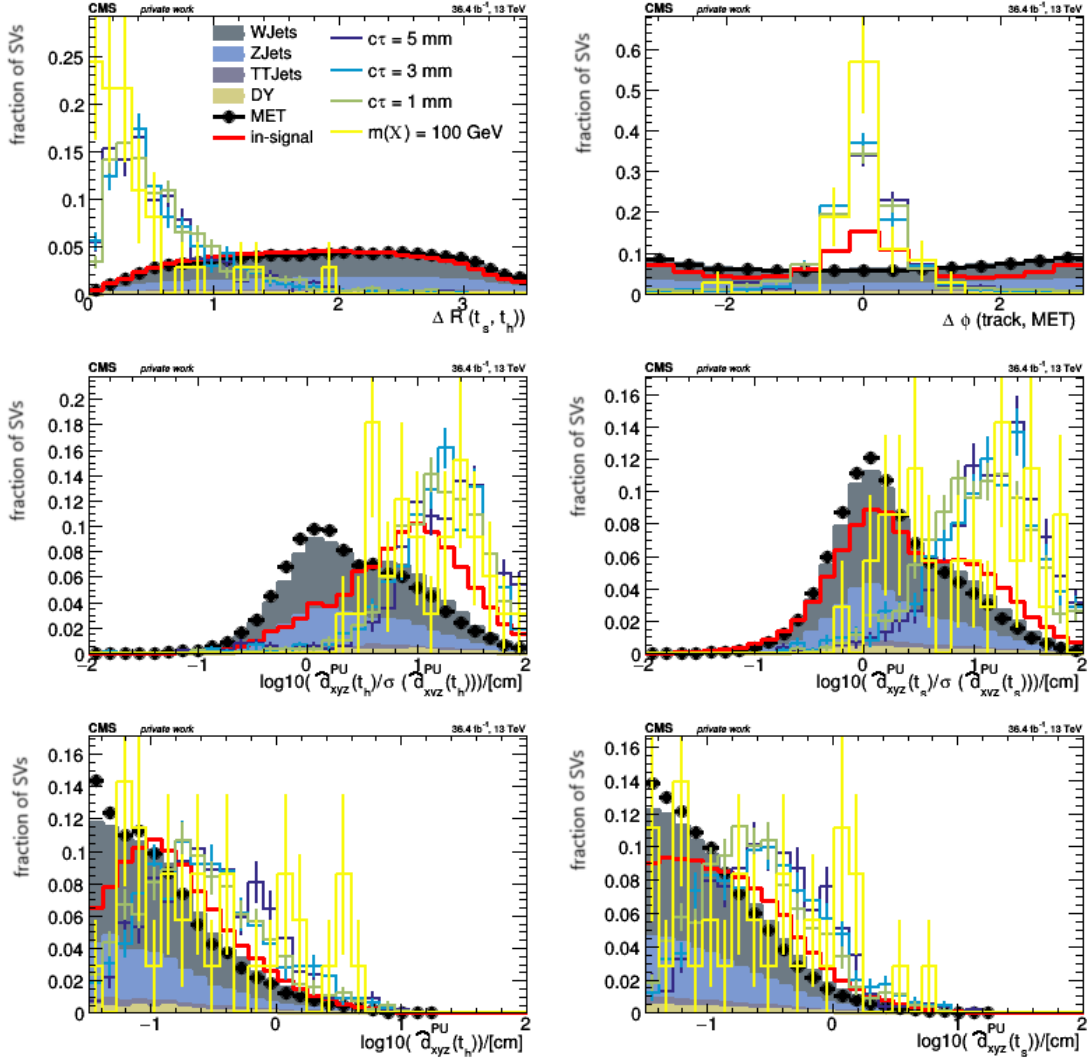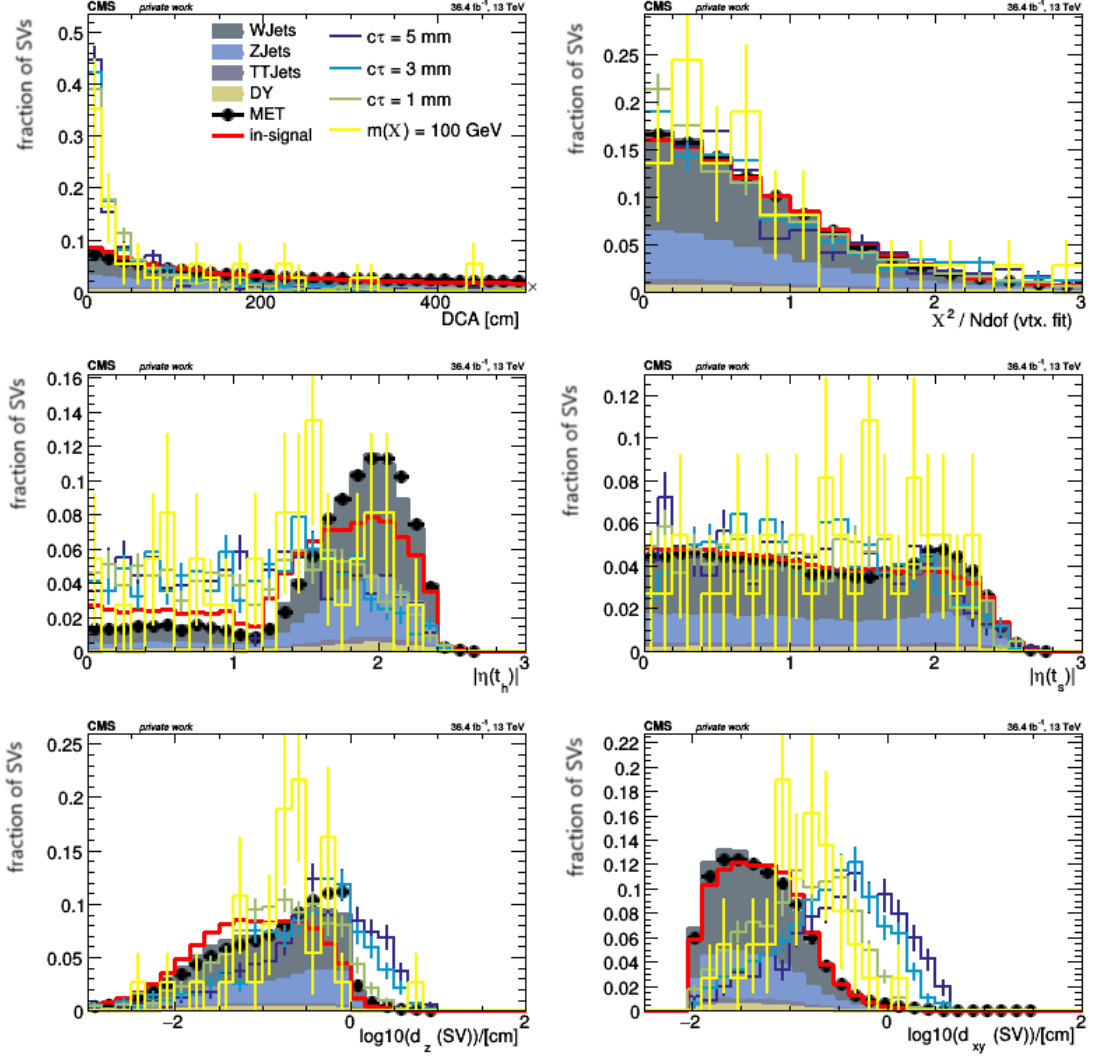
Figure 3.25: Distributions of the BDT input variables from reconstructed muon-track pairs for data as black dots, the GEANT4-based simulation of background events divided into different SM processes as colored, filled areas, as well as the in-signal background from FASTSIM simulated signal events as a red line. In addition, distributions are shown for true signal muon-track pairs for four example signal mass points as colored lines: the bino-wino-coannihilation simplified model with $\Delta m_0 = 1.17$ GeV and three different lifetimes along with the simplified higgsino model with $\Delta m_0 = 0.32$ GeV. All events have to pass the monojet selection as described in Section 3.6.2. Moreover events have to have at least one candidate SV from a track pair with a soft muon tag (cf. Table 3.4 and steps 1. to 3.4. in Figure 3.16). Distributions of the input tracks to the SV building method are defined twice, once for each track in a candidate SV, with t_s being the lower-momentum (softer) track, and t_h being the higher-momentum track in a pair.

Figure 3.26: Distributions of the BDT input variables from reconstructed muon-track pairs for data as black dots, the GEANT4-based simulation of background events divided into different SM processes as colored, filled areas, as well as the in-signal background from FASTSIM simulated signal events as a red line. In addition, distributions are shown for true signal muon-track pairs for four example signal mass points as colored lines: the bino-wino-coannihilation simplified model with $\Delta m_0 = 1.17$ GeV and three different lifetimes along with the simplified higgsino model with $\Delta m_0 = 0.32$ GeV. All events have to pass the monojet selection as described in Section 3.6.2. Moreover events have to have at least one candidate SV from a track pair with a soft muon tag (cf. Table 3.4 and steps 1. to 3.4. in Figure 3.16). Distributions of the input tracks to the SV building method are defined twice, once for each track in a candidate SV, with t_s being the lower-momentum (softer) track, and t_h being the higher-momentum track in a pair.

Figure 3.27: Distributions of the BDT input variables from reconstructed muon-track pairs for data as black dots, the GEANT4-based simulation of background events divided into different SM processes as colored, filled areas, as well as the in-signal background from FASTSIM simulated signal events as a red line. In addition, distributions are shown for true signal muon-track pairs for four example signal mass points as colored lines: the bino-wino-coannihilation simplified model with $\Delta m_0 = 1.17$ GeV and three different lifetimes along with the simplified higgsino model with $\Delta m_0 = 0.32$ GeV. All events have to pass the monojet selection as described in Section 3.6.2. Moreover events have to have at least one candidate SV from a track pair with a soft muon tag (cf. Table 3.4 and steps 1. to 3.4. in Figure 3.16). Distributions of the input tracks to the SV building method are defined twice, once for each track in a candidate SV, with t_s being the lower-momentum (softer) track, and t_h being the higher-momentum track in a pair.

Figure 3.28: Distributions of the BDT input variables from reconstructed muon-track pairs for data as black dots, the GEANT4-based simulation of background events divided into different SM processes as colored, filled areas, as well as the in-signal background from FASTSIM simulated signal events as a red line. In addition, distributions are shown for true signal muon-track pairs for four example signal mass points as colored lines: the bino-wino-coannihilation simplified model with $\Delta m_0 = 1.17$ GeV and three different lifetimes along with the simplified higgsino model with $\Delta m_0 = 0.32$ GeV. All events have to pass the monojet selection as described in Section 3.6.2. Moreover events have to have at least one candidate SV from a track pair with a soft muon tag (cf. Table 3.4 and steps 1. to 3.4. in Figure 3.16). Distributions of the input tracks to the SV building method are defined twice, once for each track in a candidate SV, with t_s being the lower-momentum (softer) track, and t_h being the higher-momentum track in a pair.

3.6.3.6 BDT Validation

Figure 3.29 shows the BDT classifier score evaluated in the training and testing samples. The distributions are expected to be similar; larger differences between the two could indicate overtraining due to too-small training samples or due to overly complex architecture. To assess the similarity between the testing and training distributions, we employ a Kolmogorov-Smirnov (KS) test, as executed within the TMVA framework. This metric helps to gauge the extent of the distributions' likeness. For any two random samples drawn from the same parent distibution, the KS test value would be distributed uniformly between 0 and 1. A small number (close to zero) means that the test and training distributions are significantly different, which could be a sign of overtraining. Figure 3.29 prints the Kolmogorov-Smirnov tests. No overtraining is observed for the BDT classifiers, as shown in the figure. An event-level observable is defined by the maximum BDT scores of all SVs in an event.
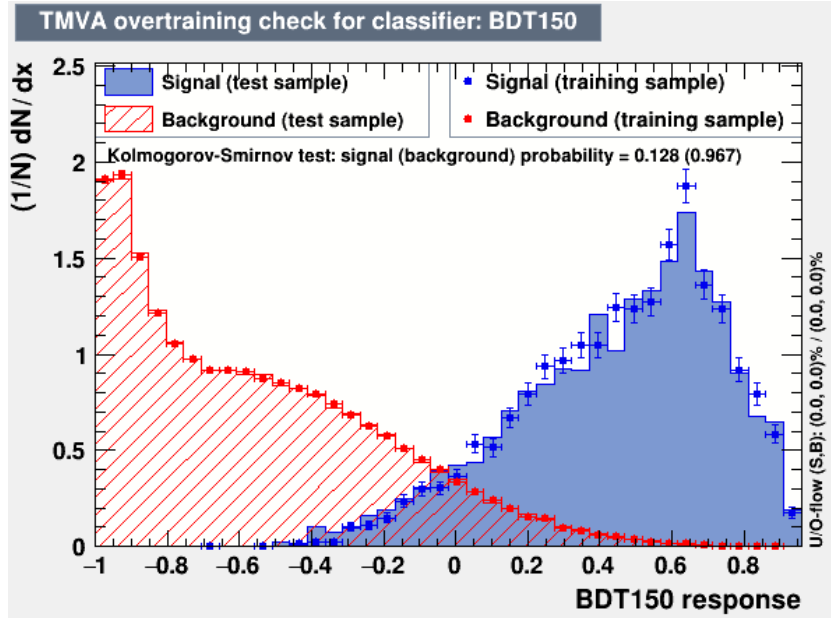
Figure 3.29: BDT classifier score in background and signal samples, for both the training and the testing components. The normalized occurrence is given on the y-axis as a function of the classifier for the BDT with 150 trees used in the analysis on the x-axis. The classifier is given for the training and testing sets of SVs as dots and filled areas, and for signal SVs in blue as well as background SVs in red.

The agreement between data and MC is investigated for the BDT classifier. A validation region is selected which is orthogonal to the signal region. This orthogonal data set serves several purposes: for establishing a background estimation method, for validating the BDT, and for selecting a signal region. For this purpose, the requirement of opposite charge for any pair of tracks in the SV building method is inverted, allowing the V0

Fitter to reconstruct only vertices from same-sign (SS) tracks. For each secondary vertex passing the selection, the BDT is evaluated using the same input observable as used for the training.

The BDT classifier after the evaluation is shown for MC backgrounds and same-sign data in Figure 3.30. In the figure, the maximum BDT classifier score among all SVs within events is shown for the in-signal background that has been used for the training of the BDT, for SM MC background samples, for the data CR, and for selected signal model points. No significant difference in the shapes of the different physics processes in the SM MC background are visible. This suggests that the soft components of events, which is mostly originating from underlying event, PU and fake tracks, are very similar for different hard processes. The implications of this are further discussed in Section 3.7. While the data is in good agreement with the SM MC backgrounds, differences are visible between the in-signal background and the SM MC backgrounds, as well as the data. This can be explained through several effects. First, two different simulations are used to obtain the background events. While FastSim is used for signal events, FullSim is used for MC backgrounds. However, this is expected to lead to a minor difference, as most track related variables are well modeled, even for signal like tracks (cf. Appx. Figures A.3 to A.9). The second reason is the different event kinematics in signal events compared to MC background events (cf. Figure 3.18). Third, the in-signal background can contain the pairing of a signal track with a random track from the event, as previously mentioned. This enhances the background composed of one true track and one fake track, which is more difficult to distinguish from true SVs (signal) than the combination of two fake tracks. Using in-signal background for the training of the BDT thus emphasizes the more difficult background types in the training. A more comprehensive discussion of the categorization of the background with respect to the nature of the tracks and SVs (true/fake) is made in the next section.
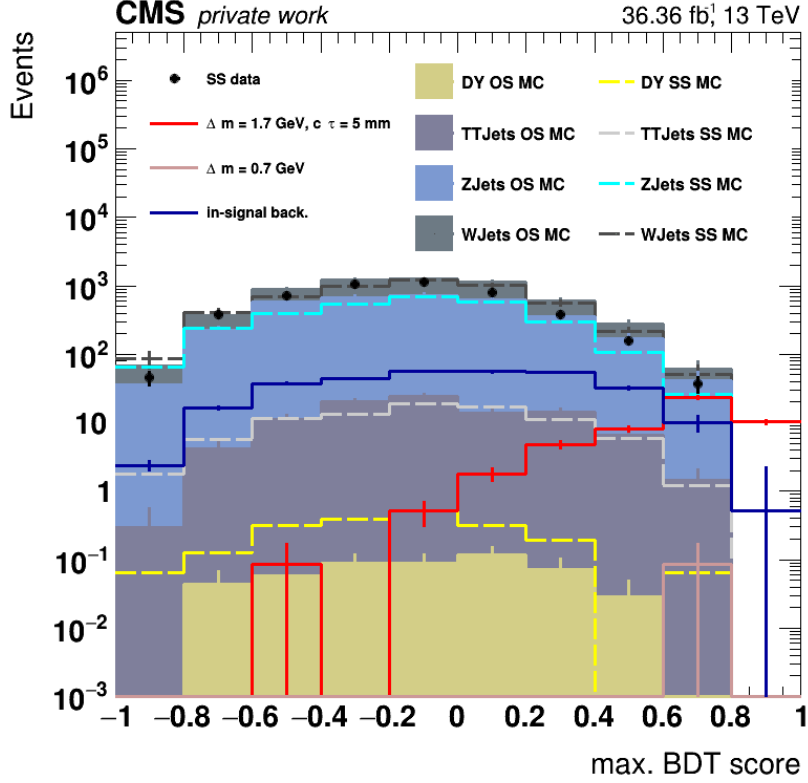
Figure 3.30: Maximum of the BDT classifier among all candidate SVs within selected events from the GEANT4-based simulation of background events divided into different SM processes as colored, filled areas, the in-signal background from FASTSIM simulated signal events as a blue line and data from the control region as black dots. The data control region uses same-sign (SS) SVs. The same charge selection is additionally applied to the SM MC backgrounds, shown as the colored dashed lines. Signal distributions are shown for true signal muon-track pairs from two example signal mass points as colored lines: the bino-wino-coannihilation simplified model with $\Delta m_0 = 1.7$ GeV along with the highest cross-section point in the range of simplified higgsimo model points with a mass of the $\tilde{\chi}_2^0$ of 100 GeV and $\Delta m_0 = 0.7$ GeV. The event selection as well as all object selections are applied as described in Section 3.6.

3.7   Background Estimation

Processes that contribute to event counts in the signal region, but that are not attributed to the signal process, are referred to as backgrounds. Backgrounds can arise from SM processes with final states closely resembling the signal, or due to detector effects and mismeasurements. An example of a background that arises from truly similar physics is the Drell-Yan process (cf. below). In a Drell-Yan event, low-momentum opposite-charge same-flavor dilepton pairs are produced from an off-shell Z^* or γ^*. However, there is

111

no source of $|\vec{p}_T^{\,\mathrm{miss}}|$ in this process. An example of a background process that is due to mismeasurement is the production of W bosons in association with jets, where one lepton comes from the leptonic decay of the W boson, and another lepton is due to either mismeasurement, i.e., a fake lepton, or as part of a hadronization process. The neutrinos in these events lead to a significant amount of $|\vec{p}_T^{\,\mathrm{miss}}|$. In this analysis, the background is collectively estimated using data, as described in Section 3.7.2.

3.7.1 Background Classification

When discussing potential backgrounds for this analysis, two aspects are of importance: one is to identify SM processes that resemble the overall signal event topology (cf. Section 3.5). The other is to identify events, where the soft part of the event, namely the common secondary vertex of a low-momentum muon-plus-track pair, is similar to events with a signal SV. For the first aspect, it is relevant to identify SM processes that produce a high-momentum jet and larger amounts of $|\vec{p}_T^{\,\mathrm{miss}}|$. A comprehensive list of the SM processes that have been studied with MC samples is given below, along with descriptions of what qualifies the respective process as a background in this analysis. The processes are ordered according to their contribution in the signal region. With regard to the soft topology of signal events, it was found that the dominant source of background in the analysis is from events with two fake or spurious tracks. Fake tracks are reconstructed tracks that do not correspond to the trajectory of an actual charged particle produced in the collision; instead, these tracks may arise from various sources of instrumental noise, electronic noise, or other detector or reconstruction artifacts. A detailed discussion of the fake background is given below.

W bosons in association with jets (WJets)
In this SM process, a W boson is produced alongside jets and decays leptonically into a lepton and a neutrino: $W + \text{jets} \rightarrow l\nu + \text{jets}$. Since a neutrino is present in the final state, there can be significant real missing transverse momentum. Events with an identified high momentum lepton are vetoed. However, the very low transverse momentum threshold for the tracks with a muon tag allows for a considerable rate of either a fake misidentified lepton or a low-pT lepton originating from a hadronization process to pass the analysis selection.

Z bosons in association with jets (ZJets)
In this SM process, there is a production of a Z boson alongside jets, decaying into two neutrinos: $Z + \text{jets} \rightarrow \nu\nu + \text{jets}$. The two neutrinos in this process contribute to true $|\vec{p}_T^{\,\mathrm{miss}}|$ in the event. The muon and track candidates can either be fake, or come from a decay of a meson produced in a hadronization process.

Drell-Yan process (DY)
The Drell-Yan process is a high-energy particle interaction involving the annihilation of a quark and an antiquark, resulting in the creation of a virtual photon or Z boson. This

virtual boson can subsequently decay into a pair of charged fermions (e.g., electrons or muons). When two muons are produced via $Z/\gamma^* \to \mu\mu$, true missing transverse momentum is not part of the production. Therefore, a relatively high $|\vec{p}_T^{\mathrm{miss}}|$ cut, as used in this analysis, suppresses these types of backgrounds. However, in the production of two tau leptons, each tau lepton can decay into a muon alongside two neutrinos, i.e., $\tau \to \mu\bar{\nu}_\mu\nu_\tau$, producing real missing transverse momentum in the event alongside two real leptons.

Top quarks in association with jets (TTJets)
When single top quarks or top quark pairs are produced, each top decays to a W boson and a b quark, with a branching fraction close to 100%. The W boson can decay to a charged lepton and a neutrino, contributing to real missing transverse momentum and, given the general abundance of low-p_T tracks and fake leptons, can satisfy the dimuon or track+muon selection. Despite the veto of b-tagged jets as a component of the monojet selection, a non-negligible rate of $t\bar{t}+$ jet events persists in the signal region.

Other backgrounds
Minor sources of background are diboson and higher-order processes, which have much lower production cross sections, and are therefore negligible in this analysis; moreover, QCD comprises events arising from the production and radiation of quarks and gluons followed by their hadronization and showering into jets. Most QCD events contain no real $\vec{p}_T^{\mathrm{miss}}$. Most $\vec{p}_T^{\mathrm{miss}}$ present in a QCD event is due to the mismeasurement of jet energy. The relatively high $|\vec{p}_T^{\mathrm{miss}}|$ cut, in combination with requiring $\Delta\phi(\vec{p}_T^{\mathrm{miss}}, \mathrm{jet}_{1,2,3,4}) > 0.5$ makes the QCD background negligible in this analysis.

Another potential source of background are resonances. Resonances are composite particles, namely mesons or baryons, that occur in any interaction due to hadronization and can decay into leptons. An overview on long-lived, low-mass, neutral, compound particles in the SM is given in Table 3.7.1. Only few SM resonances are longer-lived. Low-mass, neutral, compound particles with a $c\tau$ that could allow it to pass the selection on the transverse impact parameter ($d_{xy} > 100\mu\mathrm{m}$) are the K_S^0 (cf. Section 1.3.2), D_0, Xi, and Λ. All four have a BR to muons of less than 1 %. Therefore, although resonances can be an important background for searches with prompt soft lepton in the final state, they have been found to be of minimal importance for this analysis. Further discussion of the contribution of resonant decays to the total background is given below.

The combinatorial background in the low-momentum regime is expected to be largely independent of the hard process and mainly influenced by the number of PU vertices. Figure 3.30 shows the maximum BDT classifier for the main backgrounds. The similarity in shapes among the backgrounds confirms the process-independence of signal candidate objects. For further simulation studies of the background, the background is categorized with respect to the nature of the two tracks that contribute to the highest-scoring SV per event. Consequently, the background categories are as follows:

- the combination of two fake tracks (ff);

113

	Name	Mass [MeV]	Mean lifetime τ [s]	cτ [m]
Mesons	Rho (ρ)	82.66	4.45×10^{-24}	1.34×10^{-18}
	Pion (π^0)	134.98	8.43×10^{-17}	2.53×10^{-8}
	Kaon (K_S^0, K_L^0)	497.61	$8.95 \times 10^{-11}, 5.12 \times 10^{-8}$	0.027, 15.34
	Eta (η, η')	547.86, 957.78	$5 \times^{-19}, 3.2 \times 10^{-21}$	$1.50 \times^{-10}, 9.59 \times 10^{-13}$
	Omega (ω)	782.65	7.7×10^{-23}	2.31×10^{-14}
	Phi (ϕ)	1019.49	1.54×10^{-22}	4.62×10^{-14}
	D (D^0)	1864.84	410×10^{-15}	123×10^{-6}
Baryons	Lambda (Λ)	1120	2.631×10^{-10}	0.078
	Sigma (Σ^0)	1192.64	7.4×10^{-20}	2.22×10^{-11}
	Xi (Ξ^0)	1314.86	2.90×10^{-10}	0.087
	Omega (Ω)	2.70	268×10^{-15}	80×10^{-6}

Table 3.5: Electrically neutral low-mass compound particles in the SM with masses below 3 GeV [24].

- the combination of one true track with a fake (tf);

- the combination of two true tracks that do not belong to a true SV (tt);

- the combination of two true tracks that originate from a true common SV (sv).

This categorization is made by an association of reconstructed and generator-level objects. A matching between the input tracks to the SV building method and all generated particles requires ΔR between the track and a matching particle to be less than 0.01. Moreover, the same charge is required between the track and the generator-level particle. Tracks that cannot be matched to any generator particle are defined as fake tracks, while tracks that have a match are defined as true tracks. Tracks from pile-up interactions will appear in the ff category. However, tracks from PU interactions are strongly suppressed by the track selection, and the cut on the longitudinal displacement of the input tracks to the SV building method in particular (cf. Section 3.6.3.3). A track pair with a matching generator-level particle each, is assembled in the tt category if these two particles do not originate from the same mother particle at generator level. Track pairs that match to a generator-level particle and the same mother particle make up the sv category.

As shown in Figure 3.31, the background is dominated by events with pairs of two fake tracks (combinatorial background) (ff), followed by one true and one fake or spurious track (tf) and pairs of true tracks (tt). The background through SM processes with

true secondary vertices (sv) contributes almost negligibly. In the region of large BDT classifier scores, the dominant category is from pairs of true tracks, followed by the combination of a true track with one fake.

3.7.2 Background Estimation Method

The background amount is estimated using the data. This approach offers several advantages over simulation-based background predictions. These advantages include robustness against theoretical uncertainties, such as uncertainties in cross sections, branching fractions, and hadronization models which can lead to incorrect production rates or normalization. Additionally, the detector geometry and response, as well as real-time data taking conditions, which typically vary dynamically throughout a given run, are accounted for.

In a data-based approach, a control sample is defined in data with events that satisfy the same selection criteria as the SR. Instead of selecting events with one soft displaced muon and one track of opposite sign, the muon and the track in the control sample are required to have the same electric charge. The contamination of the SS control sample by signal is negligible. This background estimate assumes that the background events are produced with equal rates for OS and SS events. This is expected for background categories with fake tracks or random combinations of true tracks (tt) because at least one track in such a pair is randomly selected, and its electric charge is not correlated with the charge of the tagged muon or the other track.

The background category with the smallest contribution to the total, the sv background, is not expected to be fully predicted by the data-driven SS background method. The decay of unstable particles via the electroweak force, in particular the tau lepton, can be classified by the number of charged particles in the decay. For one charged particle, the decay is called a 1-prong decay, and for three charged particles, it is called a 3-prong decay. The 3-prong decays lead to pairs of oppositely charged particles along with a third particle of either charge. The decay is thus charge symmetric and yields two tracks of the same sign in 50% of all cases, on average. The SV building method selects two of the three tracks produced by the decay products of a 3-prong decay. However, if the SV building combines same-sign tracks, it neglects 50% of the total decay products of a 3-prong decay. More importantly, the decay of resonant particles to *pairs* of OS particles is not contained in the SS background prediction method by construction. Since the sv category is the least important background, this underprediction is covered by the total uncertainty of the background method and needs no dedicated correction.

3.7.3 Closure of the Background Method

The assumption that OS and SS background events are produced with equal rates in the signal region is tested in simulation using SM MC events from the major backgrounds stated above: WJets, ZJets, TTJets and DY. Figures 3.31 and 3.32 show the number of observed SS and OS events as a function of the maximum BDT score of the candidate

115

SV from SM MC background processes. The MC simulations are weighted to account for production cross-sections and luminosity. The events are selected by applying the complete object and event selection. The background is categorized as described above in ff, tf, tt, and sv. In Figure 3.31, events from all background processes are displayed. The ratio of OS to SS events is shown in each background category and for the sum of categories (stack). In Figure 3.32, the ratio is shown for WJets, ZJets, TTJets and DY events separately. The ratio of OS to SS events was found to be compatible with 1 within 26 % or less in all bins. This degree of non-closure is taken from the fit to the ratio of OS to SS events in all background categories combined (green line in Figure 3.31) and employed as the total systematic uncertainty on the background prediction.
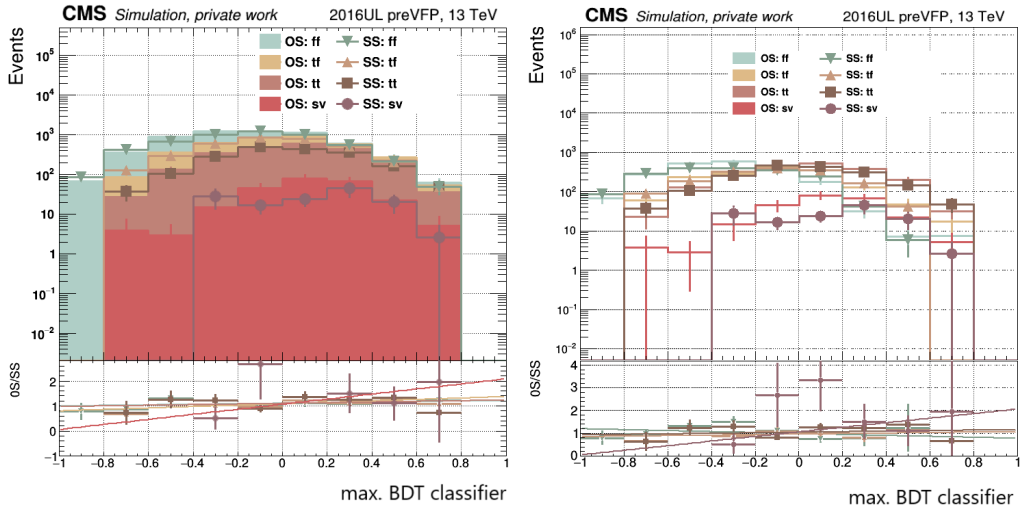
Figure 3.31: Number of observed SS and OS events as a function of the maximum BDT classifier of the candidate SV from MC simulation of background events. All event and object selection criteria are applied as described in Section 3.6. The background categories are: the combination of two fake tracks (ff); the combination of one true track with a fake (tf); the combination of two true tracks that do not belong to a true SV (tt); and the combination of two true track that originate from a true common SV (sv). The distributions for OS and SS are compared with the sum of categories stacked (left), and in each background category individually (right)). The OS to SS ratio is given in the lower panel.

In Figure 3.33, the distributions of the number of SVs (N_{SV}) and candidate SVs that pass the SV selection (N_{SV}(candidate)) are given for SS and OS events from SM MC background events. All event and object selection criteria are applied as described in Section 3.6. Good agreement between SS and OS in this quantity is essential, because a higher (lower) number of candidate SVs can lead to a systematically lower (higher) maximum score in the BDT evaluation through the larger (smaller) statistical sample.
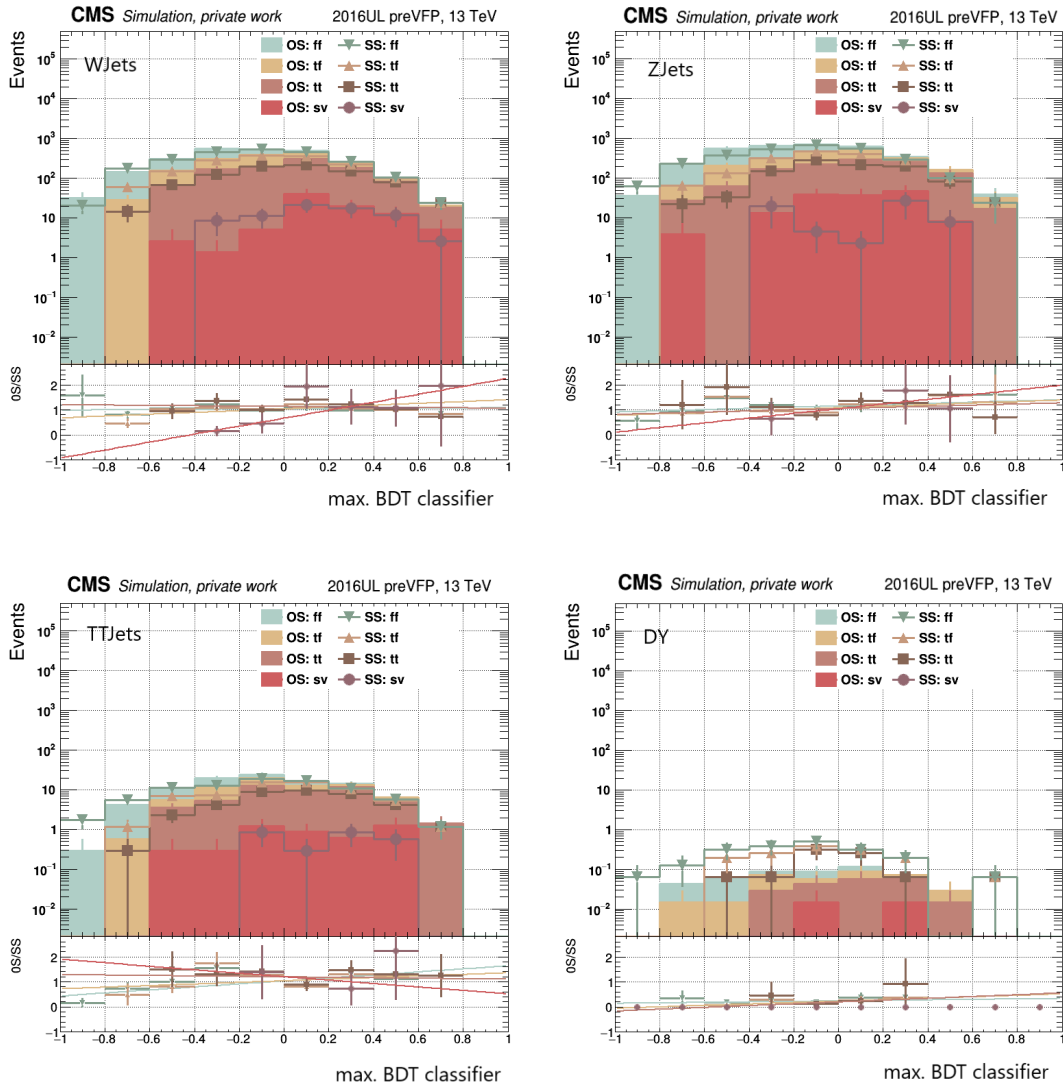
Figure 3.32: Number of observed SS and OS events as a function of the maximum BDT classifier of the candidate SV from MC simulation WJets (top left), ZJets (top, right), TTJets (bottom, left) and DY (bottom, right) background events. All event and object selection criteria are applied to the events as described in Section 3.6. The background categories are: the combination of two fake tracks (ff); the combination of one true track with a fake (tf); the combination of two true tracks that do not belong to a true SV (tt); and the combination of two true track that originate from a true common SV (sv). The distributions for OS and SS are compared for the sum of these categories stacked. The OS to SS (stacked) ratio is given in the lower panel.

117

The number of candidate SVs is found to be in good agreement between OS and SS events in most populated bins of the distribution. Overall, the number of SVs in SS events is larger than in OS events. The degree of non-closure is within the overall background uncertainty in the region of $N_{\mathrm{SV}}(\mathrm{candidate}) < 250$. The region of larger numbers of $N_{\mathrm{SV}}(\mathrm{candidate})$ contains a negligible fraction of the total events.
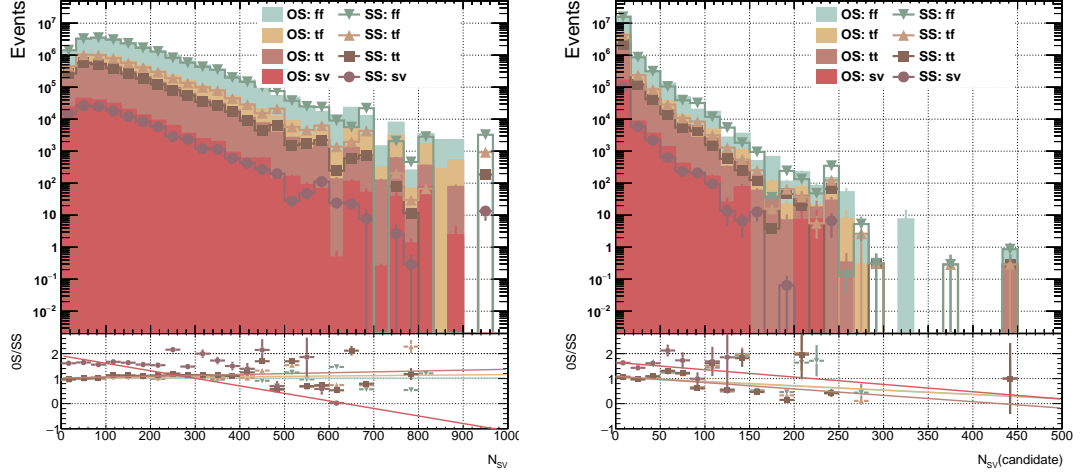
Figure 3.33: Number of SVs in SS and OS from MC simulation of background events. The event and object selection criteria are applied to the events as described in Section 3.6 upto (left) and including (right) the candidate SV selection. The background categories are: the combination of two fake tracks (ff); the combination of one true track with a fake (tf); the combination of two true tracks that do not belong to a true SV (tt). The OS to SS (stacked) ratio is given in the lower panel.

In summary, various types of background sources have been identified, and a data-driven method has been developed to reliably predict different types of background from the data. MC simulation has been employed to analyze the proportion of each background type and to conduct a closure test using MC truth information. The observed closure of the method in MC simulation serves as a robust validation of the background estimation method.

While fake tracks are the predominant source of background when considering all events, combinations of true tracks with either fake or true tracks, not originating from a true SV, are the dominant sources of background in the region of high maximum BDT classifier scores. The uncertainty for the background prediction from real secondary particles, which cannot be fully predicted with the method, is a minor source of background and is encompassed by the total uncertainty.

3.7.4 Signal Region Optimization

The goal of the signal region (SR) optimization is to maximize the significance, thus increasing the potential for the discovery of new particles. An iterative optimization procedure ensures that the chosen SR boundary achieves the highest statistical significance while avoiding fine-tuning based on the studied sample. The optimization is performed on both, $|\vec{p}_T^{\text{miss}}|$ and the maximum BDT classifier score.

The first step in defining the SRs is defining the rightmost division that becomes the left edge of the most sensitive bin up to the maximum BDT classifier value of 1. To identify that boundary the expected significance r_{s} is calculated. As the in-signal background is used in the training, and the BDT is trained on object level, the training is not conducted with cross section weights. Therefore, the ROC curves (cf. Figure 3.23) cannot be understood as a simple signal efficiency versus background rejection. The significance when each signal point has been properly weighted has to be considered together with an accurate estimate for the occurrence of background events from the SM processes. For this purpose, the BDT is evaluated for a variety of benchmark model points and in the data control region (SS SVs built in data) using the same input observable as used for the training. Figure 3.34 shows the cross section and luminosity weighted distributions of the maximum BDT classifier score per event for the bino-wino-coannihilation simplified model with a mass difference $\Delta m_0 = 1.74$ GeV, and $c\tau = 5$ mm, as well as the background prediction from SS data. The output score distributions of the number of signal events S and the expected number background events B in Figure 3.34 are fitted with interpolation functions to provide a smooth representation of the data. Using the interpolation function, a scan is performed over all possible lower thresholds on the BDT score, employing a step size ds of 0.08. The expected significance r_{s} for a given cut value on the maximum BDT output score is calculated in terms of

$$r_{\text{s}} = \frac{S}{\sqrt{S + B + dB}} \tag{3.11}$$

for different assumptions of the expected systematic uncertainty on the background method, $dB = (0.1, 0.2, 0.25, 0.3, 0.4, 0.5) \times B$. Thereby, the use of the interpolation functions allows for a more robust determination of r_{s}. The results are given in Figure 3.35. The left bin edge of the SR is determined by taking the cut value on the classifier score that results in the maximum r_{s}, provided sufficient statistical precision on the background estimation. The corresponding signal purity as a function of the cut value on the maximum BDT output score is given in Figure 3.35. It is derived from the fraction of true signal events, over the total S. In this case, true signal events are events where the maximum scoring SV matches to the signal SV at the generator level.

The procedure described above was performed for progressively stronger cuts on $|\vec{p}_T^{\text{miss}}| > (250, 350, 450, 500, 600)$. It is found that the signal to background ratio is similar for all $|\vec{p}_T^{\text{miss}}|$ bins. Therefore, a double differential binning in $|\vec{p}_T^{\text{miss}}|$ and the maximum BDT classifier score was not found to increase the significance considerably.

After determining the lower bound of the first SR bin, the second bin edge is defined such that the signal purity in that bin is above 90%. Accordingly, the signal region is split into two search bins with a of the event BDT classifier output from 0.60 to 0.65 and from 0.65 to 1. The significance r_s was calculated for several benchmark model points. In particular, it was assured that the peak r_s for the highest cross-section simplified higgsino model be contained within the SR.
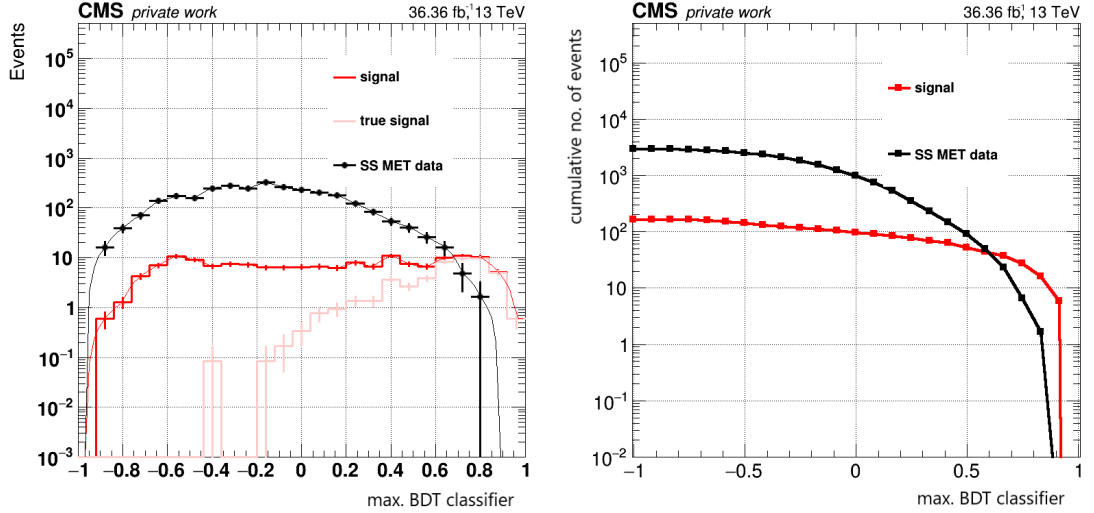
Figure 3.34: Cross section and luminosity weighted distributions of the maximum BDT classifier per event (left) and integrated for all events passing a cut at a respective classifier score (right). The bino-wino-coannihilation simplified model with a mass difference $\Delta m_0 = 1.74$ GeV, and $c\tau = 5$ mm in red, as well as the data prediction in black are evaluated. SS SVs from 36.4 fb^{-1} of the 2016 data are used for the background prediction. Signal events where the max. BDT classifier corresponds to the SV of the true signal process are given in light red.
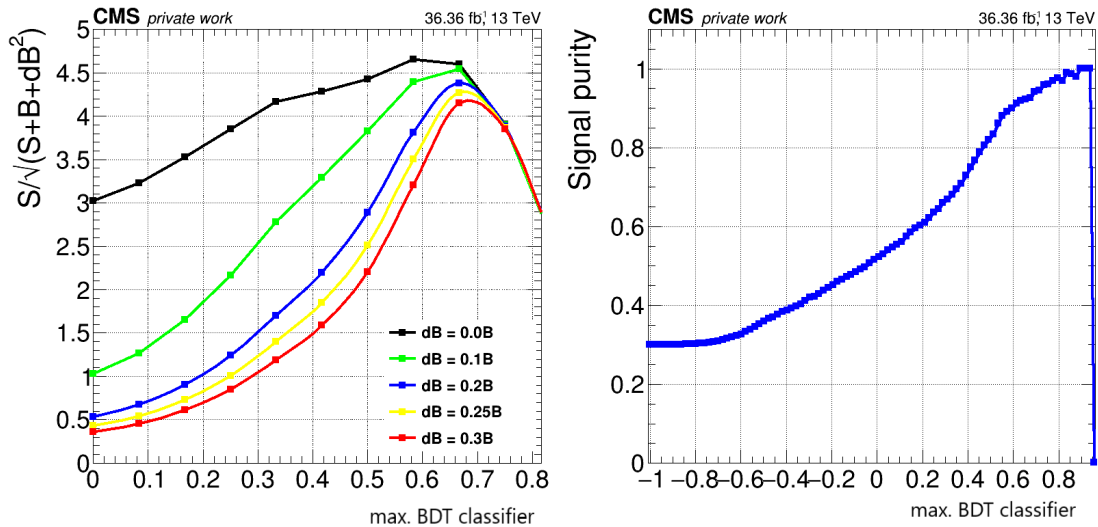
Figure 3.35: Left: Expected significance (r_s) based on the number of signal events S and the expected number of background events B for a given cut value on the maximum BDT output score. Various assumptions on the expected systematic uncertainty on the background method, $dB = (0.1, 0.2, 0.25, 0.3, 0.4, 0.5) \times B$ are compared. The bino-wino-coannihilation simplified model with a mass difference $\Delta m_0 = 1.74$ GeV, and $c\tau = 5$ mm is used as a benchmark signal model. SS SVs with 36.4 fb^{-1} of the 2016 data are used for the background prediction B. Right: Signal purity for the bino-wino-coannihilation simplified model with a mass difference $\Delta m_0 = 1.74$ GeV, and $c\tau = 5$ mm as a function of the cut value on the maximum BDT classifier score. The signal purity is the fraction of true signal SVs over the total S.

3.8 Systematic Uncertainty

Measured and predicted observables come with associated systematic uncertainties, crucial for accurate data interpretation. These uncertainties can originate from experimental factors like the muon reconstruction efficiency and theoretical aspects like the cross section uncertainty. The statistical uncertainty decreases with increasing event numbers, while the systematic uncertainty persists beyond statistical improvements. The relative statistical uncertainty of a correction systematically affects the connected distribution. This section addresses various sources of systematic uncertainty, including intrinsic uncertainties in the background estimation method and simulation-related issues affecting the expected signal efficiency. All identified sources of systematic uncertainty serve as nuisance parameters in the final result fit presented in Section 4.2.

3.8.1 Systematic Uncertainty in Background Estimation

Systematic uncertainties in the background estimation method are studied in MC. The non-closure of the background method is determined form the line fitted to the ratio

of OS over SS events versus the maximum BDT classifier score (cf. Figure 3.31). The maximum deviation of the fit line from 1 is 0.26. This maximum value of the total non-closure in all background categories summed is taken as the systematic uncertainty.

3.8.2 Systematic Uncertainty in Signal Efficiency

Systematic uncertainties also arise for the simulated MC signal. Several sources of systematic uncertainty are taken into account following standard CMS recommendations and findings of previous analysis with similar phase space [117, 119, 120]. These analyses target events with high $|\vec{p}_T^{\text{miss}}|$ as in this search. Thus, systematic uncertainties related to the hadronic component of the event are expected to be comparable. The unique feature in this analysis in regard of systematic uncertainties in the signal efficiency are the low-momentum signal tracks. However, it was shown that even the softer track in a signal pair has properties (e.g. N_{hits}, p_T) that allow for sufficient reconstruction. Therefore the standard treatment of inefficiencies related to the track reconstruction of signal tracks is adopted [117, 119, 120]. In case of different recommendations or findings, the largest stated uncertainty was taken for this analysis.

The absolute scale of the integrated luminosity is measured using van der Meer scans as discussed in Section 2.1.1. Following standard CMS recommendations for data taken in 2016, an uncertainty of 1.2% is applied to this measurement.

The 2016 data taking period is affected by an issue whereby the Level-1 trigger erroneously pre-fired on adjacent bunch crossings, prohibiting a trigger for some fraction of potential signal events. The uncertainty in the efficiency of the $|\vec{p}_T^{\text{miss}}|$ triggers is taken to be 4% [119].

A further systematic uncertainty arises from the calibration of the jet energy scale and resolution due to a time-dependent and non-uniform detector response and pileup [143]. Corrections to the jet energy scale are varied using p_T and η-dependent uncertainties, and the variations are propagated to higher level variables such as jet multiplicity, H_T^{miss}, and $|\vec{p}_T^{\text{miss}}|$ (Type-I MET correction).

A tracking inefficiency in 2016 data is caused by the unexpected saturation of photodiode signals in the tracker discussed in Section 3.3. A systematic uncertainty in the tracking efficiency of 10% in total is assumed [117].

Experimental uncertainties including the reconstruction efficiency and selection efficiency of leptons, photons, and hadronically decaying τ leptons are also incorporated. These reconstruction and selection efficiencies further translate into an uncertainty in the lepton veto efficiency of 3% [119]. Following CMS recommendations, an additional systematic uncertainty of 0.5% is assigned to the soft muon identification efficiency (cf. Section 2.4.2).

To simulate the impact of additional pile-up collisions within an event, the number of proton-proton interactions is determined using the instantaneous luminosity, relying on

a minimum-bias cross section of 69.2 mb for Run 2, accompanied by an uncertainty of 4.6% [144].

In MC simulations, the renormalization and factorization scales are adjusted to address theoretical uncertainties in parton density functions (PDFs) and matrix elements. In proton-proton collisions, PDFs model the probability to find hadron constituents (partons), namely quarks and gluons, depend on the fraction x of the proton momentum carried by the parton and the factorization scale Q^2. The renormalization scale sets the lower limit on virtualities of loop particles in the renormalized coupling definition, while the factorization scale establishes an upper limit on virtualities of partons in the PDF definition. The associated systematic uncertainty is taken to be 0.8% [119].

The systematic uncertainty regarding the SUSY production cross sections depend on the exact model point. The maximum uncertainty from all relevant model points in this analysis of 8% [145] is taken as the total uncertainty for all model points.

4 Results and Interpretation

Section 4.1 presents the observed and predicted counts for the 2016 data, corresponding to an integrated luminosity of 36.4 fb^{-1}. In Section 4.2, the observed data are interpreted in terms of the simplified higgsino model and the bino-wino coannihilation simplified model described in Section 3.3.1. The expected and observed limits for the 2016 data are shown in Section 4.2.1 alongside with the expected limits for the full Run 2 luminosity in Section 4.2.2. The latter are included to estimate the benefits of an extension of this analysis to the full Run 2 data.

4.1 Observed Data

While the analysis methods were developed without considering the OS SR in data, the unblinded data are shown in Figure 4.1. The two last bins (max. BDT classifier greater 0.6) are the SR as explained in Section 3.7.4. The figure includes the observed data in 2016 and the background prediction. A bino-wino coannihilation simplified signal model with a proper decay length of $c\tau = 5$ mm and a mass difference $\Delta m_0 = 1.17$ GeV is included to asses the signal population across the signal bins as a red line. The number of signal events where the maximum scoring SV matches to the signal SV at the generator level is given by the pink line.

The number of data events is within the combined statistical and systematic uncertainties of the number of predicted background counts, and no statistically significant deviation can be seen. The largest deviation is visible in the signal region bin with the highest sensitivity. This excess corresponds to an predicted number of background events of 13±3.61 (stat.), with an observed number of data events of 19±4.35 (stat.) and is interpreted as being in statistical agreement with the SM within the uncertainties.
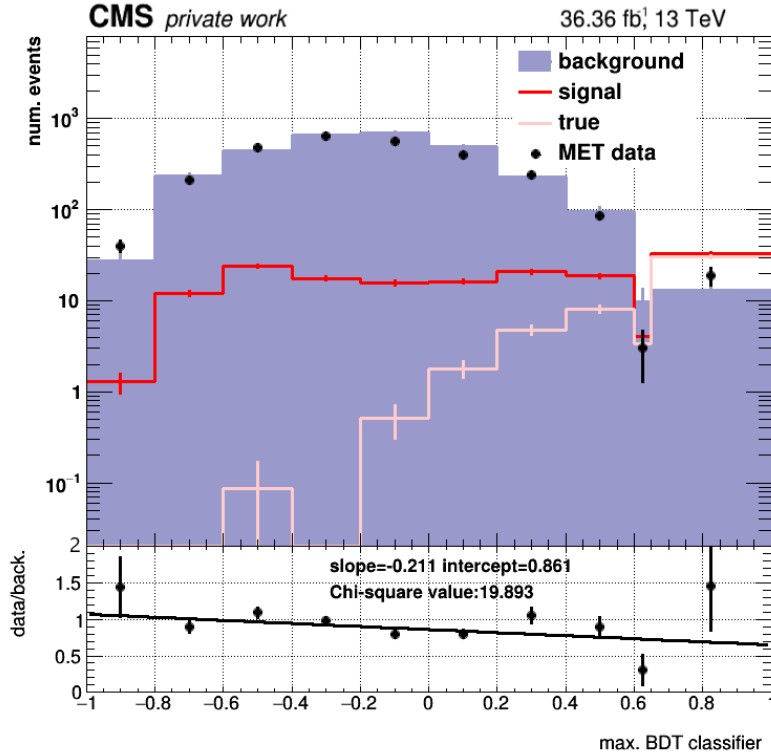
Figure 4.1: The upper panel shows the number of observed and predicted background counts from 2016 data $(36.4 \, \text{fb}^{-1})$ with the statistical uncertainties as vertical bars. The number of events form a bino-wino coannihilation simplified signal model with a proper decay length $c\tau = 5$ mm and a mass difference $\Delta m_0 = 1.17$ GeV is given as the red line and the number of true signal events for that model point as the pink line. The lower panel shows the ratio of the observed data to the background.

4.2 Interpretation

The calculation of both expected and observed limits are done using the Higgs combination tool [146]. In order to obtain both expected and observed limits, a modified frequentist approach from the standard Confidence Level (CL) technique [147, 148] at the 95% confidence level is used.

In the modified CL technique, two hypotheses are considered: the null hypothesis H_0, which assumes that only background processes contribute to the observed data, and the alternative hypothesis H_1, which posits the existence of a signal in addition to background processes. For a general test statistic q with an observed value q_{obs}, the

p-value is constructed as

$$q = -2 \ln \left(\frac{\mathcal{L}(H_1)}{\mathcal{L}(H_0)} \right) \tag{4.1}$$

where $\mathcal{L}(H_1)$ and $\mathcal{L}(H_1)$ are likelihoods associated with the alternative and null hypotheses, respectively. The key step in the CLs technique is the calculation of the CLs ratio CL_s, which is given by

$$\mathrm{CL}_s = \frac{P(q \geq q_{\mathrm{obs}}|H_1)}{P(q \geq q_{\mathrm{obs}}|H_0)} \tag{4.2}$$

If CL_s is close to 1, it suggests that the data be inconsistent with the background-only hypothesis (H_0), favoring the presence of a signal. If CL_s is close to 0, it indicates that the data are consistent with the background-only hypothesis.

A maximum likelihood fit is performed with the observed and predicted counts from data, as well as signal counts in each signal region given as input for a variety of signal model points. The systematic uncertainties discussed in Section 3.8 are included as log-normal density functions or gamma functions depending on whether the uncertainty is inherently statistical. They encode the size of the uncertainty as the width of these functions. By performing the fit and letting the nuisance parameters float, the systematic uncertainties are treated as nuisance parameters in the fit, and the post-fit distributions are obtained. Penalty terms constrain each nuisance parameter and and make use of their uncertainties. The overall experimental systematic uncertainty is dominated by the efficiency of track reconstruction in the respective data taking period and the uncertainty on the signal production cross section. All possible correlations between experimental systematic uncertainties in signal and background predictions are taken into account.

4.2.1 Results for 2016 data

In Figure 4.2, 95 % CL limits on the production cross section (σ) of $\tilde{\chi}_2^0 \, \tilde{\chi}_1^\pm$ production in the bino-wino-coannihilation model are shown as a function of Δm_0 for three life times ($c\tau$) of the $\tilde{\chi}_2^0$ (cf. Section 3.3.1). As described in Section 3.3.1, the mass of the $\tilde{\chi}_2^0$ is set to 115 GeV. The area above the curve of the observed limit is excluded. The production cross section predicted by the theoretical calculation at NLO-NLL [122, 123] is indicated in the figure as a pink solid line. With the observed upper limits, winos with a mass difference of greater or equal to 1.25 GeV to the bino LSP can be excluded. The exclusion limits are most powerful for $\tilde{\chi}_2^0$ proper decay lengths of 5 mm.

The exclusion limits derived in this analysis target mass differences that could not be reached with studies such as the CMS SOS analysis [121] (cf. Section 3.2). As the SOS analysis considers prompt identified leptons as signal signature, the search could only exclude $\tilde{\chi}_2^0$ with $\Delta m_0 \gtrsim 6$ GeV. Through the use of the secondary decay vertex of the $\tilde{\chi}_2^0$ and the relaxation of lepton identification requirements in comparison to the SOS analysis and other electroweakino DM searches [117, 149], this analysis is the first search that is able to exclude the region of 1.25 GeV $\lesssim \Delta m_0 < 2$ GeV for $\tilde{\chi}_2^0$ with a mass of 115 GeV. The exclusion limits on the electroweakino production cross sections
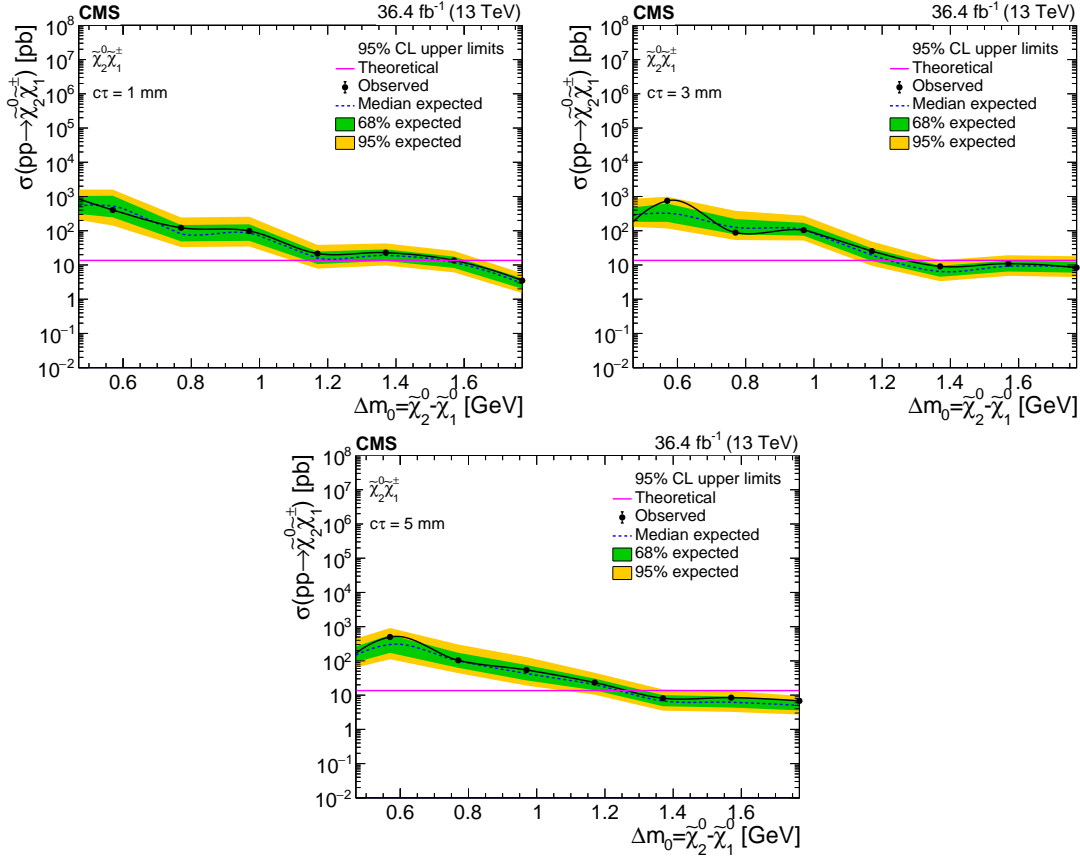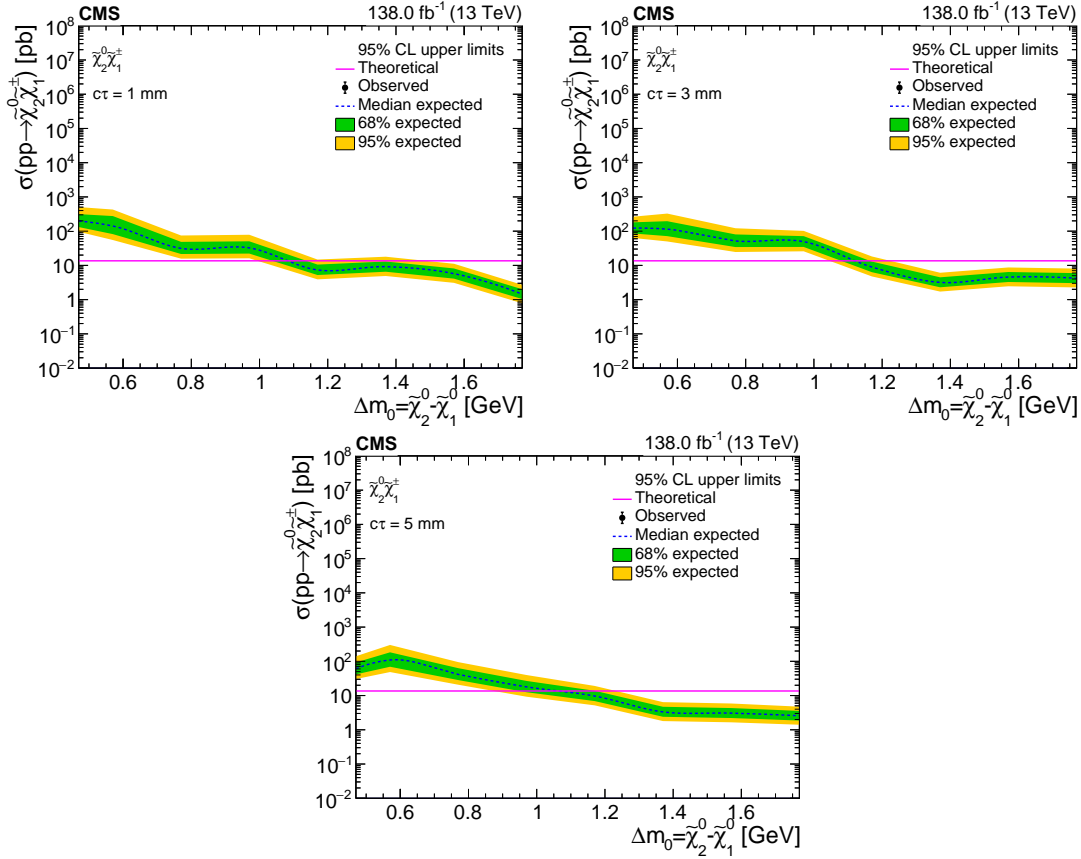
Figure 4.2: Upper 95% CL limits on the signal production cross sections (σ) in the bino-wino-coannihilation simplified model. The cross section limits are shown as a function of the mass splitting between the lightest neutralinos for a $\tilde{\chi}_2^0$ mass of 115 GeV and $c\tau = 1$ mm (top, left), $c\tau = 3$ mm (top, right) and $c\tau = 5$ mm (bottom). The black line corresponds to the observed limit using the 2016 proton-proton collision data ($L = 36.4$ fb^{-1}) at $\sqrt{s} = 13$ TeV. The pink solid line indicates the theoretical cross section of wino-like $\tilde{\chi}_2^0\,\tilde{\chi}_1^\pm$ production (cf. Section 3.3.1) [122, 123]. The green and yellow bands correspond to the 68% and 95% CL expected limits from the background prediction.

in this search can be compared with those for a pseudoscalar DM mediator from the CMS monojet analysis using the same data [119]. The latter set an upper cross section limit of about 2.8 pb for a mass of the pseudoscalar mediator of 100 GeV. Thus, the search for electroweakinos presented in this thesis can achieve a similar sensitivity as the monojet search, but for much more targeted regions of the supersymmetric parameter space.

The expected and observed limits on the production cross section of the $\tilde{\chi}_2^0$ in the simplified higgsino model are shown in Figure 4.3. The limits are shown in the plane of $\Delta m_\pm$ and the mass of the $\tilde{\chi}_1^\pm$. In the signal models, $\Delta m_\pm$ is equal to $0.5 \times \Delta m_0$. The

minimum $\Delta m_\pm$ allowed by the theoretical calculation which takes into account radiative corrections is indicated in the Figures [84]. The analysis cannot exclude regions in this plane assuming nominal production cross sections and branching fractions. However, it establishes upper limits on the cross section. Relatively stronger upper limits are seen for electroweakino masses above 130 GeV and for $\Delta m_\pm \gtrsim 1$ GeV. In comparison to models with smaller $m_{\chi^\pm}$ and $\Delta m_\pm$, signal events in this region feature objects with particularly favorable kinematics, such as larger $|\vec{p}_T^{\,\mathrm{miss}}|$ and higher-momentum displaced muons, that recoil against the leading jet. Several suggestions to further enhance the sensitivity of the analysis, especially to target more efficiently the suggested higgsino models are made in the conclusion in Chapter 5.
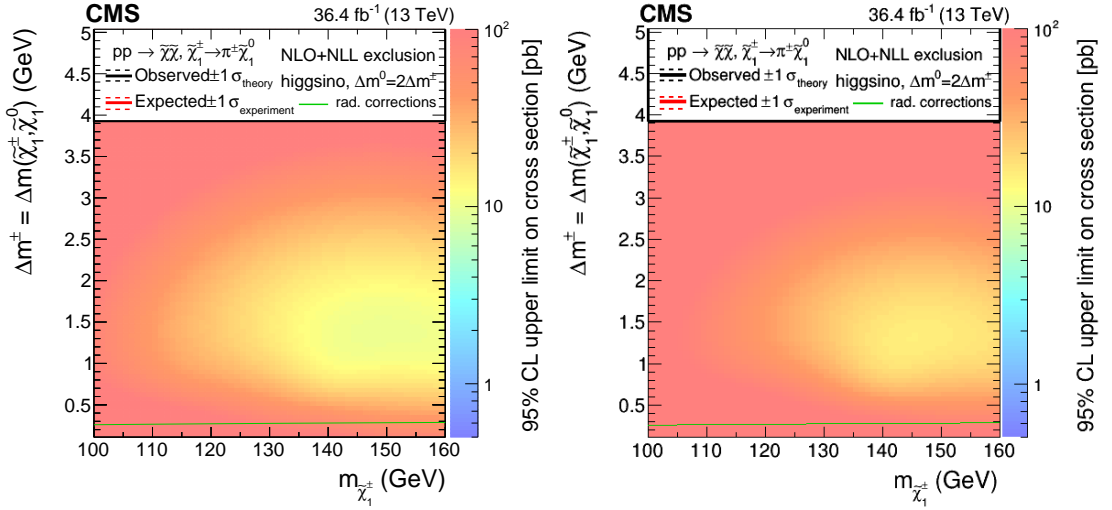
Figure 4.3: Limits on the production cross section of the $\tilde{\chi}_2^0$ in the simplified higgsino model. The expected cross section limits (left) and the observed limits using the 2016 proton-proton collision data ($L = 36.4$ fb^{-1}) at $\sqrt{s} = 13$ TeV (right) are shown in the plane of $\Delta m_\pm$ and mass of the $\tilde{\chi}_1^\pm$. The color-coded z-axis shows the upper limits on the cross section. The green solid line indicates the minimum $\Delta m_\pm$ allowed by theoretical calculation which take into account radiative corrections [84].

4.2.2 Expected Limits for Run 2

The expected limits are extrapolated to the Run 2 luminosity of 138 fb^{-1} via a $\sqrt{L}$-scaling. Results are shown in Figure 4.4. To obtain a signal and background prediction, the expected signal yield and the background along with the corresponding uncertainties for the 2016 data is scaled to account for the higher luminosity.

As in the previous section, 95 % CL limits on the expected production cross section of the $\tilde{\chi}_2^0$ in the bino-wino-coannihilation simplified model are shown as a function of Δm_0 and for the three life times of the $\tilde{\chi}_2^0$. In comparison to Figure 4.2, the sensitivity of the search expands to smaller Δm_0. With the luminosity of 138 fb^{-1} collected in Run

2, the region of wino-like $\tilde{\chi}_2^0$ with a mass differences of $\Delta m_0 \gtrsim 1.1$ GeV to the bino-like LSP is expected to be excluded. This improvement is mainly through the reduction in the statistical uncertainty of the signal and background predictions. However, the systematic uncertainties are the larger limiting factor to the sensitivity of the analysis. With improvements on the systematic uncertainties on the background prediction and signal efficiency, the excluded region may become much larger. Improvements in the sensitivity towards lower Δm_0 are also limited through the reconstruction efficiency for low-momentum tracks and muons at the CMS detector. Therefore, a relatively small improvement in the sensitivity through the higher luminosity is expected.

Figure 4.4: Expected 95% CL upper limits on the signal production cross sections (σ) in the bino-wino-coannihilation simplified model for the full Run 2 luminosity of 138 fb^{-1}. The cross section limits are shown as a function of the mass splitting between the lightest neutralinos for a $\tilde{\chi}_2^0$ mass of 115 GeV and $c\tau = 1$ mm (top, left), $c\tau = 3$ mm (top, right) and $c\tau = 5$ mm (bottom). The pink solid line indicates the theoretical cross section of wino-like $\tilde{\chi}_2^0 \tilde{\chi}_1^\pm$ production (cf. Section 3.3.1) [122, 123]. The green and yellow bands correspond to the 68% and 95% CL expected limits from the background prediction.

The expected limits on the production cross section of the $\tilde{\chi}_2^0$ for the full Run 2 luminosity

in the pure higgsino simplified model are shown in Figure 4.5. As in the previous section, the limits are shown in the plane of $\Delta m_\pm$ and mass of the $\tilde{\chi}_1^\pm$. The minimum $\Delta m_\pm$ allowed by the theoretical calculation is indicated in the Figures [84]. As can be seen from the figures, the analysis can potentially exclude electroweakinos with masses of about 140 GeV and $\Delta m_\pm \approx 1.3$ GeV. This analysis is thus anticipated to exclude mass splittings below the previous exclusion limits set at CMS in the SOS analysis, which was described in Section 3.2. In addition, it adds sensitivity in the region where the ATLAS searches for chargino-neutralino pair production using final states with two or three leptons [114, 115] presented in Section 3.2, are not sensitive. In these searches an exclusion down to $\Delta m_\pm = 2$ GeV was achieved.
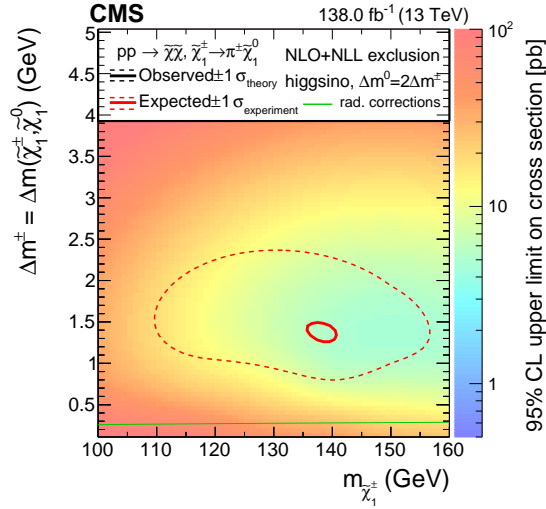
Figure 4.5: Expected limits on the production cross section of the $\tilde{\chi}_2^0$ in the pure higgsino simplified model for the full Run 2 luminosity of 138 fb^{-1}. The expected cross section limits are shown in the plane of $\Delta m_\pm$ and mass of the $\tilde{\chi}_1^\pm$. The area inside the red curves can be excluded at the 95% CL (solid line) with a 1σ variation in the systematic uncertainties (dashed line). The color-coded z-axis shows the upper limits on the cross section. The green solid line indicates the minimum $\Delta m_\pm$ allowed by the theoretical calculation which take into account radiative corrections [84].

5 Conclusion and Outlook

This thesis presents a search for compressed mass electroweakino production with low-momentum muon tracks using data taken by the CMS experiment. This investigation is part of a broader initiative aimed at identifying a viable dark matter particle. The motivation for considering the existence of dark matter stems from compelling astrophysical evidence. The proposed dark matter candidates in the context of this thesis are higgsino- and bino-like neutralinos, interpreted within the scope of simplified models. These models are motivated as they provide a suitable WIMP dark matter candidate and serve as a natural supersymmetric extension of the SM.

The search targets a dark matter candidate in a final state resulting from the decay of a long-lived second lightest neutralino ($\tilde{\chi}_2^0$), a phenomenon arising in supersymmetric models in the case of a small mass difference between the two lightest new particles. Specifically, the analysis focuses on an unexplored phase space characterized by muons with transverse momenta below 5 GeV, which are displaced from the primary interaction vertex. This unique phase space region has not been covered well in prior searches. Enhanced sensitivity in this regime is achieved by relaxing muon identification criteria and allowing for one of the two muons to just being measured as a track without being identified as a muon. To accommodate such low-momentum muons and tracks, a specialized secondary vertex reconstruction method is employed to reconstruct the decay vertex of the neutralino. Additionally, the use of multivariate discriminants increases the sensitivity of the analysis.

The efficient and large-coverage CMS muons systems, along with the precise silicon tracking detector, appropriately capture this signature. In the 2016 data, the results are statistically compatible with the background-only prediction, and upper 95% CLs limits on the neutralino production cross sections and masses are presented using 36.36 fb^{-1} of proton-proton collision data at $\sqrt{s} = 13$ TeV. These limits constrain the so far unexplored targeted region of the phase space, particularly for an LSP mass of 115 GeV, where mass differences between the neutralinos above 1.25 GeV are excluded.

Projected limits for the entire Run 2 luminosity underline the potential of this search to explore even lower values of Δm_0. From the additional luminosity when using all of the Run 2 data, $\tilde{\chi}_2^0$ with a mass of 115 GeV and Δm_0 of above 1.1 GeV are expected to be excluded. With the installation of the Phase 1 tracking detector after

2016, an improvement in the transverse momentum resolution and secondary vertex reconstruction is observed. This is expected to further enhance the potential sensitivity of this analysis when extended to the full Run 2 data set. Since the dominant limiting factor in the sensitivity of the analysis are systematic uncertainties, these improvements are expected to have an even stronger beneficial effect on the sensitivity of the analysis.

In an extension of this search, the sensitivity to the signal process with a nearly-mass-degenrate higgsino-like LSPs could be enhanced by training a multivariate classifier to specifically target the higgsino events, which have less favorable kinematics than the bino-wino-coannihilation model. The accuracy of the background prediction method could be refined by a dedicated treatment of the background from true secondary vertices, potentially reducing systematic uncertainty. This can be achieved for example by a prediction of the background from true low-mass resonances from simulation. Moreover, conservative assumptions have been made regarding uncertainties on the signal efficiency, which could be minimized through reliable studies on the simulation of soft tracks from pile-up, the underlying event, and fake tracks, particularly with the Fast Simulation (cf. Section 3.3.1). Utilizing K_s for improvements on the estimation of the track and vertex reconstruction efficiency for signal should be considered. Although K_s decay mainly into two pions, the properties of the tracks of those soft pions are similar to the tracks of soft signal muons.

Ultimately, the combination of this analysis with searches for $\tilde{\chi}_2^0$ with even smaller mass differences and larger masses, such as searches for $\tilde{\chi}_2^0$ in final states with prompt leptons [150, 149], and disappearing tracks [118] could achieve a full coverage of the targeted phase space. Thereby, it will be possible to find an answer to the question if natural supersymmetric models can provide a suitable dark matter candidate.

In conclusion, this search successfully demonstrates an approach to discovering new long-lived particles and dark matter using advanced vertexing techniques and a data-driven background estimation. In a broader context, this analysis underscores the significance and potential in exploring dark matter-related signatures previously beyond reach at the LHC. The discovery of such signatures could fundamentally reshape our comprehension of particle physics and cosmology and mark a scientific milestone in unraveling the remaining mysteries surrounding the nature of dark matter and its role in the universe.

A Appendix

Performance of the V0 Fitter

This section contains additional figures, referred to in Section 2.3.2.1. Figure A.1 shows the mean invariant mass of K_s^0 (Λ^0) particles reconstructed from oppositely-charged pion (and proton) candidates in data. The difference between the expected mass of the K_s^0 (Λ^0) particles and the measurement, as well as the difference between the reconstructed mass in MC simulation and data as functions of p_T, ϕ, and the decay length are evidence for the great resolution of the V0 Fitter over large regions of the phase space.
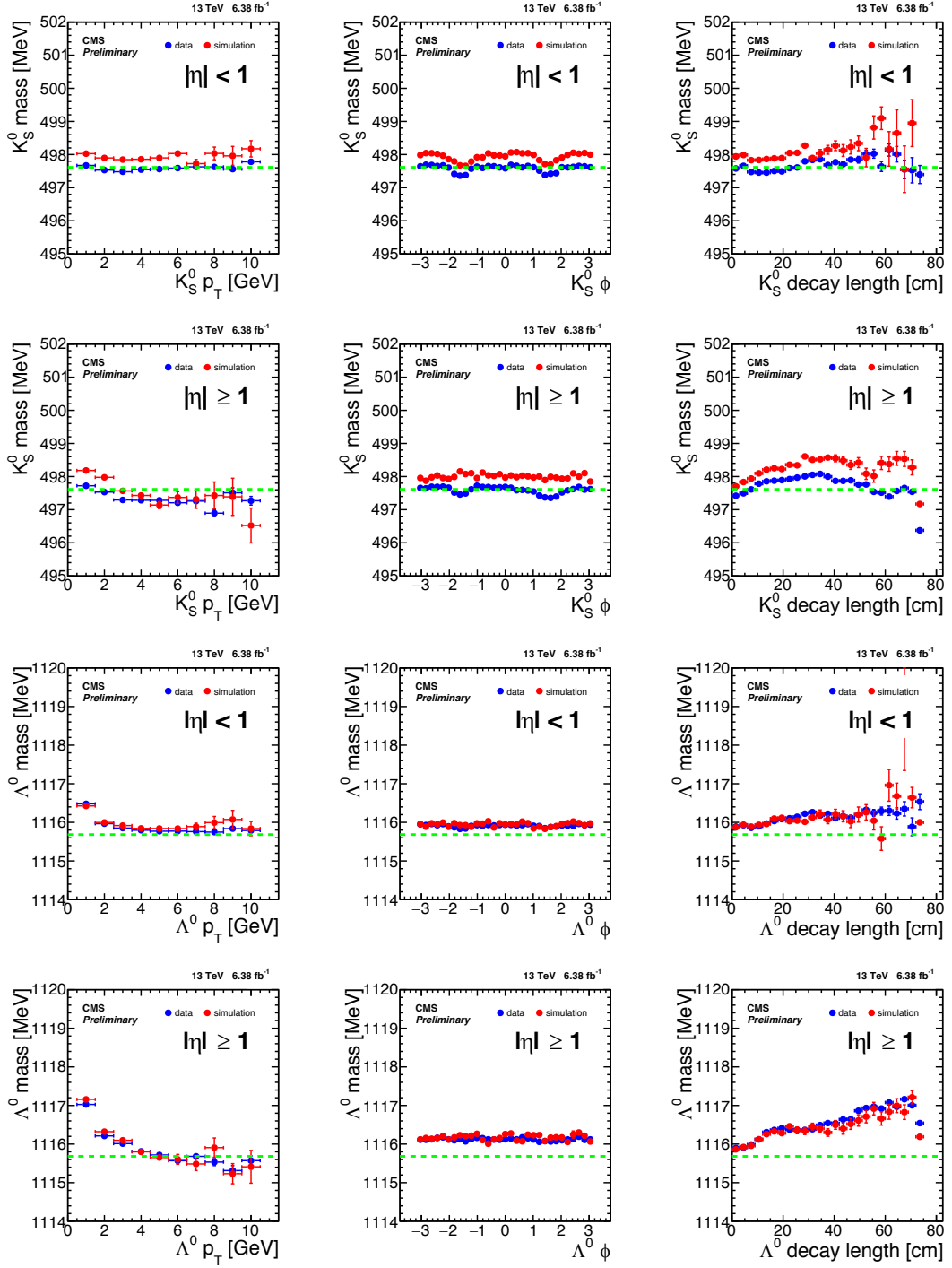
Figure A.1: Invariant mass of K_s^0 (top two rows) and Λ^0 (bottom two rows) particles as a function of p_T, ϕ, and the decay length from data (blue points) and MS simulation (red points) inside the central ($|\eta| < 1$) and forward ($|\eta| \geq 1$) regions. The decay length is the 3D distance from the vertex of the K_s^0 (Λ^0) to the nearest primary vertex. The expected mass of the K_s^0 (Λ^0) particles is contained in the plot (dashed green line). To obtain these figures, the $V0$ Fitter described in Section 2.3.2.1 is used [106].

Soft Muon Tag

This section contains additional figures, referred to in Section 3.6.3. Figure A.2 shows additional characteristics of the soft displaced muon candidate signal and SM MC background events, such as the number of muon stations, pixel layers and muon chambers associated to the muon.
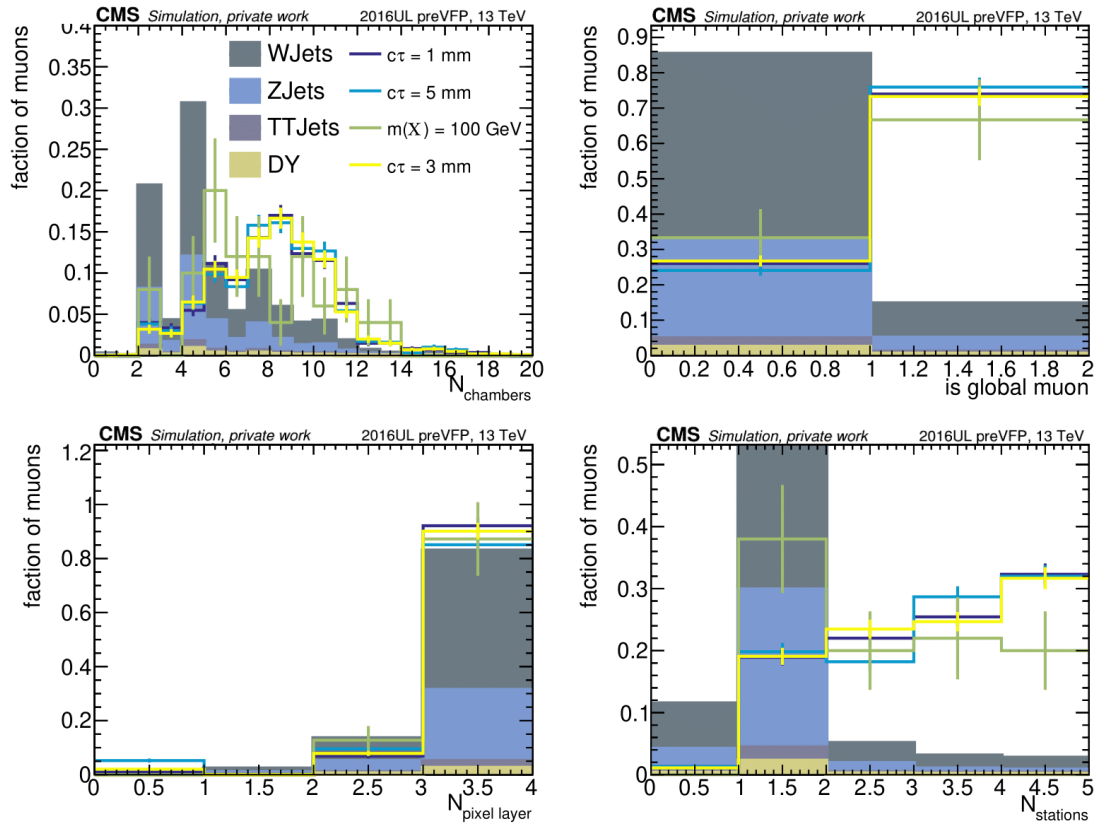
Figure A.2: Characteristics of soft muons in generator-level true signal muon-track pairs and reconstructed muon-track pairs from SM MC background events. Four example signal mass points as are shown as colored lines: the bino-wino coannihilation simplified model with a $\Delta m_0 = 1.17$ GeV and three different lifetimes along with the simplified nearly-pure higgsino model with a $\Delta m_0 = 0.32$ GeV. The GEANT4-based simulation of events is shown for the background as colored filled areas divided into different SM processes. All events have to pass the monojet selection as described in Section 3.6.2. Moreover events have to have at least one SV.

FastSim to FullSim Comparison for Signal

This section contains additional figures, referred to in Section 3.6.3.6. The Figures A.3 to A.9 show kinematic distributions for signal events with low momentum displaced tracks. For two exemplary signal model points, each variable is shown from signal events simulated using FASTSIM, as in the main part of this analysis, in comparison to the same model point simulated with the comprehensive CMS detector simulation employing the GEANT4 toolkit (FULLSIM) (cf. Section 3.1). The distributions are shown with PU weights to have matching PU conditions in the FULLSIM simulated signal samples and the FASTSIM simulated signal samples. Overall, there is no significant deviation between the two simulation modes for the relevant variables. More information on the performance of FASTSIM in general can be found in [151], and for the specific application of FASTSIM for signal simulation with soft displaced signal tracks in [150].
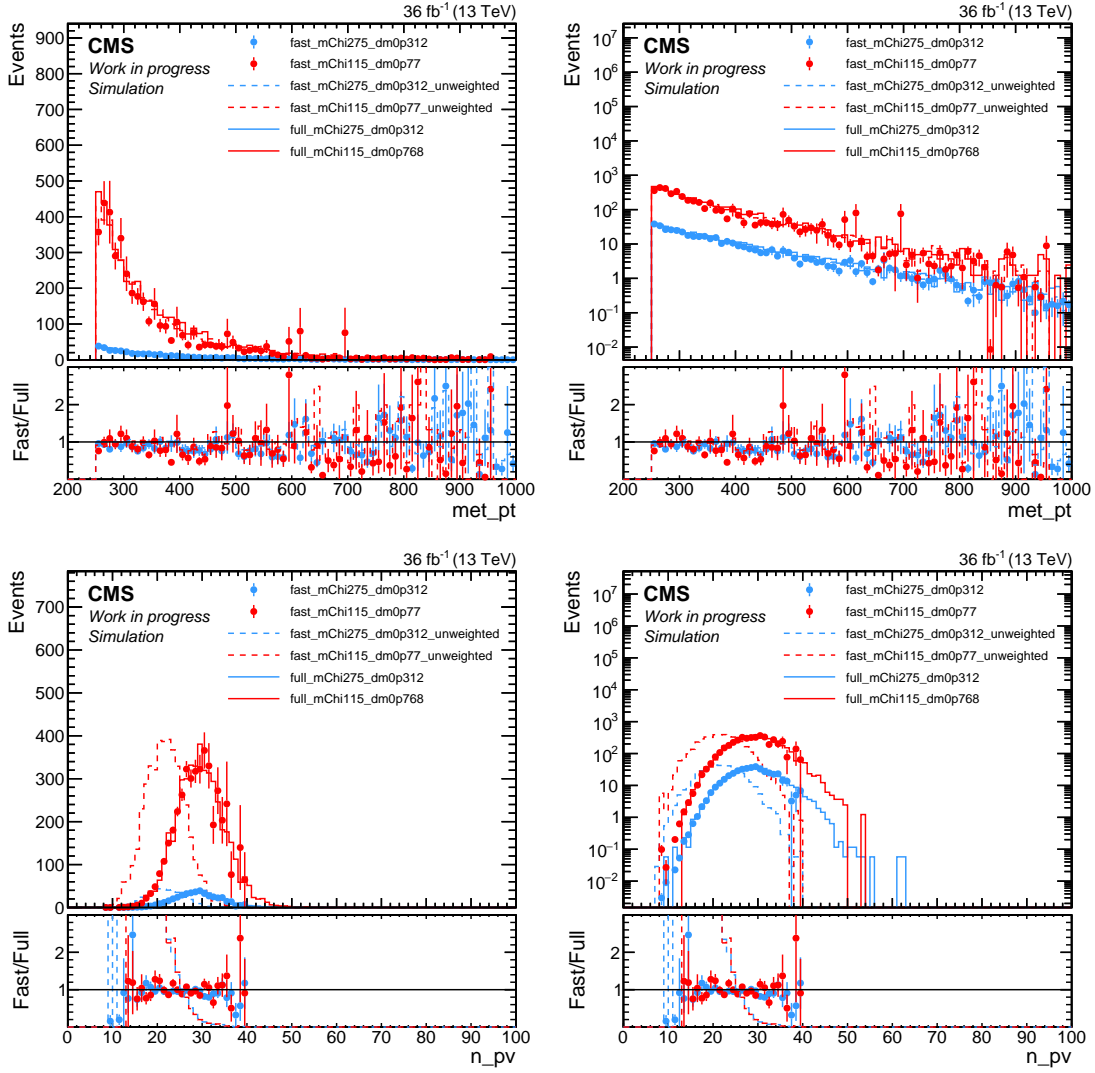
Figure A.3: Distributions of $p_T^{Miss.}$ (met_pt), and the number of pile-up vertices (n_pv) for signal events with low momentum displaced tracks from two exemplary signal model point in red and blue. Each variable is shown from signal events simulated using FASTSIM as dots, as in the main part of this analysis, in comparison to the same model point simulated with the comprehensive CMS detector simulation employing the GEANT4 toolkit, FULLSIM, (cf. Section 3.1) as solid lines. The dashed lines represent the respective distributions without the PU weights. The ratio panel shows the ratio of (unweighted) FASTSIM to FULLSIM events as dots (dashed lines) for the two signal models [150].
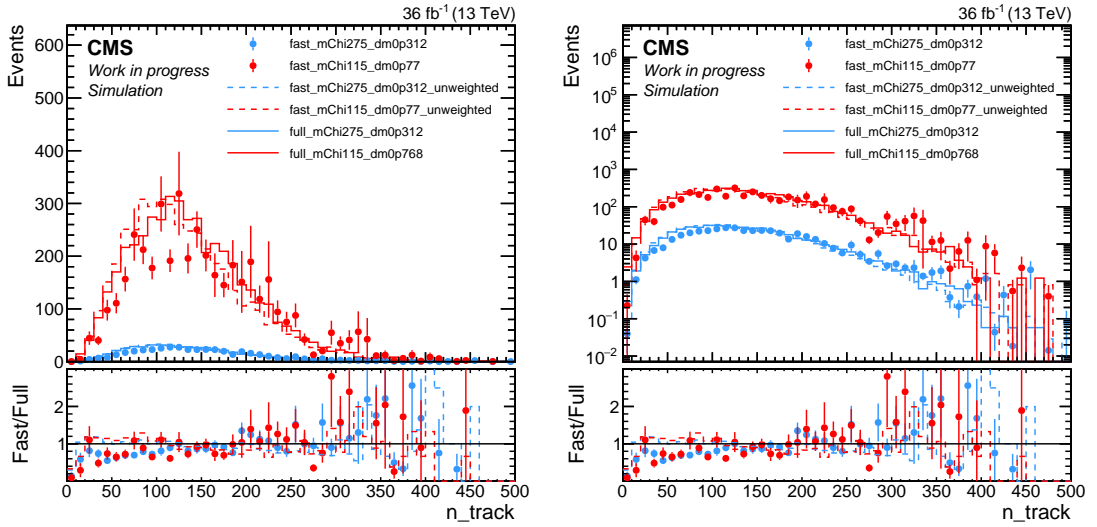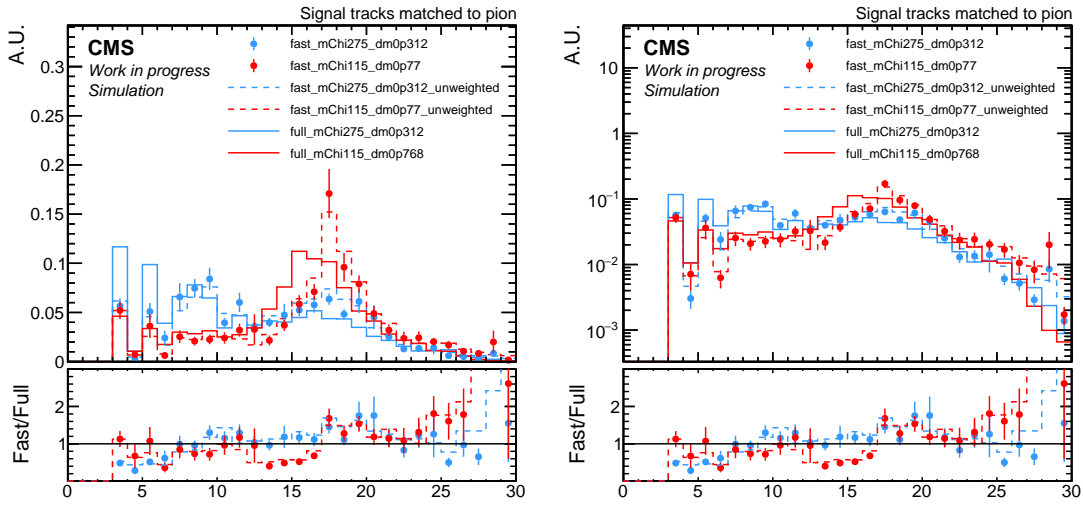
Figure A.4: Distribution of the number of tracks (n_track) for signal events with low momentum displaced tracks from two exemplary signal model point in red and blue. Each variable is shown from signal events simulated using FASTSIM as dots, as in the main part of this analysis, in comparison to the same model point simulated with the comprehensive CMS detector simulation employing the GEANT4 toolkit, FULLSIM, (cf. Section 3.1) as solid lines. The dashed lines represent the respective distributions without the PU weights. The ratio panel shows the ratio of (unweighted) FASTSIM to FULLSIM events as dots (dashed lines) for the two signal models [150].
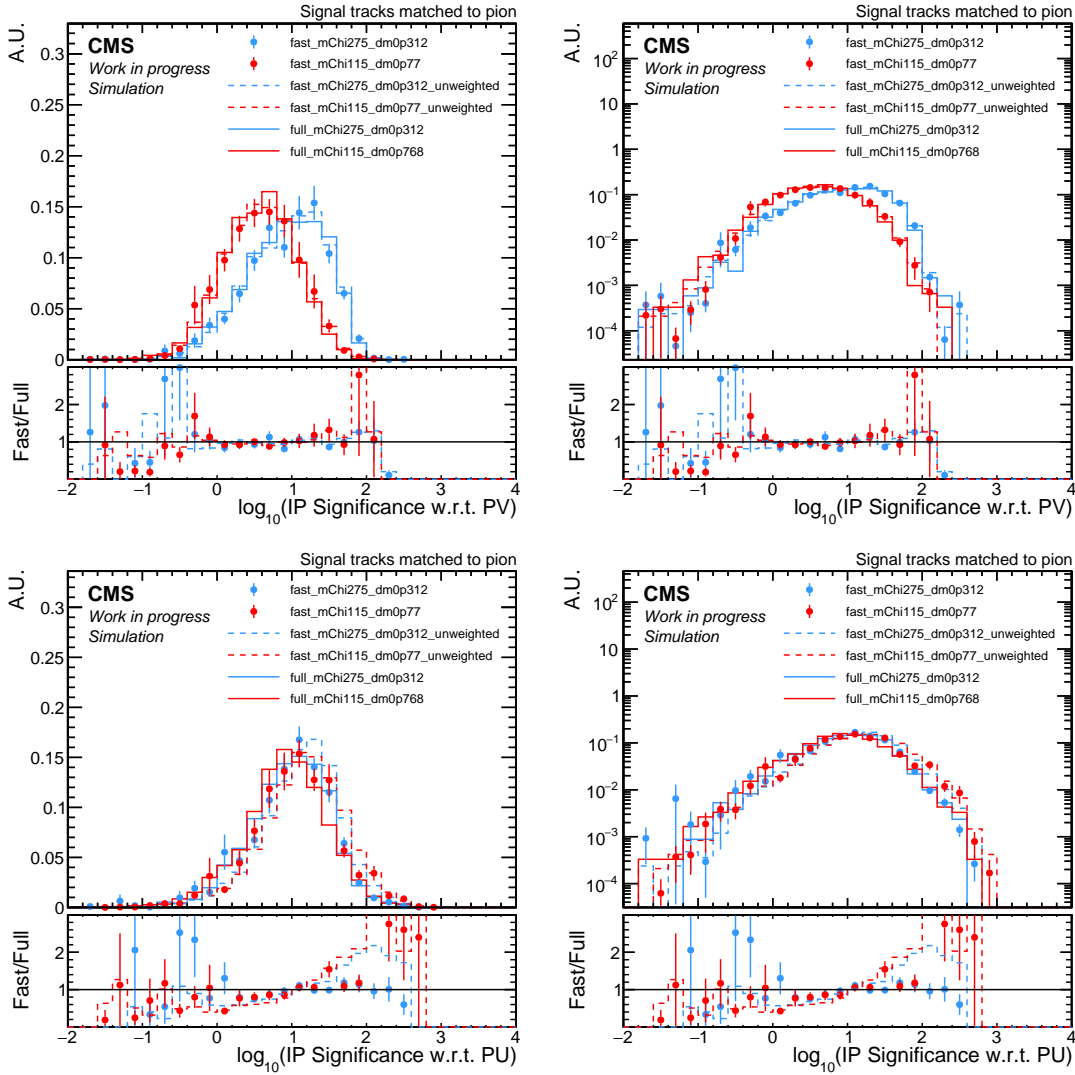
Figure A.5: Distributions of IP significance with respect to the PV and the nearest PU vertex for signal events with low momentum displaced tracks from two exemplary signal model points in red and blue. Each variable is shown from signal events simulated using FASTSIM as dots, as in the main part of this analysis, in comparison to the same model point simulated with the comprehensive CMS detector simulation employing the GEANT4 toolkit, FULLSIM, (cf. Section 3.1) as solid lines. The dashed lines represent the respective distributions without the PU weights. The ratio panel shows the ratio of (unweighted) FASTSIM to FULLSIM events as dots (dashed lines) for the two signal models [150]
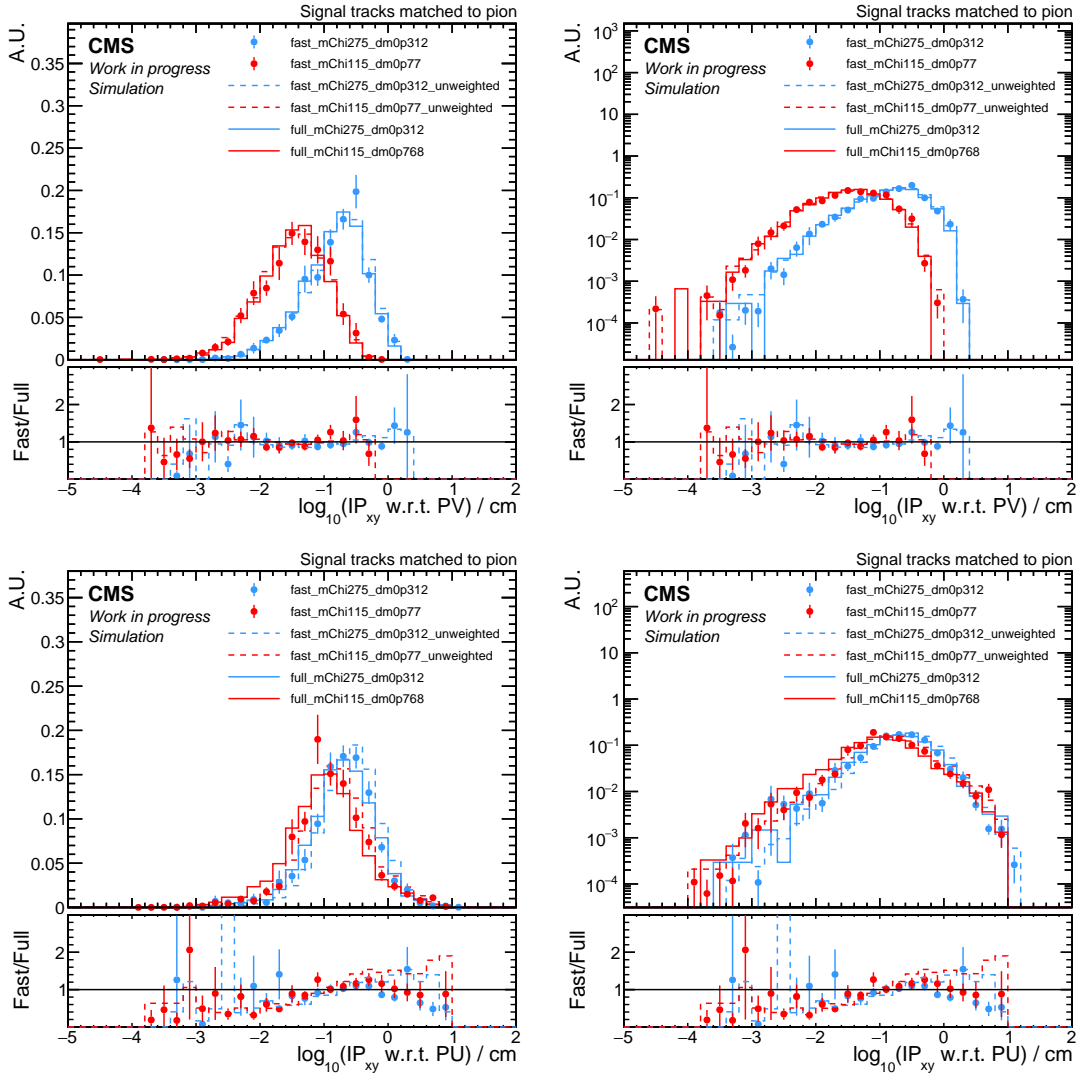
Figure A.6: Distributions of the longitudinal impact parameter with respect to the PV and the nearest PU vertex for signal events with low momentum displaced tracks from two exemplary signal model points in red and blue. Each variable is shown from signal events simulated using FASTSIM as dots, as in the main part of this analysis, in comparison to the same model point simulated with the comprehensive CMS detector simulation employing the GEANT4 toolkit, FULLSIM, (cf. Section 3.1) as solid lines. The dashed lines represent the respective distributions without the PU weights. The ratio panel shows the ratio of (unweighted) FASTSIM to FULLSIM events as dots (dashed lines) for the two signal models [150].

Figure A.7: Distributions of the transverse impact parameter with respect to the PV and the nearest PU vertex for signal events with low momentum displaced tracks from two exemplary signal model points in red and blue. Each variable is shown from signal events simulated using FastSim as dots, as in the main part of this analysis, in comparison to the same model point simulated with the comprehensive CMS detector simulation employing the Geant4 toolkit, FullSim, (cf. Section 3.1) as solid lines. The dashed lines represent the respective distributions without the PU weights. The ratio panel shows the ratio of (unweighted) FastSim to FullSim events as dots (dashed lines) for the two signal models [150].

Figure A.8: Distributions of the p_T, and η for low momentum displaced signal tracks from two exemplary signal model points in red and blue. Each variable is shown from signal events simulated using FASTSIM as dots, as in the main part of this analysis, in comparison to the same model point simulated with the comprehensive CMS detector simulation employing the GEANT4 toolkit, FULLSIM, (cf. Section 3.1) as solid lines. The dashed lines represent the respective distributions without the PU weights. The ratio panel shows the ratio of (unweighted) FASTSIM to FULLSIM events as dots (dashed lines) for the two signal models [150].

Figure A.9: Distributions of the number of valid hits for low momentum displaced signal tracks from two exemplary signal model points in red and blue. The variable is shown from signal events simulated using FASTSIM as dots, as in the main part of this analysis, in comparison to the same model point simulated with the comprehensive CMS detector simulation employing the GEANT4 toolkit, FULLSIM, (cf. Section 3.1) as solid lines. The dashed lines represent the respective distributions without the PU weights. The ratio panel shows the ratio of (unweighted) FASTSIM to FULLSIM events as dots (dashed lines) for the two signal models [150].

Bibliography

[1] H. Renz-Polster, *Kinder verstehen: Born to be wild.* Kösel, 2009.

[2] Planck Collaboration, "Planck 2018 results. vi. cosmological parameters," *Astronomy Astrophysics*, vol. 641, p. A6, 2020.

[3] W. L. Freedman, B. F. Madore, D. Hatt, T. Hoyt, I. S. Jang, R. L. Beaton, *et al.*, "The carnegie-chicago hubble program. viii. an independent determination of the hubble constant based on the tip of the red giant branch," *The Astrophysical Journal*, vol. 882, no. 1, p. 34, 2019.

[4] W. Chen and G. J. Wasserburg, "The isotopic composition of lead in the earth's oldest rocks," *Earth and Planetary Science Letters*, vol. 62, no. 2, pp. 167–185, 1981.

[5] S. A. Wilde, J. W. Valley, W. H. Peck, and C. M. Graham, "Evidence from detrital zircons for the existence of continental crust and oceans on the earth 4.4 gyr ago," *Nature*, vol. 409, no. 6817, pp. 175–178, 2001.

[6] C. Stringer, "The origin and evolution of homo sapiens," *Philosophical Transactions of the Royal Society B: Biological Sciences*, vol. 371, no. 1698, p. 20150237, 2016.

[7] T. Higham, K. Douka, R. Wood, C. B. Ramsey, F. Brock, L. Basell, *et al.*, "The timing and spatiotemporal patterning of neanderthal disappearance," *Nature*, vol. 512, no. 7514, pp. 306–309, 2014.

[8] R. Largo, *Babyjahre: die frühkindliche Entwicklung aus biologischer Sicht : das andere Erziehungsbuch.* Serie Piper, Piper, 1998.

[9] V. S. Butler, "Dark matters," *Fermi News*, vol. 21N5, pp. 8–9, 1998.

[10] D. N. Spergel, "The dark side of cosmology: Dark matter and dark energy," *Science*, vol. 347, pp. 1100–1102, 2015.

[11] K. Garrett and G. Duda, "Dark matter: A primer," *Advances in Astronomy*, vol. 2011, pp. 1–22, 2011.

[12] V. Trimble, "Existence and nature of dark matter in the universe," *Annual Review of Astronomy and Astrophysics*, vol. 25, no. 1, pp. 425–472, 1987.

[13] A. Kohn and C. Kolarik, *Liebe und Eigenständigkeit: die Kunst bedingungsloser Elternschaft, jenseits von Belohnung und Bestrafung.* Arbor-Verlag, 2010.

[14] T. Berners-Lee, "Information management: A proposal," tech. rep., CERN, 1990.

[15] National Research Council (US) Committee to Update Science, Medicine, and Animals, *Science, Medicine, and Animals.* Washington, DC: National Academies Press (US), 2004. The Concept of Basic Research.

[16] A. Einstein, *The Human Side: Glimpses from His Archives.* Princeton, NJ: Princeton University Press, 1979.

[17] G. Bertone, *Particle Dark Matter: Observations, Models and Searches.* Cambridge Monographs on Particle Physics, Nuclear Physics and Cosmology, Cambridge University Press, 2010.

[18] S. P. Martin, "A Supersymmetry Primer," *hep-ph/9709356*, Sep 1997. `http://cds.cern.ch/record/334060`.

[19] M. Peskin and D. Schroeder, *An Introduction To Quantum Field Theory.* Frontiers in Physics, Avalon Publishing, 1995.

[20] L. Ryder, *Quantum Field Theory.* Cambridge University Press, 1996.

[21] D. Griffiths, *Introduction to Elementary Particles.* Physics textbook, Wiley, 2008.

[22] S. Chatrchyan *et al.*, "Observation of a new boson at a mass of 125 GeV with the CMS experiment at the LHC," *Phys. Lett.*, vol. B716, pp. 30–61, 2012.

[23] G. Aad *et al.*, "Observation of a new particle in the search for the Standard Model Higgs boson with the ATLAS detector at the LHC," *Phys. Lett.*, vol. B716, pp. 1–29, 2012.

[24] R. L. Workman *et al.*, "Review of Particle Physics," *PTEP*, vol. 2022, p. 083C01, 2022.

[25] D. Kestenbaum, "What is electroweak symmetry breaking anyway?," *Fermi News*, vol. 21N2, p. 1, 1998.

[26] P. W. Higgs, "Broken Symmetries and the Masses of Gauge Bosons," *Phys. Rev. Lett.*, vol. 13, pp. 508–509, 1964.

[27] P. W. Higgs, "Broken symmetries, massless particles and gauge fields," *Phys. Lett.*, vol. 12, pp. 132–133, 1964.

[28] F. Englert and R. Brout, "Broken Symmetry and the Mass of Gauge Vector Mesons," *Phys. Rev. Lett.*, vol. 13, pp. 321–323, 1964.

[29] G. S. Guralnik, C. R. Hagen, and T. W. B. Kibble, "Global conservation laws and massless particles," *Phys. Rev. Lett.*, vol. 13, pp. 585–587, Nov 1964.

[30] P. W. Higgs, "Spontaneous Symmetry Breakdown without Massless Bosons," *Phys. Rev.*, vol. 145, pp. 1156–1163, 1966.

[31] W. A. Bardeen, C. T. Hill, and M. Lindner, "Minimal Dynamical Symmetry Breaking of the Standard Model," *Phys. Rev.*, vol. D41, p. 1647, 1990.

[32] Nobelprize.org, "The Nobel Prize in Physics 2013 - Press Release," 2014. `http://www.nobelprize.org/nobel_prizes/physics/laurates/2013/press.html`,Accessed: 28 February, 2023.

[33] M. E. Peskin and D. V. Schroeder, *An Introduction to Quantum Field Theory.* Westview Press, 1995.

[34] M. Gell-Mann, "Symmetries of Baryons and Mesons," *Physical Review*, vol. 125, no. 4, pp. 1067–1084, 1962.

[35] J. Ellis, M. K. Gaillard, and D. V. Nanopoulos, "A Historical Profile of the Higgs Boson. An Updated Historical Profile of the Higgs Boson," p. 22, Apr 2015.

[36] N. Schmitz, "The discovery of neutrino masses," in *Correlations and Fluctuations in QCD*, world scientific, Sep 2003.

[37] P. Minkowski, "$\mu \to e\gamma$ at a rate of one out of 10^9 muon decays?," *Physics Letters B*, vol. 67, no. 4, pp. 421–428, 1977.

[38] K. Zuber, *Neutrino Mass and Mixing: From Theory to Experiment.* Springer, 2012.

[39] S. R. Elliott and J. Engel, "Neutrinoless double-beta decay: Status and prospects," *Journal of Physics G: Nuclear and Particle Physics*, vol. 30, no. 9, p. R183, 2004.

[40] G. 't Hooft, C. Itzykson, A. Jaffe, H. Lehmann, P. K. Mitter, I. M. Singer, and R. Stora, "Recent developments in gauge theories," *NATO Sci. Ser. B*, vol. 59, pp. 1–438, 1980.

[41] A. Deur, S. J. Brodsky, and G. F. de Teramond, "The QCD Running Coupling," *Prog. Part. Nucl. Phys.*, vol. 90, pp. 1–74, 2016.

[42] H. Georgi and S. L. Glashow, "Unity of All Elementary Particle Forces," *Phys. Rev. Lett.*, vol. 32, pp. 438–441, 1974.

[43] G. W. Bennett *et al.*, "Final report of the e821 muon anomalous magnetic moment measurement at bnl," *Physical Review D*, vol. 73, no. 7, p. 072003, 2006.

[44] G. Venanzoni, "New results from the Muon g-2 Experiment," in *2023 European Physical Society Conference on High Energy Physics* , 11 2023.

[45] A. Keshavarzi, K. S. Khaw, and T. Yoshioka, "Muon g2: A review," *Nuclear Physics B*, vol. 975, p. 115675, 2022.

[46] E. Corbelli and P. Salucci, "The extended rotation curve and the dark matter halo of m33," *Monthly Notices of the Royal Astronomical Society*, vol. 311, pp. 441–447, jan 2000.

[47] K. Blundell, *The Big Bang: A Very Short Introduction*. Oxford University Press, 2013.

[48] A. H. Guth, "The Inflationary Universe: A Possible Solution to the Horizon and Flatness Problems," *Phys. Rev. D*, vol. 23, pp. 347–356, 1981.

[49] B. W. Carroll and D. A. Ostlie, *An Introduction to Modern Astrophysics*. Addison-Wesley, 2007.

[50] A. G. Riess *et al.*, "Observational evidence from supernovae for an accelerating universe and a cosmological constant," *The Astronomical Journal*, vol. 116, no. 3, pp. 1009–1038, 1998.

[51] G. Hinshaw, D. Larson, E. Komatsu, D. N. Spergel, C. L. Bennett, J. Dunkley, *et al.*, "Nine-year wilkinson microwave anisotropy probe (wmap) observations: Cosmological parameter results," *The Astrophysical Journal Supplement Series*, vol. 208, no. 2, p. 19, 2013.

[52] S. Weinberg, *The First Three Minutes: A Modern View of the Origin of the Universe*. Basic Books, 1977.

[53] S. Perlmutter, G. Aldering, G. Goldhaber, R. A. Knop, P. Nugent, P. G. Castro, S. Deustua, *et al.*, "Observational evidence from supernovae for an accelerating universe and a cosmological constant," *The Astrophysical Journal*, vol. 517, no. 2, pp. 565–586, 1999.

[54] Phys.org, "Big bang theory and the mysteries of dark matter," 2015. `https://phys.org/news/2015-12-big-theory.html`.

[55] A. G. Riess, A. V. Filippenko, P. Challis, and et al. (The Supernova Search Team), "Cosmological Constant Problem and the End of the Universe," *The Astronomical Journal*, vol. 116, no. 3, pp. 1009–1038, 1998.

[56] E. Hertzsprung, "On the relation between the mass of a stellar system and the mass of its individual stars," *Astrophysical Journal*, vol. 37, p. 209, 1913.

[57] F. Zwicky, "How Far Do Cosmic Rays Travel?," *Physical Review*, vol. 43, pp. 147–148, Jan. 1933.

[58] J. Kepler, *Astronomia Nova*. Typis Iacobi Bertschii, 1609.

[59] L. Rossi, "How dark matter became a particle," *CERN Courier*, February 2019.

[60] D. H. Rogstad and G. S. Shostak, "Gross Properties of Five Scd Galaxies as Determined from 21-CENTIMETER Observations," , vol. 176, p. 315, Sept. 1972.

[61] D. Clowe, M. Bradac, A. H. Gonzalez, M. Markevitch, S. W. Randall, C. Jones, et al., "Weak lensing mass reconstruction of the interacting cluster 1e0657-558: Direct evidence for the existence of dark matter," *The Astrophysical Journal*, vol. 648, no. 2, pp. L93–L96, 2006.

[62] D. Clowe, M. Bradač, A. H. Gonzalez, M. Markevitch, S. W. Randall, C. Jones, et al., "A direct empirical proof of the existence of dark matter," *The Astrophysical Journal*, vol. 648, no. 2, pp. L109–L113, 2006.

[63] P. A. R. Ade et al., "Planck 2015 results. XIII. Cosmological parameters," *Astron. Astrophys.*, vol. 594, p. A13, 2016.

[64] ESA, "Planck cmb." [Online Image], March 2013. `https://www.esa.int/ESA_Multimedia/Images/2013/03/Planck_CMB`, Accessed: 1 May, 2023.

[65] G. 't Hooft, "Symmetry breaking through bell-jackiw anomalies," *Phys. Rev. Lett.*, vol. 37, pp. 8–11, Jul 1976.

[66] P. A. Zyla et al., "Heavy neutral leptons (pdf)," *Progress of Theoretical and Experimental Physics*, vol. 2020, no. 8, p. 083C01, 2020.

[67] G. Bertone, D. Hooper, and J. Silk, "Weakly interacting massive particle dark matter candidates and searches," *Physics Reports*, vol. 405, no. 5-6, pp. 279–390, 2005.

[68] T. M. C. Abbott et al., "Dark Energy Survey Year 3 results: Cosmological constraints from galaxy clustering and weak lensing," *Phys. Rev. D*, vol. 105, no. 2, p. 023520, 2022.

[69] A. Abramowski et al., "The H.E.S.S. Survey of the Inner Galaxy in Very High-Energy γ Rays," *The Astrophysical Journal*, vol. 735, no. 2, p. 63, 2011.

[70] A. A. Abdo et al., "The Fermi Large Area Telescope on Orbit: Event Classification, Instrument Response Functions, and Calibration," *The Astrophysical Journal Supplement Series*, vol. 183, no. 1, p. 46, 2009.

[71] R. Abbasi et al., "The IceCube Neutrino Observatory: Instrumentation and Online Systems," *Journal of Instrumentation*, vol. 12, no. 03, p. P03012, 2017.

[72] O. Adriani et al., "The PAMELA Mission: A Payload for Antimatter Matter Exploration and Light-nuclei Astrophysics," *Astroparticle Physics*, vol. 34, no. 1, pp. 1–54, 2010.

[73] M. Aguilar et al., "The Alpha Magnetic Spectrometer (AMS) on the International Space Station: Part I—Results from the Test Flight on the Space Shuttle," *Physics Reports*, vol. 366, no. 6, pp. 331–405, 2002.

[74] C. Pérez de los Heros, "Status, Challenges and Directions in Indirect Dark Matter Searches," *Symmetry*, vol. 12, no. 10, p. 1648, 2020.

[75] C. Armand, E. Charles, M. di Mauro, C. Giuri, J. P. Harding, D. Kerszberg, T. Miener, *et al.*, "Combined dark matter searches towards dwarf spheroidal galaxies with Fermi-LAT, HAWC, H.E.S.S., MAGIC, and VERITAS," 2021.

[76] Q. R. Ahmad *et al.*, "The Sudbury Neutrino Observatory," *Nuclear Instruments and Methods in Physics Research Section A: Accelerators, Spectrometers, Detectors and Associated Equipment*, vol. 449, no. 1-2, pp. 172–207, 2000.

[77] M. Schumann, "Direct detection of WIMP dark matter: concepts and status," *Journal of Physics G: Nuclear and Particle Physics*, vol. 46, p. 103003, Aug 2019.

[78] J. Aalbers, D. S. Akerib, C. W. Akerlof, *et al.*, "First dark matter search results from the lux-zeplin (lz) experiment," 2022.

[79] H. P. Nilles, "Supersymmetry, Supergravity and Particle Physics," *Phys. Rept.*, vol. 110, pp. 1–162, 1984.

[80] L. Randall and R. Sundrum, "Out of this world supersymmetry breaking," *Nucl. Phys.*, vol. B557, pp. 79–118, 1999.

[81] B. Aharmim, S. N. Ahmed, T. C. Andersen, A. E. Anthony, and e. Barros, "Limits on nucleon decay via invisible modes from the sudbury neutrino observatory," *Phys. Rev. D*, vol. 71, p. 072005, Apr 2005.

[82] R. Barbier *et al.*, "R-parity violating supersymmetry," *Phys. Rept.*, vol. 420, pp. 1–202, 2005.

[83] E. Fermi, "On the quantum theory of collisions," *Nuovo Cimento*, vol. 2, no. 1, pp. 22–29, 1928.

[84] N. Nagata and S. Shirai, "Higgsino dark matter in high-scale supersymmetry," *Journal of High Energy Physics*, vol. 2015, Jan 2015.

[85] M. Mrowietz, *Constraints on Supersymmetry from Collider Searches and Other Experiments*. PhD thesis, University of Hamburg, 2023. PhD thesis, To be published.

[86] J. H. Christenson, J. W. Cronin, V. L. Fitch, and R. Turlay, "Evidence for the 2π Decay of the $K2^0$ Meson," *Physical Review Letters*, vol. 13, no. 4, pp. 138–140, 1964.

[87] S. L. Glashow, J. Iliopoulos, and L. Maiani, "Violations of C invariance and baryon number in the SU(2) × U(1) theory of weak interactions," *Physical Review D*, vol. 2, no. 7, p. 1285, 1970.

149

[88] J. Alimena, J. Beacham, M. Borsato, *et al.*, "Searching for long-lived particles beyond the standard model at the large hadron collider," *Journal of Physics G: Nuclear and Particle Physics*, vol. 47, p. 090501, Sep 2020.

[89] G. L. Bayatian *et al.*, *CMS Physics: Technical Design Report Volume 1: Detector Performance and Software.* Technical Design Report CMS, Geneva: CERN, 2006.

[90] AC Team, "The four main LHC experiments," 1999. https://cds.cern.ch/record/40525.

[91] CMS Collaboration, "CMS Luminosity - Public Results," 2016. `https://twiki.cern.ch/twiki/bin/view/CMSPublic/LumiPublicResults#2016_proton_proton_collisions_at`, Accessed: 08. December, 2023.

[92] A. M. Sirunyan *et al.*, "Precision luminosity measurement in proton-proton collisions at $\sqrt{s} = 13$ TeV in 2015 and 2016 at CMS," *Eur. Phys. J. C*, vol. 81, no. 9, p. 800, 2021.

[93] S. Czellar, A. Heikkinen, J. Härkönen, V. Karimäki, R. Kinnunen, T. Lampen, K. Lassila-Perini, CMS Collaboration, *et al.*, "CMS physics technical design report," *Journal of Physics G: Nuclear and Particle Physics , vol G34 , pp. 2307-2455 .*, 06 2023.

[94] S. Chatrchyan *et al.*, "The CMS Experiment at the CERN LHC," *JINST*, vol. 3, p. S08004, 2008.

[95] M. Schott and M. Dunford, "Review of single vector boson production in pp collisions at $\sqrt{s} = 7$ TeV," *Eur. Phys. J.*, vol. C74, p. 2916, 2014.

[96] V. Veszpremi, "Performance verification of the CMS Phase-1 Upgrade Pixel detector," *Journal of Instrumentation*, vol. 12, no. 12, p. C12010, 2017.

[97] The Tracker Group of the CMS Collaboration, "The CMS Phase-1 Pixel Detector Upgrade," tech. rep., CERN, Geneva, 2020.

[98] CMS Collaboration, "Description and performance of track and primary-vertex reconstruction with the CMS tracker," *Journal of Instrumentation*, vol. 9, no. 10, p. P10009, 2014.

[99] H. Seo, "RPC hit contribution to CMS muon reconstruction at LHC," *Nuclear Instruments and Methods in Physics Research*, vol. 718, p. 437–439, 08 2013.

[100] W. Adam *et al.*, "The CMS high level trigger," *Eur. Phys. J.*, vol. C46, pp. 605–667, 2006.

[101] CMS Collaboration, "Description and performance of track and primary-vertex reconstruction with the CMS tracker," *Journal of Instrumentation*, vol. 9, no. 10, p. P10009, 2014.

[102] P. Billoir, "Progressive track recognition with a Kalman like fitting procedure," *Comput. Phys. Commun.*, vol. 57, pp. 390–394, 1989.

[103] R. Frühwirth, "Application of kalman filtering to track and vertex fitting," *Nuclear Instruments and Methods in Physics Research Section A: Accelerators, Spectrometers, Detectors and Associated Equipment*, vol. 262, no. 2-3, pp. 444–450, 1987.

[104] CMS Collaboration, "CMS Tracker Performance results for full Run 2 Legacy reprocessing," 2020. `https://cds.cern.ch/record/2713208`.

[105] M. Kortelainen, "CMS Tracking POG Performance Plots For 2017 with PhaseI pixel detector," 2017. `https://twiki.cern.ch/twiki/bin/view/CMSPublic/TrackingPOGPerformance2017MC`, Accessed: 10 February, 2023.

[106] CMS Collaboration, "Tracking Performance Plots: CMS Public TWiki," 2016. `https://twiki.cern.ch/twiki/bin/view/CMSPublic/TrackingPOGPlotsICHEP2016`, Accessed: 28 June, 2023.

[107] A. M. Sirunyan *et al.*, "Muon reconstruction efficiency and momentum resolution of the CMS experiment in proton-proton collisions at $\sqrt{s} = 13$ TeV," *JINST*, vol. 13, no. 10, p. P10002, 2018.

[108] A. Sirunyan, A. Tumasyan, W. Adam, E. Asilar, *et al.*, "Particle-flow reconstruction and global event description with the CMS detector," *Journal of Instrumentation*, vol. 12, pp. P10003–P10003, Oct 2017.

[109] CMS Collaboration, "Particle-Flow Event Reconstruction in CMS and Performance for Jets, Taus, and MET," Tech. Rep. CMS-PAS-PFT-09-001, CERN, Geneva, Apr 2009.

[110] CMS Collaboration, "CMS physics results - muon physics," 2018. `https://twiki.cern.ch/twiki/bin/view/CMSPublic/PhysicsResultsMUO` Accessed: 7 September, 2023.

[111] A. M. Sirunyan *et al.*, "Electron and photon reconstruction with the CMS experiment at $\sqrt{s} = 13$ TeV," *JINST*, vol. 13, no. 10, p. P10003, 2018.

[112] A. Malara, "Reconstruction of jets and missing transverse momentum at the CMS experiment: Run 2 and perspective for Run 3," 2021.

[113] V. Khachatryan *et al.*, "Performance of the CMS missing transverse momentum reconstruction in pp data at $\sqrt{s} = 8$ TeV," *JINST*, vol. 10, no. 02, p. P02006, 2015.

[114] G. Aad *et al.*, "Searches for electroweak production of supersymmetric particles with compressed mass spectra in $\sqrt{s} = 13$ TeV *pp* collisions with the ATLAS detector," *Phys. Rev. D*, vol. 101, no. 5, p. 052005, 2020.

151

[115] G. Aad *et al.*, "Search for chargino–neutralino pair production in final states with three leptons and missing transverse momentum in $\sqrt{s} = 13$ TeV pp collisions with the ATLAS detector," *Eur. Phys. J. C*, vol. 81, no. 12, p. 1118, 2021.

[116] G. Aad *et al.*, "Search for long-lived charginos based on a disappearing-track signature using 136 fb^{-1} of pp collisions at $\sqrt{s} = 13$ TeV with the ATLAS detector," *Eur. Phys. J. C*, vol. 82, no. 7, p. 606, 2022.

[117] A. Hayrapetyan *et al.*, "Search for inelastic dark matter in events with two displaced muons and missing transverse momentum in proton-proton collisions at $\sqrt{s}$ = 13 TeV," *CMS-EXO-20-010, CERN-EP-2023-083 arXiv.2305.11649*, May 2023.

[118] V. Kutzner, *Search for exotic long-lived particles using disappearing tracks with the CMS experiment in proton-proton collisions at $\sqrt{s} = 13$ TeV.* PhD thesis, Universität Hamburg, 2023. PhD thesis.

[119] A. M. Sirunyan *et al.*, "Search for new physics in final states with an energetic jet or a hadronically decaying W or Z boson and transverse momentum imbalance at $\sqrt{s} = 13$ TeV," *Phys. Rev. D*, vol. 97, no. 9, p. 092005, 2018.

[120] A. Tumasyan *et al.*, "Search for new particles in events with energetic jets and large missing transverse momentum in proton-proton collisions at $\sqrt{s} = 13$ TeV," *JHEP*, vol. 11, p. 153, 2021.

[121] A. Tumasyan *et al.*, "Search for supersymmetry in final states with two or three soft leptons and missing transverse momentum in proton-proton collisions at $\sqrt{s}$ = 13 TeV," *JHEP*, vol. 04, p. 091, 2022.

[122] B. Fuks, M. Klasen, D. R. Lamprea, and M. Rothering, "Precision predictions for electroweak superpartner production at hadron colliders with RESUMMINO," *Eur. Phys. J. C*, vol. 73, p. 2480, 2013.

[123] B. Fuks, M. Klasen, D. R. Lamprea, and M. Rothering, "Gaugino production in proton-proton collisions at a center-of-mass energy of 8 TeV," *JHEP*, vol. 10, p. 081, 2012.

[124] V. Beylin, V. Kuksa, R. Pasechnik, and G. Vereshkov, "Neutralino-nucleon interaction in the Split SUSY scenario of the Dark Matter," *International Journal of Modern Physics A*, vol. 24, 03 2009.

[125] M. Tanabashi and et al. (Particle Data Group), "Review of particle physics," *Physical Review D*, vol. 98, p. 030001, 2018.

[126] G. Abbiendi *et al.*, "Search for nearly mass degenerate charginos and neutralinos at LEP," *Eur. Phys. J. C*, vol. 29, pp. 479–489, 2003.

[127] M. Rammensee and others (on behalf of the ATLAS and CMS Collaborations), "SUSY searches: Recent results from ATLAS and CMS," *Journal of Physics: Conference Series*, vol. 631, p. 012072, Jul 2015.

[128] M. Ibe, S. Matsumoto, and R. Sato, "Mass Splitting between Charged and Neutral Winos at Two-Loop Level," *Phys. Lett. B*, vol. 721, pp. 252–260, 2013.

[129] ATLAS Collabortaion, "SUSY Summary Plots June 2021," *ATL-PHYS-PUB-2021-019*, 2021.

[130] T. Sjöstrand, S. Ask, J. R. Christiansen, R. Corke, N. Desai, P. Ilten, S. Mrenna, *et al.*, "An introduction to PYTHIA 8.2," *Comput. Phys. Commun.*, vol. 191, pp. 159–177, 2015.

[131] S. Agostinelli *et al.*, "GEANT4–a simulation toolkit," *Nucl. Instrum. Meth. A*, vol. 506, pp. 250–303, 2003.

[132] S. Abdullin, P. Azzi, F. Beaudette, P. Janot, A. Perrotta, and (on behalf of the CMS Collaboration), "The Fast Simulation of the CMS Detector at LHC," *Journal of Physics: Conference Series*, vol. 331, p. 032049, Dec 2011.

[133] B. C. Allanach, "SOFTSUSY: a program for calculating supersymmetric spectra," *Comput. Phys. Commun.*, vol. 143, pp. 305–331, 2002.

[134] J. Alwall, M. Herquet, F. Maltoni, O. Mattelaer, and T. Stelzer, "MadGraph 5 : Going Beyond," *JHEP*, vol. 06, p. 128, 2011.

[135] M. J. French, L. L. Jones, Q. R. Morrissey, A. Neviani, R. Turchetta, J. R. Fulcher, G. Hall, *et al.*, "Design and results from the APV25, a deep sub-micron CMOS front-end chip for the CMS tracker," *Nucl. Instrum. Methods Phys. Res., A*, vol. 466, no. 2, pp. 359–65, 2001.

[136] F. Cavallari and C. Rovelli, "Calibration and performance of the cms electromagnetic calorimeter in lhc run2," *EPJ Web of Conferences*, vol. v, 2020.

[137] BRIL Group, "Bril work suite," 2017. `http://cms-service-lumi.web.cern.ch/cms-service-lumi/brilwsdoc.html`.

[138] CMS Collaboration, "StripsOfflinePlots2016 - cms public twiki," 2016. `https://twiki.cern.ch/twiki/bin/view/CMSPublic/StripsOfflinePlots2016`.

[139] L. A. T. Bauerdick, G. Eulisse, C. D. Jones, D. Kovalskyi, T. McCauley, A. M. Tadel, J. Muelmenstaedt, I. Osborne, M. Tadel, Y. Tu, and A. Yagil, "Event Display for the Visualization of CMS Events," *Journal of Physics: Conference Series*, vol. 331, p. 072039, dec 2011.

[140] C. Collaboration, "Egamma PFBased Isolation for Run2." `https://twiki.cern.ch/twiki/bin/view/CMS/EgammaPFBasedIsolationRun2`, Accessed: 1 November, 2023.

[141] A. Hocker *et al.*, "TMVA - Toolkit for Multivariate Data Analysis," *CERN-OPEN-2007-007, physics/0703039*, Mar 2007.

[142] M. Wolf, *Search for Higgsinos in final states with a low-momentum, displaced track.* Masterthesis, Universität Hamburg, Institut für Experimentalphysik, Mar 2020.

[143] G. Agarwal, "Jet Energy Scale and Resolution Measurements in CMS," *PoS*, vol. ICHEP2022, p. 652, 2022.

[144] A. M. Sirunyan *et al.*, "Pileup mitigation at CMS in 13 TeV data," *JINST*, vol. 15, no. 09, p. P09018, 2020.

[145] CMS Collaboration, "LHCPhysics TWiki: SUSY cross sections." `https://twiki.cern.ch/twiki/bin/view/LHCPhysics/SUSYCrossSections`, Accessed: December 1, 2023.

[146] CMS Collaboration, "HiggsAnalysis-CombinedLimit github repository." `https://cms-analysis.github.io/HiggsAnalysis-CombinedLimit/`. Accessed: December 1, 2023.

[147] T. Junk, "Confidence level computation for combining searches with small statistics," *Nucl. Instrum. Meth. A*, vol. 434, pp. 435–443, 1999.

[148] A. L. Read, "Presentation of search results: the cls technique," *Journal of Physics G: Nuclear and Particle Physics*, vol. 28, p. 2693, Sept. 2002.

[149] Y. Nissan, *Search for compressed mass Higgsino production with low-momentum lepton tracks with the CMS experiment.* PhD thesis, Universität Hamburg, 2023. PhD thesis.

[150] M. Wolf, *Search for Higgsinos in Final States with a Low-momentum, Displaced Track at the CMS Experiment.* PhD thesis, University of Hamburg, 2024. PhD thesis, To be published.

[151] S. Sekmen, "Recent Developments in CMS Fast Simulation," *PoS*, vol. ICHEP2016, p. 181, 2016.

List of Figures

List of Tables

Eidesstattliche Versicherung / Declaration on oath

Hiermit versichere ich an Eides statt, die vorliegende Dissertationsschrift selbst verfasst und keine anderen als die angegebenen Hilfsmittel und Quellen benutzt zu haben.

Hamburg, den ___08.01.2024___

Alexandra Tews

Unterschrift der Doktorandin / des Doktoranden